Representation of Tones and Vowels in a Biophysically Detailed Model of Ventral Cochlear Nucleus

REPRESENTATION OF TONES AND VOWELS IN A BIOPHYSICALLY DETAILED MODEL OF VENTRAL COCHLEAR NUCLEUS

BY

MELIH YAYLI, B.Sc.

A THESIS

SUBMITTED TO THE DEPARTMENT OF ELECTRICAL & COMPUTER ENGINEERING

AND THE SCHOOL OF GRADUATE STUDIES

OF MCMASTER UNIVERSITY

IN PARTIAL FULFILMENT OF THE REQUIREMENTS

FOR THE DEGREE OF

MASTER OF APPLIED SCIENCE

Master of Applied Science (2018) McMaster University

(Electrical & Computer Engineering) Hamilton, Ontario, Canada

TITLE:	Representation of Tones and Vowels in a Biophysically Detailed Model of Ventral Cochlear Nucleus
AUTHOR:	Melih YAYLI B.Sc., (Electrical and Electronics Engineering) Ankara University, Ankara, Turkey
SUPERVISOR:	Dr. Ian C. Bruce
NUMBER OF PAGES:	xvi, 146

To the people who are dealing with depression and anxiety through their lives. We can do it, do not lose hope...

Abstract

Biophysically detailed representations of neural network models provide substantial insight to underlying neural processing mechanisms in the auditory systems of the brain. For simple biological systems the behavior can be represented by simple equations or flow charts. But for complex systems, more detailed descriptions of individual neurons and their synaptic connectivity are typically required. Creating extensive network models allows us to test hypotheses, apply specific manipulations that cannot be done experimentally and provide supporting evidence for experimental results. Several studies have been made on establishing realistic models of the cochlear nucleus (Manis and Campagnola, 2018; Eager *et al.*, 2004), the part of the brainstem where sound signals enter the brain, both on individual neuron and networked structure levels. These models are based on both in vitro and in vivo physiological data, and they successfully demonstrate certain aspects of the neural processing of sound signals. Even though these models have been tested with tone bursts and isolated phonemes, the representation of speech in the cochlear nucleus and how it may support robust speech intelligibility remains to be explored with these detailed biophysical models.

In this study, the basis of creating a biophysically detailed model of microcircuits in the cochlear nucleus is formed following the approach of Manis and Campagnola (2018). The focus of this thesis is more on bushy cell microcircuits. We have updated

Manis and Campagnola (2018) model to take inputs from the new phenomenological auditory periphery model of Bruce *et al.* (2018). Different cell types in the cochlear nucleus are modelled by detailed cell models of Rothman and Manis (2003c) and updated Manis and Campagnola (2018) cell models. Networked structures are built out of them according to published anatomical and physiological data. The outputs of these networked structures are used to create post-stimulus-time-histograms (PSTH) and response maps to investigate the representation of tone bursts and average localized synchronized rate (ALSR) of phoneme /ε/ and are compared to published physiological data (Blackburn and Sachs, 1990).

Acknowledgements

First of all, I would like to thank my supervisor Dr Ian C. Bruce for guiding me through this process by constantly providing academic and emotional support. His calm nature was always assuring me, a panicking graduate student who thinks what he does is not enough. Finishing this thesis would not be possible without his help.

I also want to thank my family for always being there for me even though they were thousands of kilometers away. Especially to my father, for supporting me as a parent, a teacher and a friend. And my close friends who I was constantly in contact with through various group chats. They showed me distance is a relative measure and you don't have to be in the same place to feel love and support.

Notation and abbreviations

AN Auditory Nerve

ANF Auditory Nerve Fiber

AVCN Anteroventral Cochlear Nucleus

BF Best Frequency

BNN Bio-physically-accurate Neural Network

CF Characteristic Frequency

ChS Sustained Chopper

ChT Transient Choppper

CN Cochlear Nucleus

CV Coefficient of Variation

DCN Dorsal Cochlear Nucleus

DS D Stellate

EPSC Excitatory Post-Synaptic Current

EPSP Excitatory Post-Synaptic Potential

GABA Gamma-Aminobutyric Acid

GABAa GABAergic subtype A

GlyR Glycine Receptor

HH Hodgkin-Huxley

HSR High Spontaneous Rate

IC Inferior Colliculus

IHC Inner Hair Cell

IPSC Inhibitory Post-Synaptic Current

IPSP Inhibitory Post-Synaptic Potential

KLT Low-threshold Potassium Channel

KHT High-threshold Potassium Channel

LSR Low Spontaneous Rate

MNTB Medial Nucleus of Trapezoidal Body

MOC Medial Olivocochlear

NMDA N-Methyl-D-aspartic Acid

OHC Outer Hair Cell

OnC Onset Chopper

OnL Onset with Latent Response

PL Primary-like

PLn Primary-like with Notch

PSP Post-synaptic Potential

PSTH Peri-stimulus Time Histogram

PVCN Posteroventral Cochlear Nucleus

RM Rothmann and Manis

SNR Signal to Noise Ratio

SPL Sound Pressure Level

SR Spontaneous Rate

TS T Stellate

TV Tuberculoventral

VCN Ventral Cochlear Nucleus

Contents

List of Figures

Chapter 1

Introduction and Literature Review

1.1 Introduction

The mammalian auditory system is a complex structure consisting of sections that apply different type of processing to sound signals. Creating extensive models of this system based on physiological and anatomical data is important in terms of providing researchers with new tools for inspecting sound processing in the auditory system. Each stage shows nonlinear behaviour and creating detailed models of these stages has its own challenges. The focus of this thesis is on the cochlear nucleus where the sound signals first enter the brain. In the cochlear nucleus features of sound are extracted that help understanding where the sound comes from and what the sound is.

The cochlear nucleus consists of various types of neurons. Two types of primary neurons that send information to the upper stages on the central auditory system

are bushy cells and stellate cells (Campagnola and Manis, 2014). Detailed Hodgkin-Huxley type models of these cells have been created by Rothman and Manis (2003c). By interconnecting them with simple synapse models, networked structures are created to simulate the behaviour of cochlear nucleus microcircuits. The circuit models are tested and the parameters of the model are tuned to match with the physiological recordings and simulation results presented in Rothman and Manis (2003c), Eager *et al.* (2004) and Manis and Campagnola (2018).

In this part of the thesis, important background information is presented: an overview of how sound is processed by the auditory system, stages of the auditory system, a detailed description of the cochlear nucleus, Hodgkin-Huxley models, and synaptic modeling. This information is relevant to understand how realistic models of the cochlear nucleus are created.

Chapter 2 introduces the Bruce *et al.* (2018) auditory periphery model and the Rothman and Manis (2003c) model of ventral cochlear nucleus (VCN) neurons. An updated version of VCN cell models presented by Manis and Campagnola (2018) is also reviewed.

In Chapter 3 the results of various tests are presented. Individual cell models are tested by applying current injections and synaptic inputs. The synaptic model mechanism is tested to check if mechanisms like synaptic convergence (more than one neuron connecting to a single neuron) and summation are working properly. Small interconnected structures called as microcircuits are formed out of cell models to further investigate the cell behaviour to auditory nerve (AN) like inputs. The AN model is fed with tone bursts with different frequencies to conduct these tests. Resulting post-stimulus-time-histograms (PSTH), the regularity of firing and response

maps are checked to see if the model is acting according to physiological data. At the end of the chapter, the microcircuits are tested by appyling a synthetic phoneme as inputs to the AN model. The results are compared with the physiological data presented in Blackburn and Sachs (1990).

Chapter 4 finalizes this thesis by commenting on the results and future work.

The code used in this research can be found in the Appendix.

1.2 Auditory Periphery

1.2.1 Outer Ear

The processing of the sound starts before it enters the ear canal. The outer ear is a structure consisting of the pinna, concha and ear canal (external auditory meatus) that ends at the eardrum (tympanic membrane) (Fig. 1.1). The mission of the outer ear is to collect sound waves coming from different directions and channel them into the ear canal. With the help of resonance effects, the outer ear helps increase the pressure on the eardrum which causes more energy to be transferred to the middle ear (Schnupp *et al.*, 2011).

In humans, this pressure increase has a broad peak (15-20 dB) centered around 2.5 kHz since the combined length of the concha and ear canal is approximately equal to a quarter wavelength of this frequency. Even though the pinna and concha create a complex acoustic cavity, which is expected to cause pressure gain to be highly frequency dependent, the changes are fairly uniform between 2 kHz and 7 kHz (Fig. 1.2).

Another contribution of the outer ear to the sound processing is providing valuable

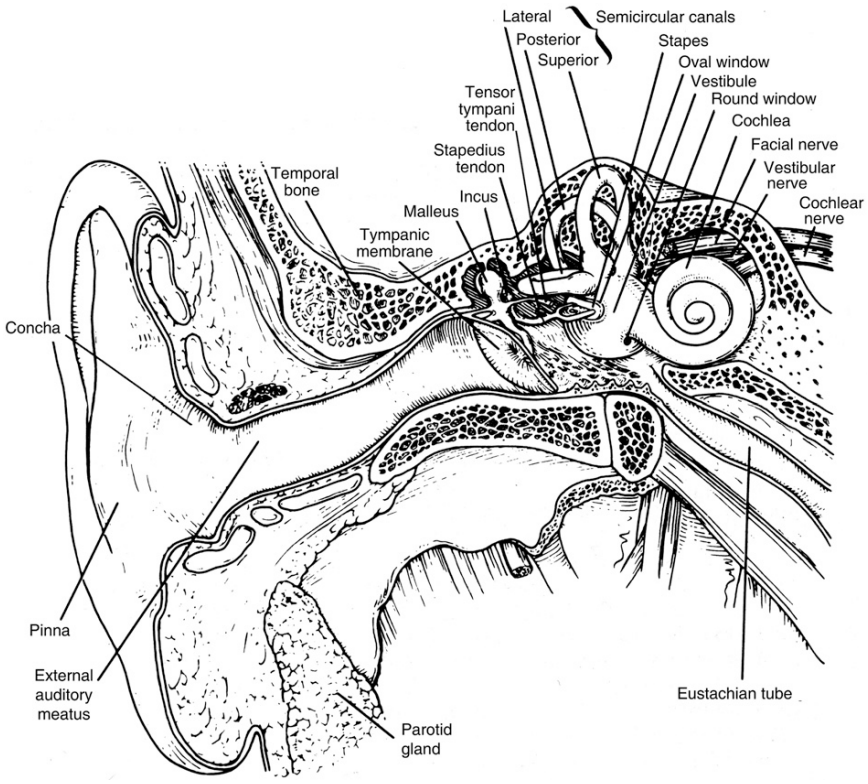

Figure 1.1: Auditory periphery of humans. Reprinted with permission of the Brill Publishers, Figure 2.1 from Pickles (2013) ©2013.

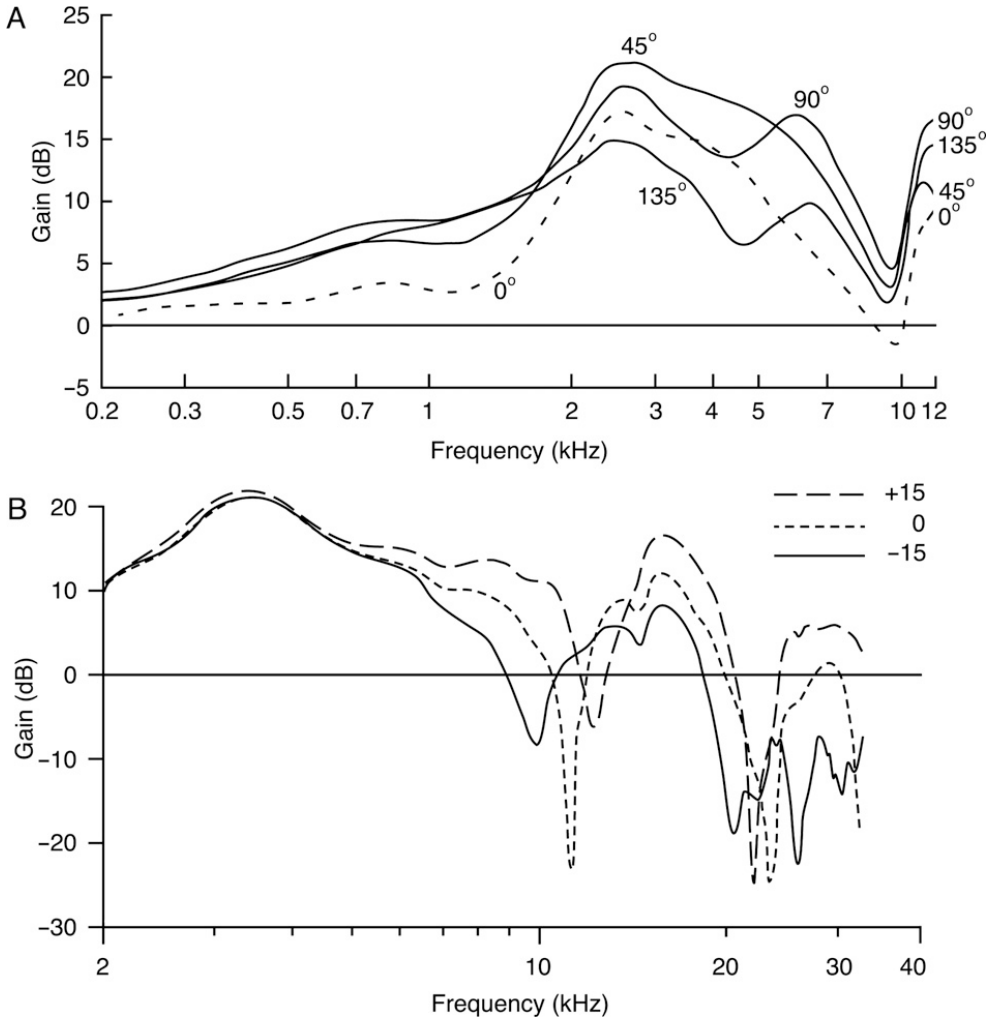

Figure 1.2: (A) Average pressure gain of human outer ear as a function of frequency for different directions. 0° indicates the sound source is straight ahead. (B) The change in the gain as a function of frequency of cat ear related to the elevation of the sound source. 0° indicates the horizontal plane. Reprinted with permission of the Brill Publishers, Figure 2.2 from Pickles (2013) ©2013.

information about the sound location. The most obvious indicator of where the sound comes from is the timing difference between left and right ear. Depending on the direction of the sound the intensity will also tend to be higher in the ear that is closer to the source. But binaural timing and level differences do not directly indicate whether the sound is coming from behind or front, or from a lower or higher source. The pinna and concha have distinctive shapes that reflect the sounds into the ear canal differently depending on the direction and elevation of the source. This causes waves to arrive in different phases which leads to cancellation. So the intensity of the stimulus is reduced at certain frequencies dependent on sound location in the vertical plane. Later stages of the auditory system use this information to distinguish the vertical location of the sound source.

1.2.2 Middle Ear

After the sound wave travels through the ear canal, it hits the tympanic membrane. As a result the tympanic membrane vibrates and these vibrations are propagated through the middle ear by ossicles, three small bones named the malleus, incus and stapes (hammer, anvil and stirrup) (Fig 1.3). The purpose of this system is to transmit the sound signal while reducing the energy loss between the air, which has a low acoustic impedance, and the cochlea which is filled with a physiological fluid that has a higher acoustic impedance than air. Without a system like this, most of the sound energy would be reflected at the eardrum. So it can be said that the middle ear is applying impedance matching.

The mechanism works as follows: when sound waves hit the tympanic membrane, incus and malleus which are bonded tightly, are pushed by membrane. The bones

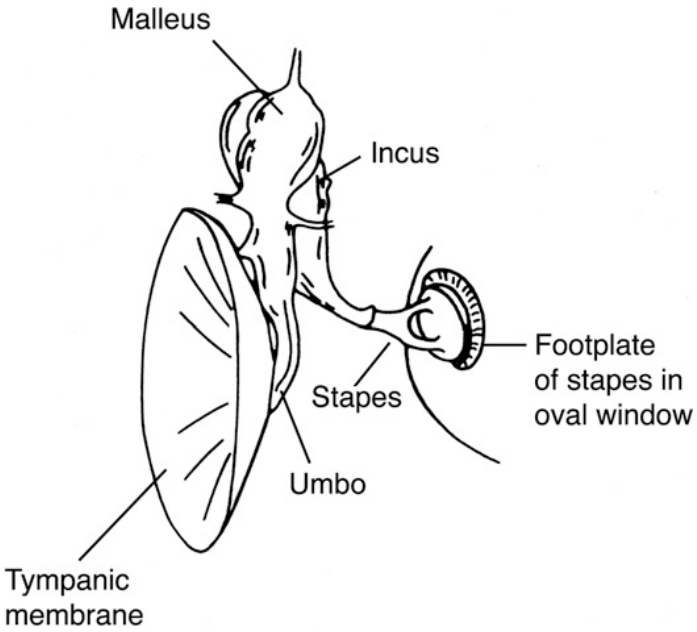

Figure 1.3: Physiology of middle ear which consists of incus, malleus and stapes. Reprinted with permission of the Brill Publishers, Figure 2.4 from Pickles (2013) ©2013.

start to rotate, appyling a force to the stapes, which causes a displacement in the oval window of the cochlea.

The main impedance gain comes from focusing the forces that hits the tympanic membrane having a large surface area to the oval window which has smaller surface area. This phenomena causes an increase in the pressure over the oval window. The gain is dependent on the surface area ratio and the bony structures vibration response to the sounds.

The middle ear also works as a protection mechanism. By contracting the stapedius muscle the motion of the stapes can be reduced, which helps protect the inner ear structures from damage caused by loud sounds.

1.2.3 Cochlea

The cochlea is a coiled structure located deep in the temporal bone. The anatomical structure of the cochlea is shown in the Fig. 1.4. The cochlea is divided into three sections called scalae: the scala vestibuli, the scala tympani, and the scala media which separates the other two. But this separation is not complete, as the scala tympani and scala vestibuli connect with each other at the apex of the cochlea by an opening called the helicotrema. The scala vestibuli is separated from the scala media by Reissner′s membrane, while the scala tympani is separated from the scala media by the basilar membrane. The scala vestibuli and the scala tympani are filled with an ionic fluid called perilymph, while the scala media has endolymph. Perilymph has a high concentration of sodium ions (Na+) and a low concentration of potassium (K+). Endolymph has a high K+ and low Na+ concentrations and rests at a high positive potential (of about +80mV).

There are two types of mechanical resistance in the cochlea: the basilar membrane stiffness and the cochlear fluid inertia. The basilar membrane is a structure that has more resistance on the end near the oval window (base) and is more elastic near the helicotrema. On the other hand, the inertial gradient is increasing while moving towards apex and this inertial resistance is dependent on the frequency. Higher frequencies tend to cause maximal displacement of the basilar membrane towards the base, while lower frequencies cause maximal displacement towards the apex. As a result, these two factors contribute to the frequency mapping in the basilar membrane, meaning that if a single sinusoidal input with a certain frequency is presented, it will cause movement that has a sharp peak in a highly localized region of the basilar membrane. This frequency specific response also occurs at higher levels of the auditory

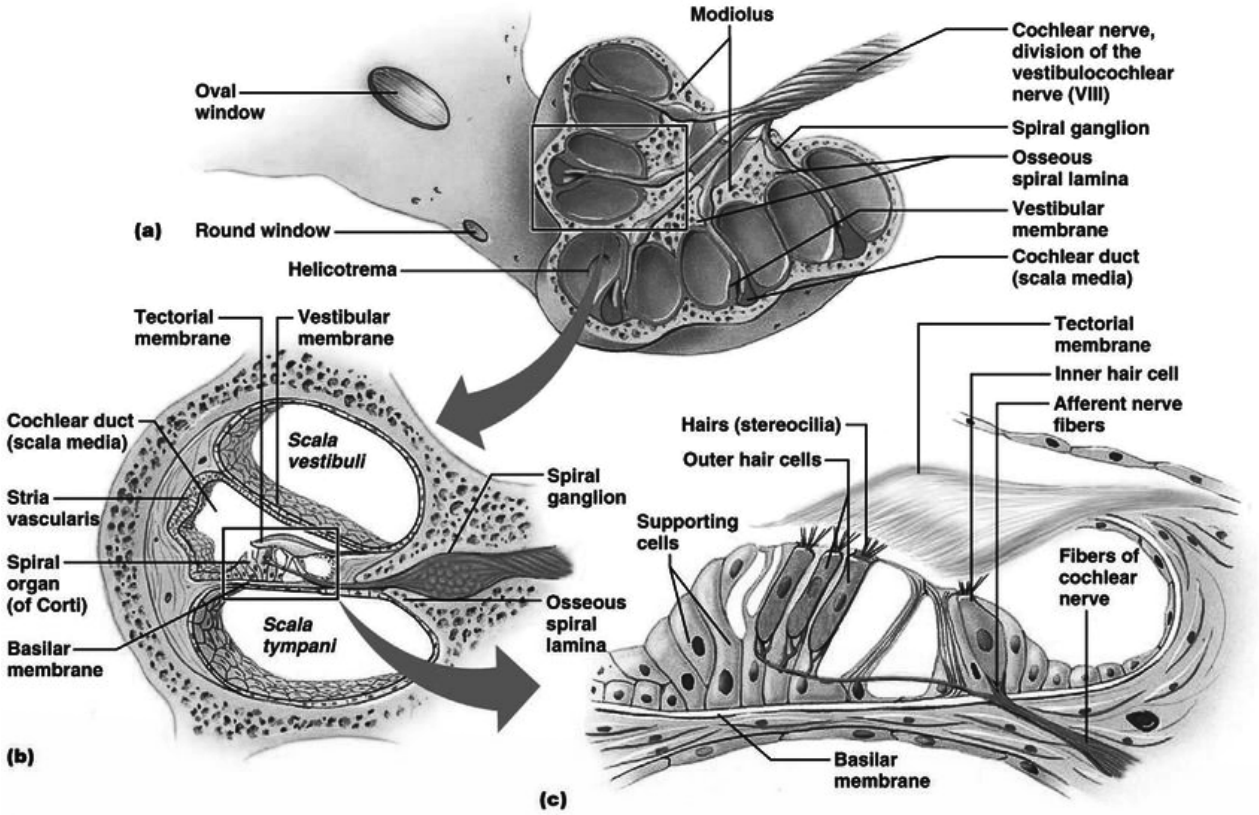

Figure 1.4: An illustration of anatomy of cochlea. (a) A cross section of coilings. (b) 3 major compartments of cochlea; scala vestibuli, scala media, scala tympani. (c) The structure of organ of corti. From Anatomybody-charts (2016).

system (Fig 1.5).

The mechanical movement of basilar membrane turns into electrical signal in a structure called the organ of Corti that is attached to the basilar membrane. When the basilar membrane moves up and down, the corresponding part of the organ of Corti also moves along with it. The organ of corti achieves the transduction via hair cells (Fig. 1.6).

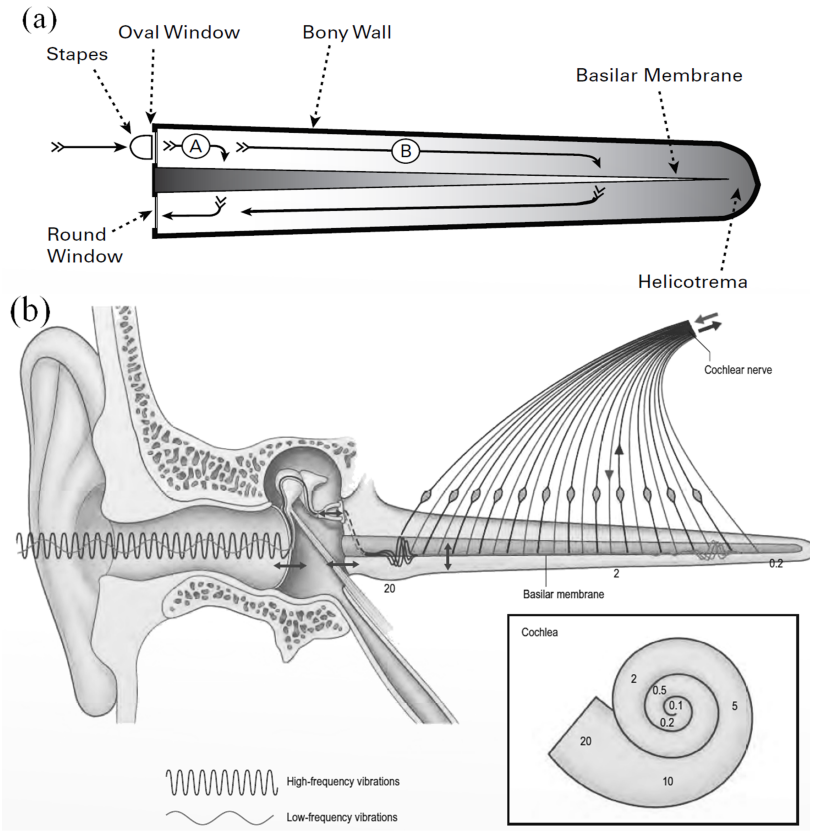

Figure 1.5: (a) The different gradients of resistance in cochlea. Reprinted with permission of the MIT Press, Figure 2.2 from Schnupp *et al.* (2011) ©2011. (b) The frequency selectivity of the basilar membrane. Higher frequency inputs cause a displacement closer to the base while the lower frequency ones cause a vibration on the apex side of cochlear duct. Inner Figure, a rough sketch of the distribution of frequency tuning across cochlea. Numbers indicate frequencies in kHz. From Standring (2015).

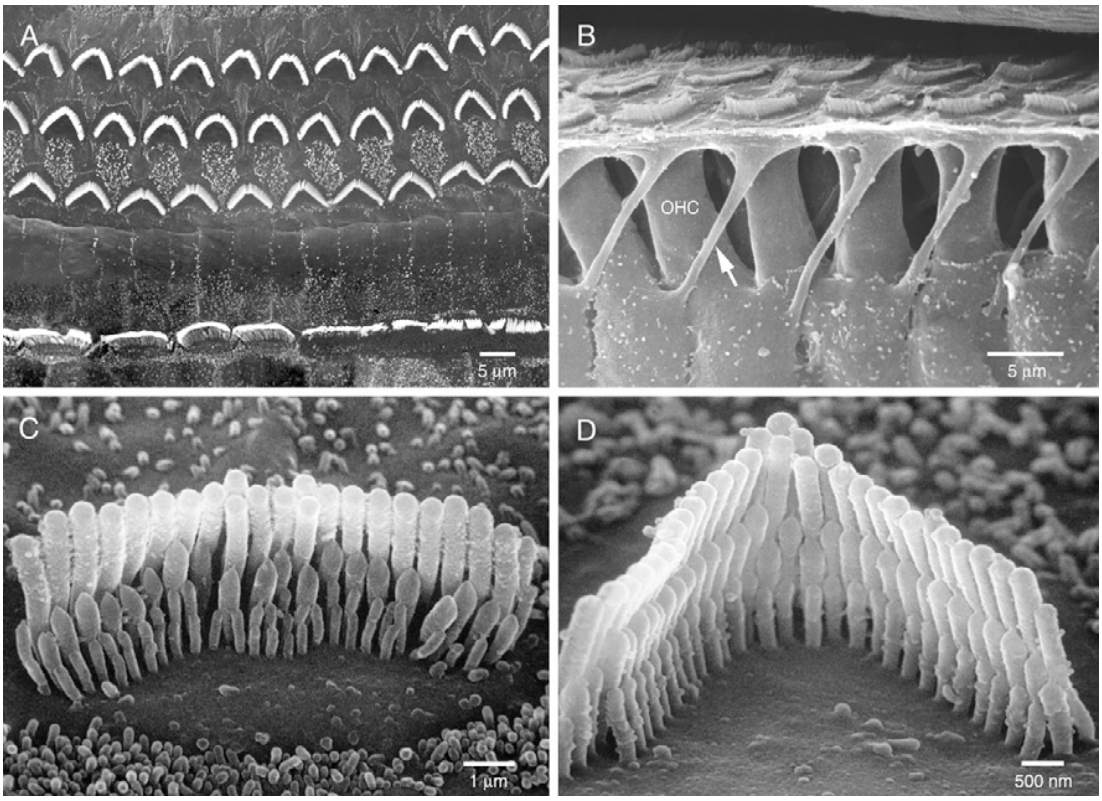

Figure 1.6: (a) Three rows of outer hair cells and a row of inner hair cells, captured by scanning electron micrograph after removing the tectorial membrane. (b) The cylindirical body of OHCs. (c) A closer look at inner hair cell bundles. (d) A closer look at outer hair cell bundles. Reprinted with permission of the Brill Publishers, Figure 3.4 from Pickles (2013) ©2013.

The tectorial membrane, which sits on top of the inner hair cells (IHCs), pushes cells by moving the highest stereocilia in the bundle as the basilar membrane moves. Inner hair cells sits in a row and are closer to the center part of the cochlea. The movement of the inner hair cells are dependent on the fluid movement since they do not have any direct contact with tectorial membrane. Even though the movement mechanisms are different, they succesfully capture the movement of the basilar membrane.

As the tectorial membrane moves, outer hair cells (OHCs), which contains dozens

of stereocilia, are deflected. These stereocilias are not in the same length and connected to each other by fine protein fibers (Fig. 1.7). When the longest stereocilia moves, it causes all of the stereocilia on the same bundle to move and this causes the K+ ions, which are supplied by the stria vascularis, to flow inside hair cells. This flow causes a depolarization in the hair cell. And this flow is dependent on the displacement of the basilar membrane since the greater displacement causes more channels to open which means more depolarizing current to flow inside. By this mechanism, the movement pattern of the membrane is translated into a current.

Outer hair cells have unique structural properties. Their membrane has a protein called prestin which makes them shorter when depolarized and longer when they are hyperpolarized. This protein gives outer hair cells the ability to change their length at high speed. Even though the exact mechanism is not clear, it is known that OHCs provide mechanical gain in a feedforward manner. It is suggested that the more the basilar membrane moves, the more OHCs are deflected, and in return OHC movement causes basilar membrane to move even more. But this improvement is not the same along the basilar membrane, and the low amplitude sounds are boosted more than high amplitude sounds (Fig. 1.8). Since OHCs have crucial roles in the transduction process, damaging these cells would cause extreme disruption in hearing process. In fact the most common cause of hearing problems is damage to OHCs (Schnupp *et al.*, 2011).

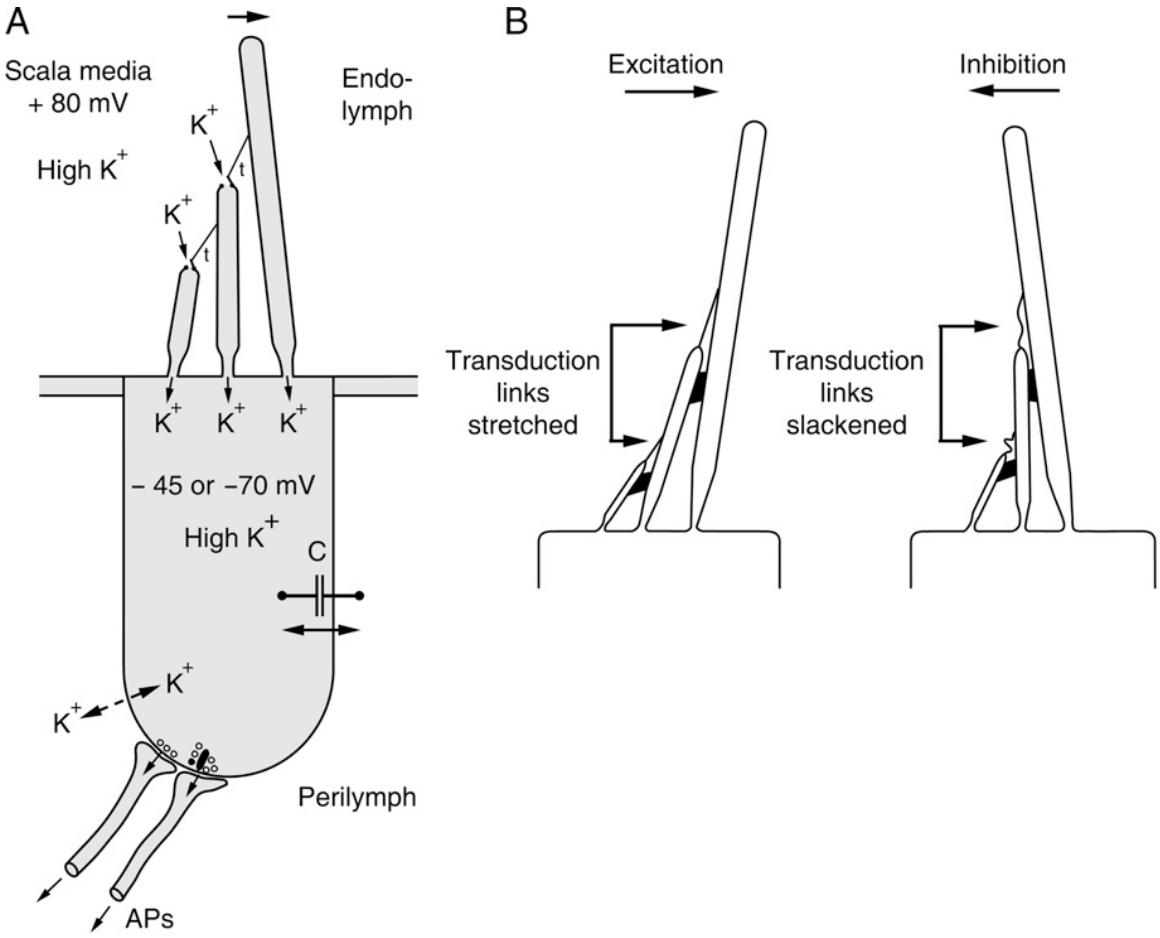

Figure 1.7: (a) The mechanism of the hair cell transduction. When the tectorial membrane moves, it causes a movement on the highest one of the stereocilia bundle. This movement results in the opening of the channels reside on the tips of stereocilia. The K^+ ions flow into the cell and produce a current according to the movement of the membrane. (b) The movement of the membrane can have excitatory or inhibitory effects on the hair cell bundle. Reprinted with permission of the Brill Publishers, Figure 3.19 from Pickles (2013) ©2013.

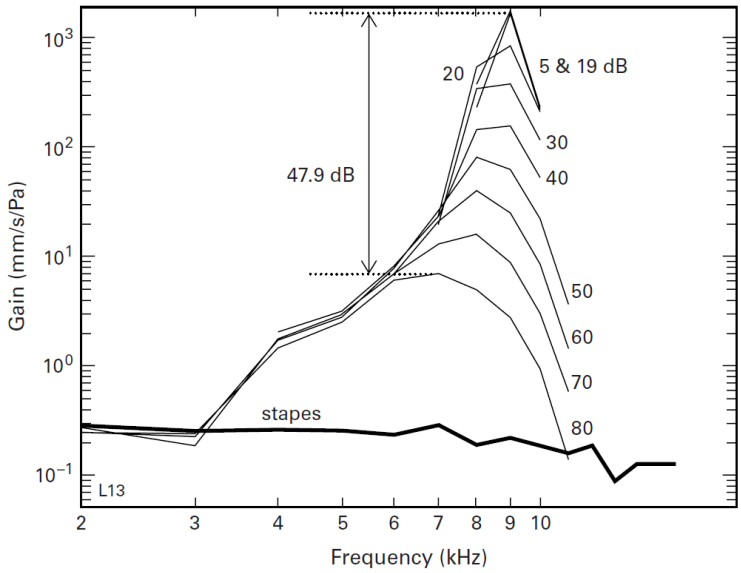

Figure 1.8: The characteristic of gain of 9kHz CF point on the basilar membrane in response to different frequency stimulus. Reprinted with permission of the MIT Press, Figure 2.10 from Schnupp *et al.* (2011) ©2011.

1.2.4 Auditory Nerve

The outer and inner hair cells are connected to auditory nerve fibers (Fig. 1.9). According to Pickles (2013), the human cochlea is innervated by 30000 sensory neurons. The auditory information is carried to the upper levels of auditory system via these afferent fibers. These fibers have their cell bodies in the spiral ganglion, while one side takes the auditory information from hair cells and the other side projects to the cells of the cochlear nucleus which resides in the brainstem. 95% of the afferent fibers are exclusively connected to the inner hair cells. Each fiber connects to one IHC. These fibers are specified as Type I fibers and they have myelinated cell bodies and axons. OHCs are connected by unmyelinated Type II fibers. Fibers that connect to OHCs branch and innervate about 10 hair cells.

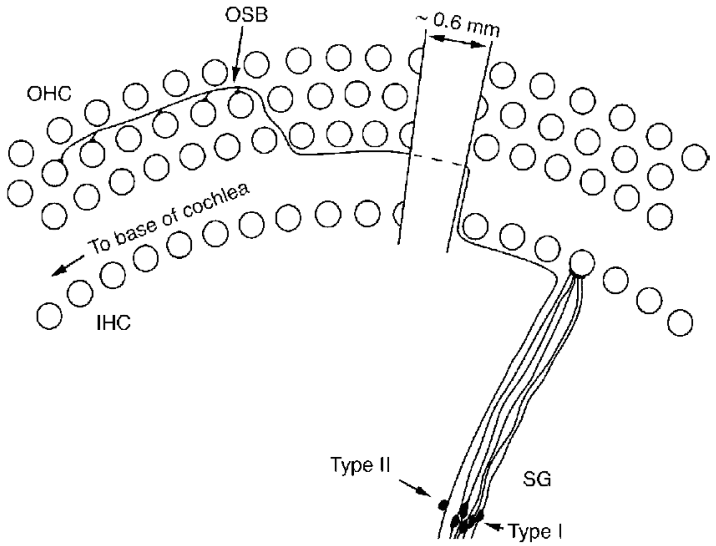

Figure 1.9: IHC and OHC connections to the auditory nerve fibers. Most of the auditory nerve fibers (type I) connect to IHC's. IHC, inner hair cells; OHC, outer hair cells; SG, spiral ganglion; OSB, outer spiral bundle. Reprinted with permission of the Brill Publishers, Figure 3.6 from Pickles (2013) ©2013.

Since Type I neurons have thick, myelinated axons they are capable of transferring the signals rapidly while Type II fibers are slow. Type I fibers are easier to record from, so their role on the conduction of the signal is known in detail. On the other hand recording from Type II fibers is more difficult. However, according to some anatomical observations their role is relatively minor compared to type I fibers (Schnupp *et al.*, 2011).

Many of these fibers exhibit spontaneous activity, which means even if there is no stimulation from the hair cells, there are spikes occuring. The spontaneous firing rate has a huge range of variation from as low as 0.5/sec to as high as 160/sec (Pickles, 2013).

AN fibers respond to pure tone stimuli and if there are no other stimuli present,

these responses are always excitatory. Taking a look at just one instance of a response to a stimulus might not explain the nature of the fibers response to it since there is random behaviour in the firing patterns of these fibers. Every other trial for the same procedure will give different results in terms of the exact spike times. But the behaviour of these fibers can be characterized using post-stimulus-time-histograms (PSTH), which are created by presenting the same stimulus multiple times and recording the number of spike occurance in the same time bin. With this approach, the patterns in the firing behaviour of the fibers can be observed. A typical PSTH of a single auditory nerve fiber (Fig. 1.10) to a tone burst shows a sharp increase in the activity to the onset of the stimulus. This response will then decrease slowly to a steady rate until the end of the stimulus (Pickles, 2013). The spike occurances in the bins where stimulus are not presented anymore are caused by the spontaneous firing of the fiber.

Another powerful tool for examining the behaviour of the ANFs is the tuning curve. Tuning curves are obtained by increasing the intensity of the tone burst until there is a detectable increase in the firing rate. Doing this for multiple frequencies will give the relationship between threshold and frequency. Fig. 1.11 shows different examples of tuning curves. From the figures it can be seen that different fibers have a tendency to fire more easily to a specific frequency. In other words, they are more responsive to that frequency than to the other stimulus frequencies. This frequency is known as the best frequency (BF) or characteristic frequency (CF) of that fiber. As the characteristic frequency of the fiber increases, the sharpness of its curve becomes more and more prominent on a log frequency scale, but in terms of absolute bandwith the frequency tuning decreases at higher CFs.

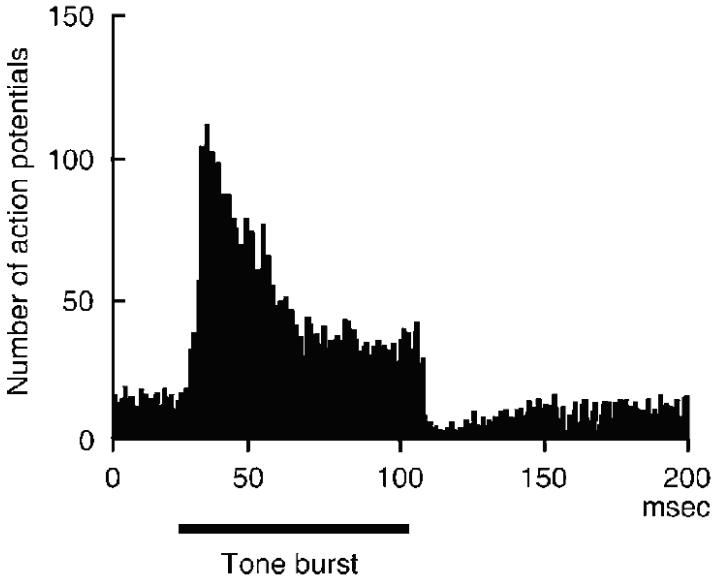

Figure 1.10: Recorded post-stimulus-time-histogram (PSTH) of an auditory nerve fiber stimulated with a tone burst. Reprinted with permission of the Brill Publishers, Figure 4.2 from Pickles (2013) ©2013.

Rate-level curves show firing rates as a function of stimulus intensity. For ANFs the function has a sigmoidal shape where fibers saturate above at 20-50dB their threshold. Below the CF, the slope of the response is steeper but for the above values the curve gets shallower. The spontaneous rate (SR) of the fiber also affects the slope of this curve. The slope gets shallower as the SR gets lower (Fig. 1.12).

The frequency resolution of ANFs for broadband stimuli and narrowband stimuli is similar. When a stimulus consists of multiple frequencies presented to ANF simultaneoulsy, depending on the CF of the fiber, the strength of the phase locking for individual frequency component of the stimulus would be different. A tuning curve can be constructed from this information. It is found that this type of tuning curve is similar to the ones constructed by presenting pure tone stimuli and measuring the threshold of the fibers response Pickles (2013). On the other hand when the stimulus

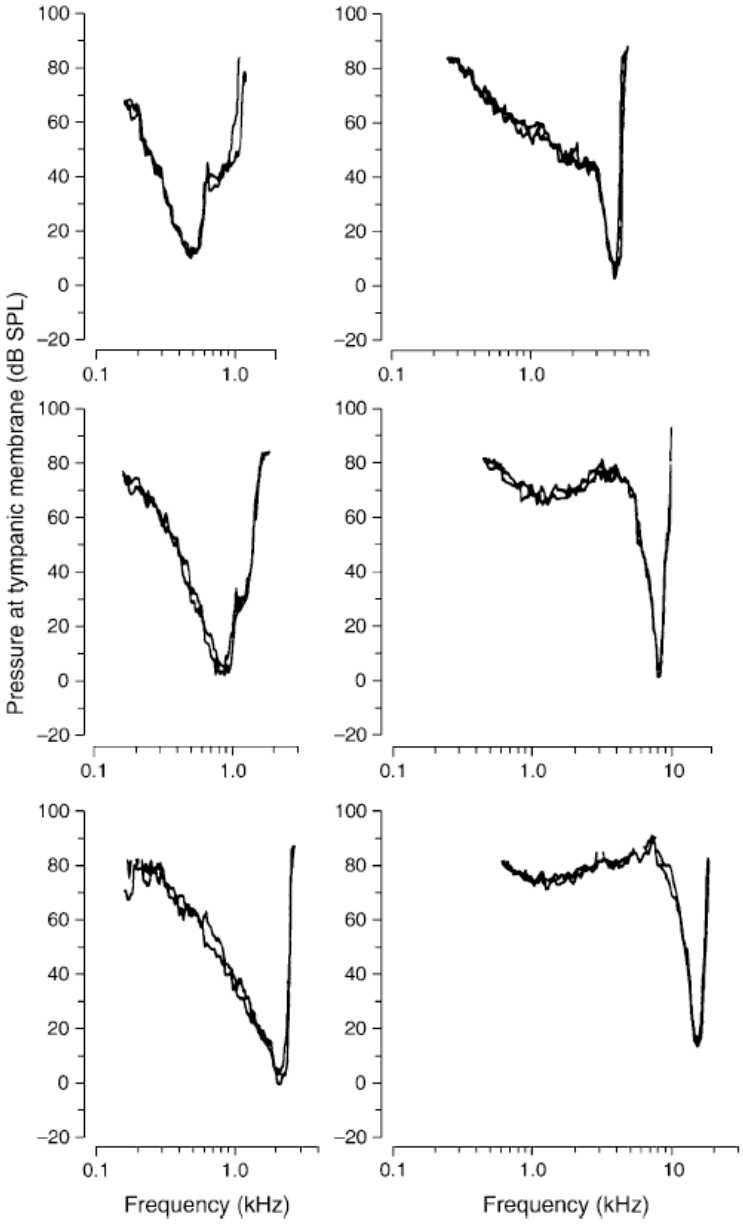

Figure 1.11: Tuning curves for different AN fibers. As the CF of the fiber gets higher the sharpness of the frequency selectivity feature is increased. Reprinted with permission of the Brill Publishers, Figure 4.3 from Pickles (2013) ©2013.

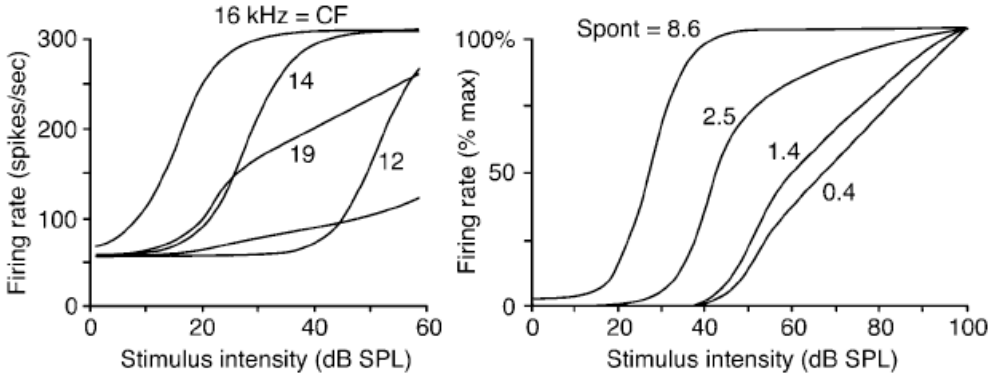

Figure 1.12: Rate-level curves of ANFs. Reprinted with permission of the Brill Publishers, Figure 4.6 from Pickles (2013) ©2013.

intensity increases the width of tuning curves gets wider. Although some level of frequency resolution is preserved, the sharp tuning response of the curve gets less prominent as the intensity increases.

1.3 Central Auditory System

The mammalian central auditory system incorporates multiple subcortical nuclei (Fig. 1.13). Each stage has different types of physiological and anatomical structures, therefore applying different types of processing to the neural representation of the sound signal propagated from lower stages of the auditory system. Features are progressively extracted at different stages in terms of identifying the sound content and localization of the source. Information is propagated through higher levels of the system in multiple parallel pathways. Later, these features are combined to create an 'auditory object' that can be defined as the representation of a sound in the brain grouped as coming from a common source.

Auditory nerve fibers enter the cochlear nucleus via the VIIIth cranial nerve and

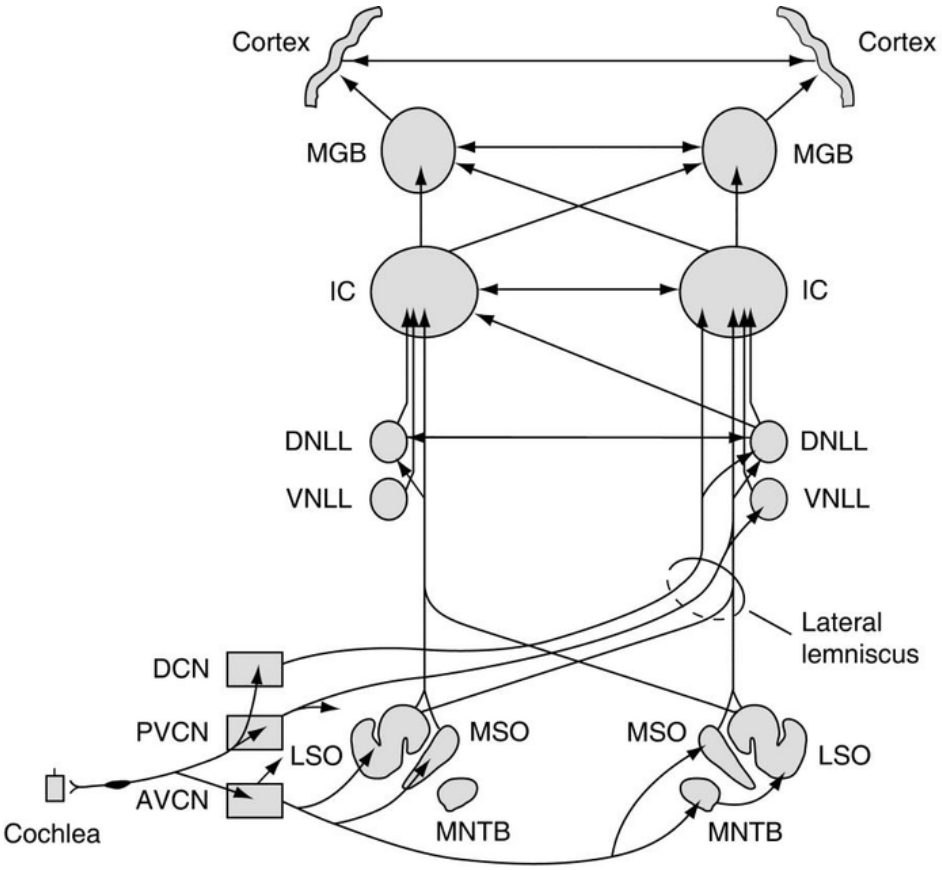

Figure 1.13: Main ascending pathways of the mammalian central auditory system. AVCN, anteroventral cochlear nucleus; PVCN, posterovenrtal cochlear nucleus; DCN, dorsal cochlear nucleus; LSO, lateral superior olive; MSO, medial superior olive; MNTB, medial nucleus of the trapezoid body; VNLL, ventral nucleus of the lateral lemniscus; DNLL, dorsal nucleus of the lateral lemniscus; IC, inferior colliculus; MGB, medial geniculate body. Reprinted with permission of the Brill Publishers, Figure 6.12 from Pickles (2013) ©2013.

bifurcate upon entrance. The ascending branch enters the anteroventral cochlear nucleus (AVCN) and the descending branch enters the dorsal cochlear nucleus (DCN) through the posteroventral cochlear nucleus (PVCN). Feature extraction starts in the cochlear nucleus. Then, localization and identification cues propagate to higher levels via several parallel pathways. Depending on the type of the cell they rise from, some of these streams are mainly responsible for carrying the sound identification features such as temporal variation and spectral information while others transfer fine timing information which is crucial for sound localization. AVCN mainly projects to the superior olivary complex while PVCN projects to ventral nucleus of the lateral lemniscus (VNLL) and superior olivary complex. The superior olivary complex is involved in the sound localization process by comparing the timing and intensity of inputs coming from both ipsilateral and contralateral VCN parts. On the other hand, DCN projects the vertical plane localisation cues to the contralateral inferior colliculus (IC). IC integrates the features which are propagated through parallel streams. The MGB acts like a relay structure: the ventral part of MGB projects the information coming from IC to the primary auditory cortex, while the medial and dorsal part of MGB projects to the area surrounding the primary auditory cortex.

Since this research is mainly focused on the ventral part of the cochlear nucleus, processing in the other areas of the central auditory system are not going to be explained further.

1.4 Cochlear Nucleus

The cochlear nucleus is the first stage in the central auditory system that the auditory nerve fibers make connections to. Based on the anatomical, physiological structure

and functionality, the nuclei are divided into two main parts: dorsal and ventral. The ventral side of the cochlear nucleus is further divided into anterior and posterior parts. The frequency mapping introduced in the basilar membrane is reflected in the cochlear nucleus by the pattern of innervation of the AN fibers. The main physiological structure and the tonotopic mapping of the cochlear nucleus is shown Fig. 1.14. From the figure it can be seen that the DCN has more capability to do higher frequency processing than VCN (Ryugo and Parks, 2003).

Auditory nerve fibers have similar physiological properties, therefore modelling their behaviour as a population can be achieved by adding small variations to the same type of model. In contrast, the cochlear nucleus has several different type of cells which show different behaviours. This diversity makes the cochlear nucleus an important feature extractor. Each cell type selectively emphasizes different aspects of the sound signal to form sound localization, temporal fluctuations and frequency spectrum cues (Pickles, 2013). However, the processing applied to elevate one aspect of the sound usually degrades the other features of the sound signal. For example, to locate the source of a sound signal, exact timing cues from both ears is needed for comparison. There are different type of cells in the CN which contribute to enhancing the timing information. However while this cue is extracted by these cells by firing primarily on the onset of the signal, the complex spectral information is lost. Therefore, the multiple parallel pathways of the CN using different cell types is an advantage. The distinction between the functions of these parallel pathways (i.e. sound identification and sound localization cues) becomes less prominent as features reach to the upper levels of central auditory system since the features are combined and get more complex in structure.

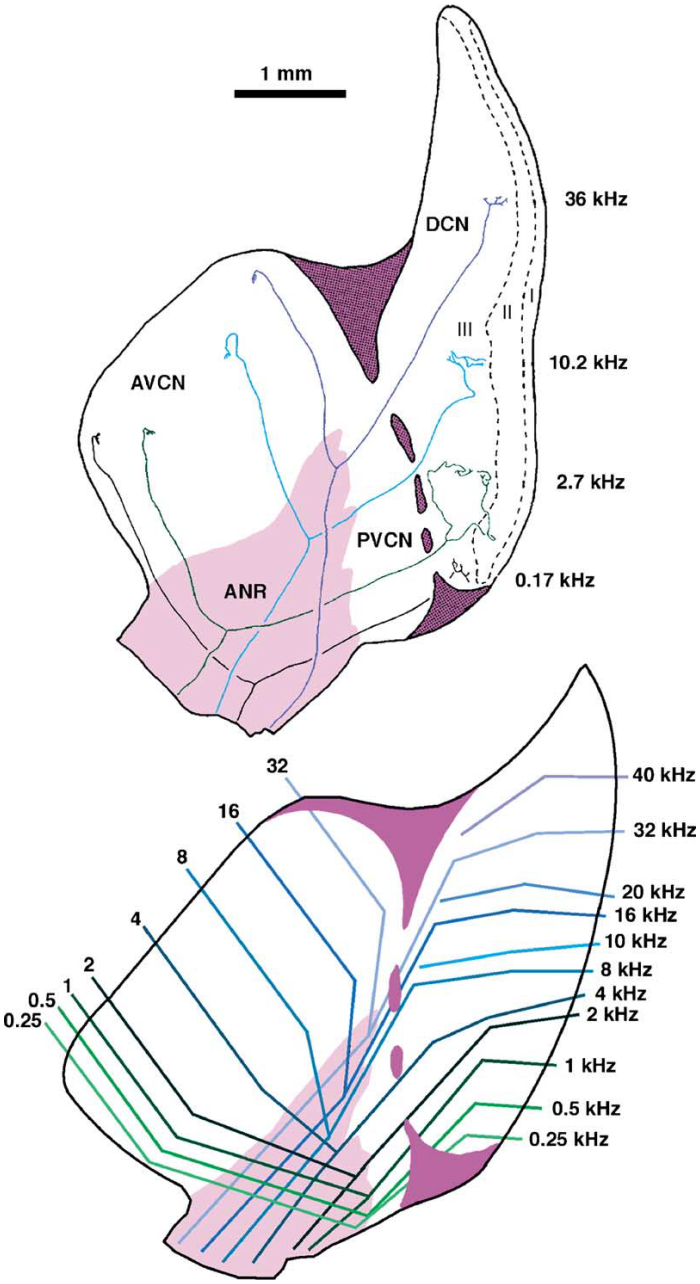

Figure 1.14: Three main compartments of the mammalian cochlear nucleus. The projection of afferent AN fibers and the tonotopic mapping is also shown. ANR, auditory nerve root; AVCN, anteroventral cochlear nucleus; DCN, dorsal cochlear nucleus; PVCN, posteroventral cochlear nucleus. Reprinted from Ryugo and Parks (2003) ©2003, with permission from Elsevier.

There are two main methods of classification of cell response types in the cochlear nucleus: PSTH based and response map based schemes. These methods emphasize different aspects of the responses. PSTH based classification shows the temporal firing patterns of the cell, while response maps emphasize more on receptive field properties that shows the excitatory and inhibitory frequency bands (Shofner and Young, 1985). Different behaviours of PSTHs shown by VCN cells can be seen in Fig. 1.15.

Another useful tool to investigate the response behaviour of cells is the coefficient of variation (CV). It is calculated by taking the ratio of the standard deviation of inter spike intervals (ISI) with respect to mean ISIs. CV shows the irregularity of the firing patterns of cells' reponses to tone bursts. Young *et al.* (1988) investigate the VCN cells' regularity of firing and showed that it is a useful tool to distinguish different type of cells.

Chopper type cells exhibit regular firing responses with consistent intervals to a stimuli regardless of its frequency (Rhode and Smith, 1986). This chopping behaviour may persist through the response or it can attenuate through time and is followed by random firing behaviour. Chopper responses are the most common firing behaviour seen in the VCN, and they are produced by stellate cells (Feng *et al.*, 1994; Oertel, 1983). For positive square wave intracellullar current injections the cells respond with regularly spaced action potentials (Oertel, 1983). This firing behaviour and its relation to the amplitude of input can be seen in Fig. 1.16.

Primary-like responses show a sharp onset component and exponential decay to a steady firing rate like those seen in AN fiber firing. Primary-like with notch behaviour is similar to the primary-like but there is a brief notch after the onset. This notch is a result of the refractoriness. Primary-like and onset type of units have similar

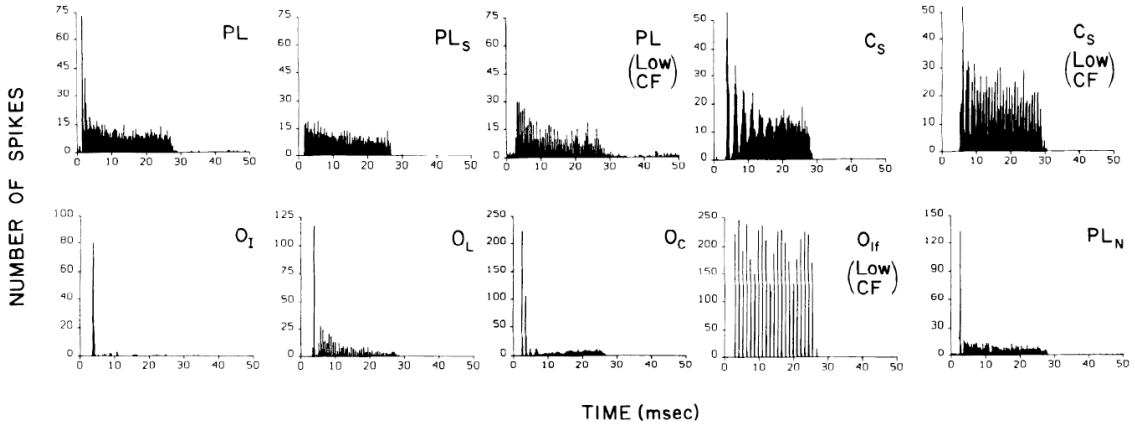

Figure 1.15: Several distinct PSTH types seen in VCN cells. PL: primary-like pattern; PL_s: primary-like pattern seen in auditory nerve fibers with low spontaneous firing rates (SR near zero); PL (low CF): primary-like response showing phase locking; C_s: sustained chopper; C_s (low CF): sustained chopper showing phase locking; O_I: onset response; O_L: onset response with small amount of late activity; O_C: onset unit with initial chopper behaviour; O_{lf}: onset unit with low CF; PL_N: primary-like with notch. Reprinted with permission of The American Physiological Society, from Rhode and Smith (1986) ©1986.

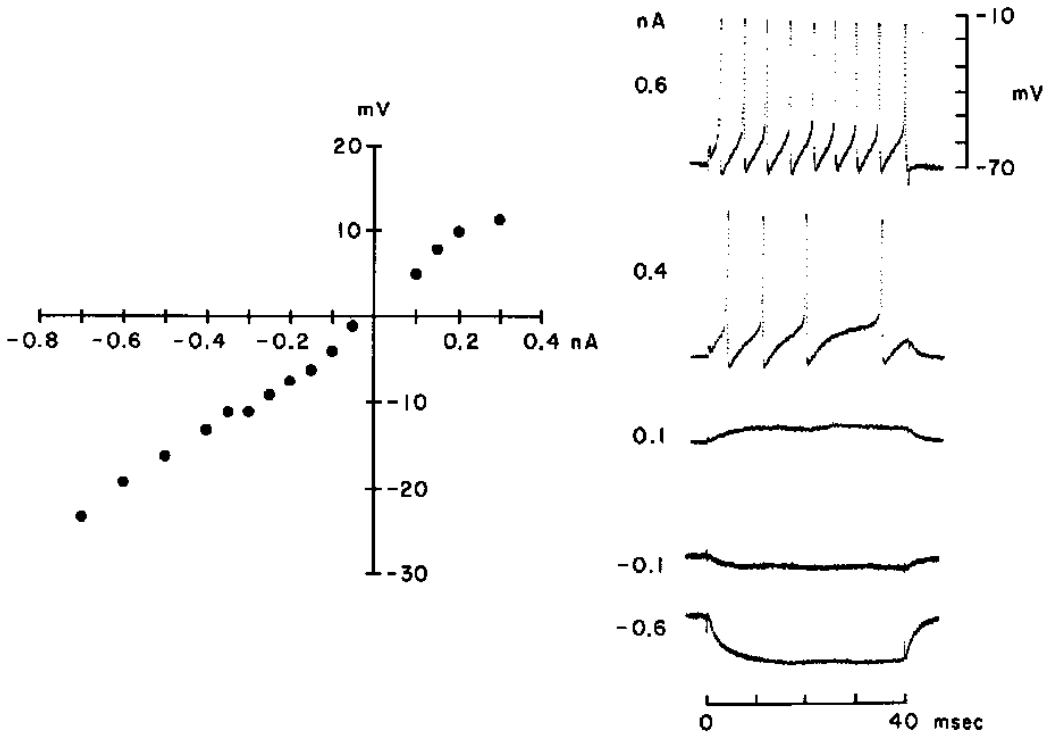

Figure 1.16: Current-voltage relationship of stellate cells. Until a threshold of 0.3 nA, the current and membrane voltage has fairly linear relationship. When the 0.3 nA threshold is exceeded the cell begins to fire regularly. The frequency of firing is proportional to the the magnitude of input current pulse. Republished with permission of Society for Neuroscience, from Oertel (1983) ©1983; permission conveyed through Copyright Clearance Center, Inc.

responses. The difference is onset type cells do not fire as much as primary-like cells after the initial spike. Onset type cells divide into subtypes: O_I, O_L and O_C. Although these subtypes' responses are not diverse from each other too much, including them in this chapter is important in terms of explaining the diversity of responses of cells in VCN. O_I is the classic onset type response. O_L presents small amount of late activitiy after the initial spike. O_C is an onset unit with a weak chopping behaviour after the initial spike. Both onset and primary-like cells show strong phase-locking behaviour which helps preserve timing information. This information is used for sound location estimation by the upper stages of the central auditory system. Bushy cells shows primary-like type of behaviour (Feng *et al.*, 1994; Rhode *et al.*, 1983; Rhode and Smith, 1986). Intracellular recordings done by Oertel (1983) are shown in Fig. 1.17.

In this study, mostly PSTH based methods are conducted so the emphasis will be more on this method instead of response maps in following sections.

1.4.1 Projections of the Cochlear Nucleus to the Central Auditory System

Specific cell types in the cochlear nucleus project to a specific parts in the upper levels of central auditory system (Cant and Benson, 2003). These pathways are mapped by injecting intracellular tracers and checking the axonal branching patterns or using extracellular tracing techniques. The projections of cochlear nucleus can be seen in Fig. 1.18.

Cells types are named according to the studies of Osen (1969) and Brawer *et al.* (1974). In the ventral side of CN main cell types are identified as bushy cells (spherical and globular), multipolar or stellate cells (d-stellate and t-stellate), octopus cells,

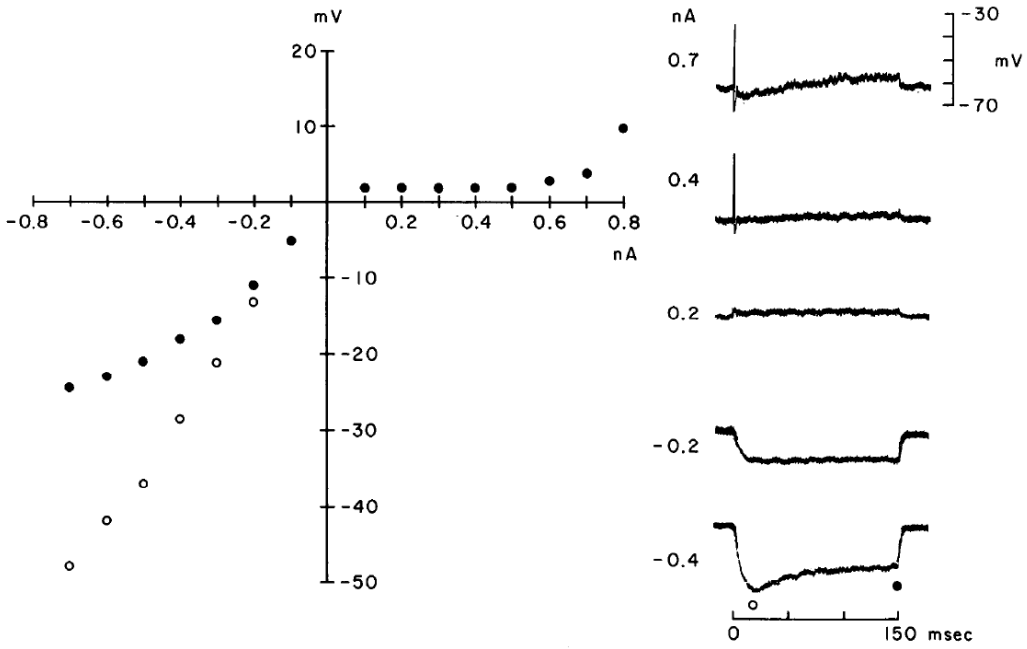

Figure 1.17: Current voltage relationship of bushy cells. After the threshold value, the cell fires only at the beggining of the stimuli and after that the membrane voltage returns to a steady state value proportional to the magnitude of external current input. The black dots indicate the final value of the membrane voltage at the end of the stimuli while the white dots shows the peak voltage of the hyperpolarization. Republished with permission of Society for Neuroscience, from Oertel (1983) ©1983; permission conveyed through Copyright Clearance Center, Inc.

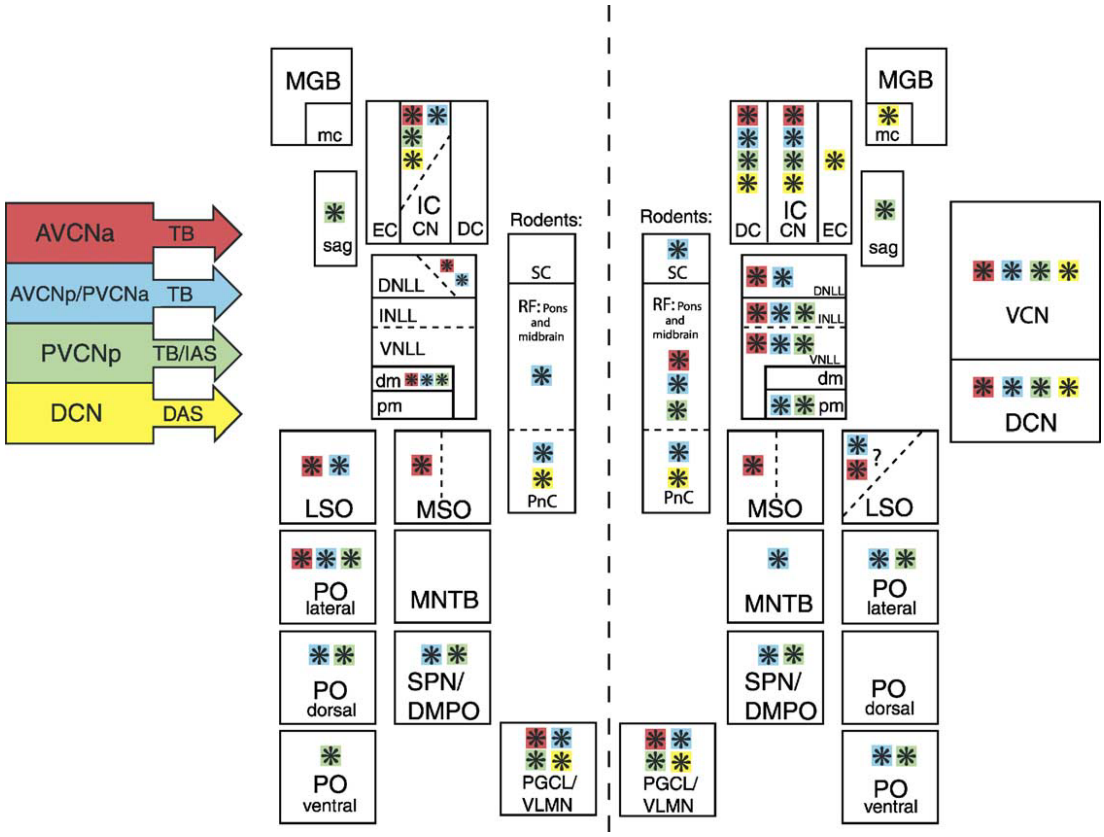

Figure 1.18: The cochlear nucleus' projections to the ascending auditory pathways. AVCNa, anterior part of the anteroventral cochlear nucleus; AVCNp, posterior part of the anteroventral cochlear nucleus; CN, central nucleus of the inferior colliculus; DAS, dorsal acoustic stria; DC, dorsal cortex of the inferior colliculus; DCN, dorsal cochlear nucleus; DMPO, dorsomedial periolivary nucleus; DNLL, dorsal nucleus of the lateral lemniscus; EC, external cortex of the inferior colliculus; IAS, internal acoustic stria; IC, inferior colliculus; INLL, intermediate nucleus of the lateral lemniscus; LSO, lateral superior olivary nucleus; mc, magnocellular division of the medial geniculate body; MGB, medial geniculate body; MNTB, medial nucleus of the trapezoid body; MSO, medial superior olivary nucleus; PGCL, lateral paragigantocellular nucleus; PnC, caudal pontine reticular nucleus; PnO, oral pontine reticular nucleus; PO, periolivary nuclei; pm, posteromedial part of the ventral nucleus of the lateral lemniscus; PVCNa, anterior part of the posteroventral cochlear nucleus; PVCNp, posterior part of the posteroventral cochlear nucleus; sag, sagulum; SC, superior colliculus; SPN, superior paraolivary nucleus; TB, trapezoid body; VCN, ventral cochlear nucleus; VLMN, ventrolateral medullary nucleus; VLTg, ventrolateral tegmental area; vm, ventromedial part of the ventral nucleus of the lateral lemniscus; VNLL, ventral nucleus of the lateral lemniscus. Reprinted from Cant and Benson (2003) ©2003 with permission from Elsevier.

small cells and granule cells. In the dorsal part, fusiform cells, giant cells, granule cells and some types of small cells can be found. The classification of these cells are based on their distinct morphologies and their response to tone stimuli. Projections of these various cell types to the central auditory system are shown in Fig. 1.19.

1.4.2 Principal Cells of the Ventral Cochlear Nucleus

1.4.2.1 Bushy Cells

Bushy cells have big round cell bodies with short dentritic branches which gives the dentritic tree a 'bushy' look. (Fig. 1.20). Two types of bushy cells are identified in the VCN according to the shape of their somas: spherical bushy cells and globular bushy cells. Spherical bushy cells are also divided into two groups: large spherical bushy cells which take their inputs from lower frequency AN fibers and small spherical bushy cells which takes a full range of inputs from the cochlea.

Spherical bushy cells receive their excitatory AN inputs from a specialized synaptic connection called the Calyx of Held. This glutamatergic synapse has high number of synaptic release sites and is able to succesfully follow rates of synaptic input. Therefore it allows the postsynaptic neuron to follow the firing pattern of the presynaptic neuron. When depolarized, the membrane resistance decreases for bushy cells which results in a decrease in membrane time constant. This aspect of bushy cells is associated with low-threshold-conductance potassium channel and is not in favor of repetitive firing (Feng *et al.*, 1994). However bushy cells can show irregular firing activity after the initial spike. This firing behaviour does not show any relation with the level of stimuli and might be related with the spontaneous firing of the cell. Combining all of these aspects together, bushy cells show primary-like responses. The

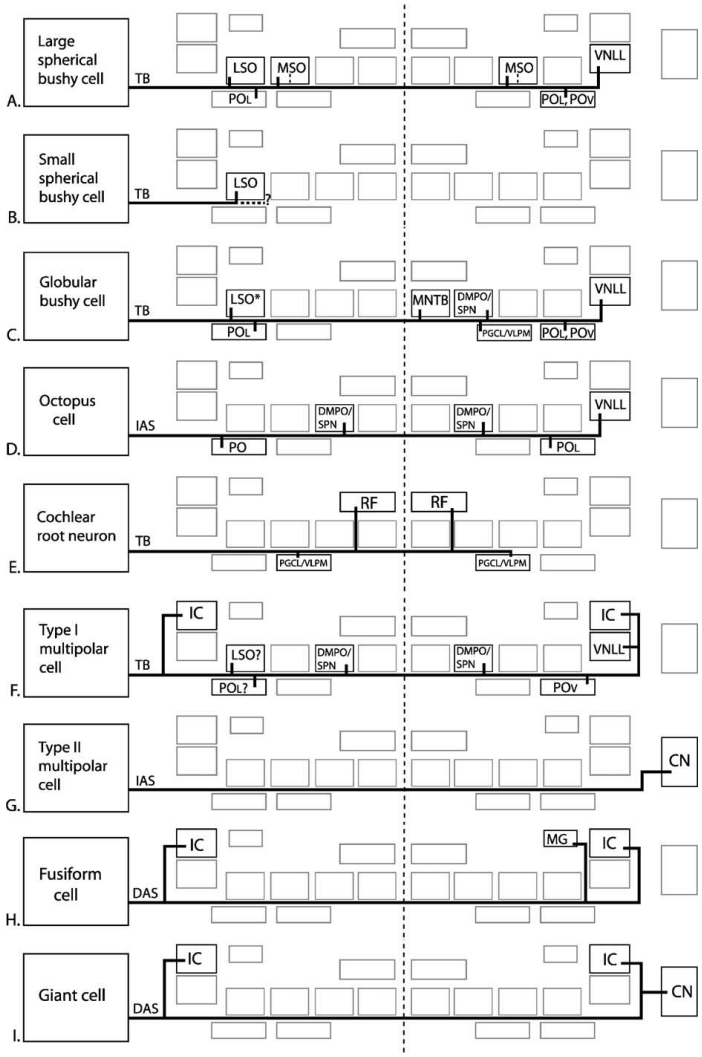

Figure 1.19: Specific CN cell types' projections to the central auditory system. Abrevations are the same with previous figure with additions of; POL, lateral periolivary group; POV, ventral periolivary group. Reprinted from Cant and Benson (2003) ©2003, with permission from Elsevier.

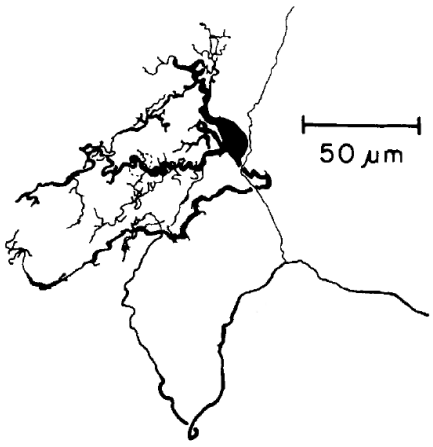

Figure 1.20: Camera lucida drawing of bushy cell morphology. Reprinted with permission of John Wiley and Sons, from Rhode *et al.* (1983) ©1983.

CV of these units are large which means the regularity of the firing is low. This can be seen in the middle column of Fig. 1.21. Spherical bushy cells are also targeted by glysinergic or GABAergic inhibitory inputs. These inputs are argued to adjust the gain of the responses to AN inputs (Caspary *et al.*, 1994). Globular bushy cells exhibit a primary-like with notch PSTH profile. There are on the order of 36600 spherical bushy cells and 6300 globular bushy cells in the VCN (Young and Oertel (2004)).

1.4.2.2 Stellate Cells

Identified as multipolar cells before, stellate cells have multiple dentrites extending away from their soma in multiple directions. Stellate cells have two main types; T stellate cells (also identified as Type I multipolar or planar cells) whose main axons project through the **T**reapezoid body, and D stellate cells (also identified as Type II multipolar or radiate cells) that project **D**orsalward. T stellate cell dentrites project

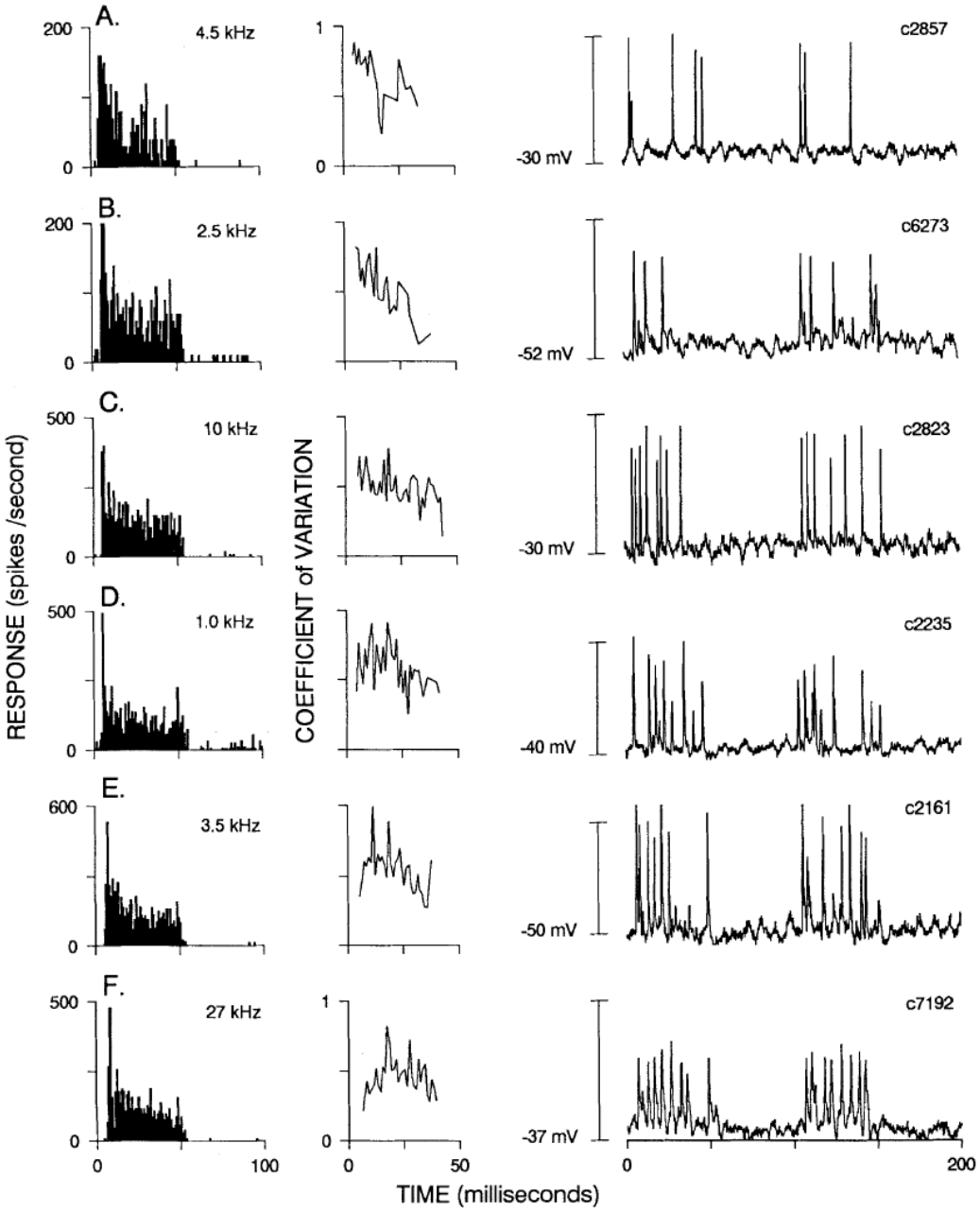

Figure 1.21: Some examples of bushy cell firing behaviour to different frequencie stimuli. As the frequency of the stimulus increase the primary like behaviour becomes more prominent. The middle column shows the CV of cells. The right column shows the irregularity of the firing response to two same tone bursts presented back to back to the same cell. Reprinted with permission of John Wiley and Sons, from Feng *et al.* (1994) ©1994.

parallel with AN fibers and end with highly branced tips. D stellate cell dentrites are not aligned with AN fiber directions. Some D stellate and T stellate cell morphology and current evoked responses are shown in Fig. 1.22.

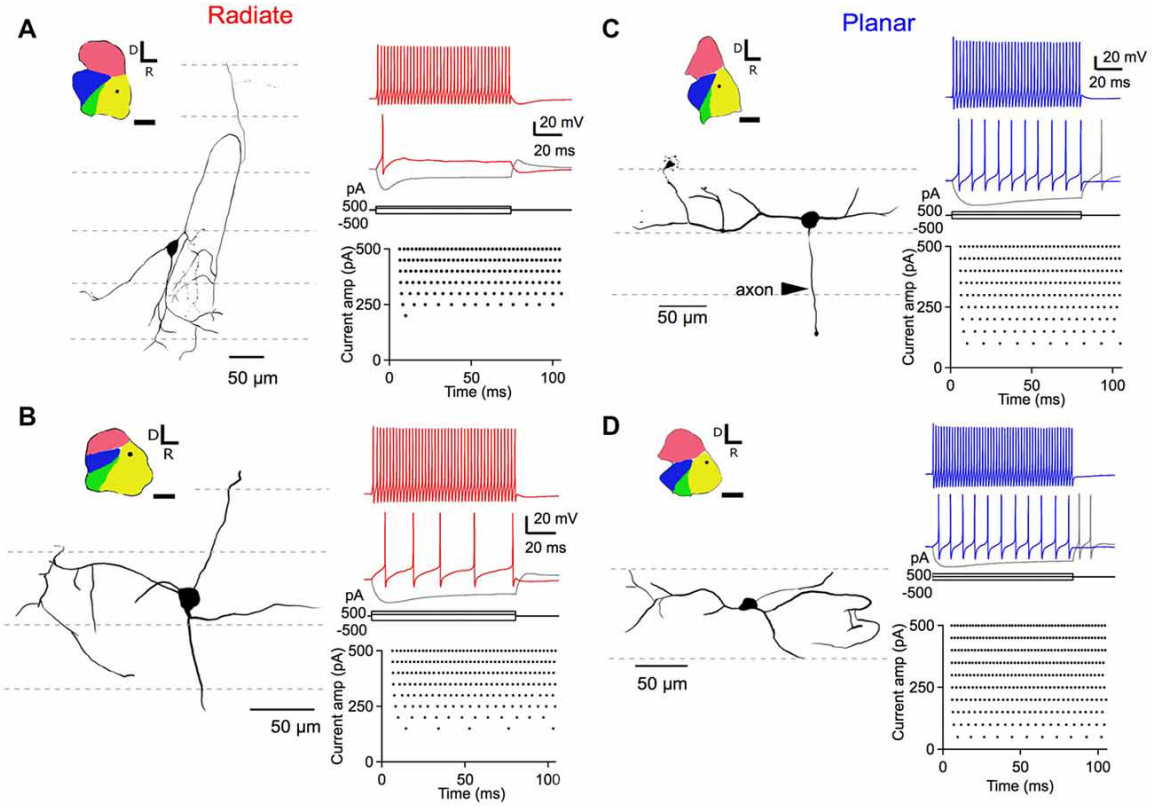

Figure 1.22: Examples of D stellate (radiate) and T stellate (multipolar) cell morphology and current evoked responses. Left column shows drawings of cell morphology and locations in AVCN. Dots in yellow areas show the location of the cell. Dashed lines represents the direction of ANFs. Right column shows the response of cells to 500 pA, 200 pA and -500 pA current injections. Raster plots are also included to show the regularity of spiking. From Xie and Manis (2017).

T stellate cells exhibit onset behaviour and are excitatory, while D stellate show onset chopper behaviour and are inhibitory (Rhode *et al.*, 1983; Young and Oertel, 2004). D stellate cells receive more broadly tuned inputs then T stellate cells. D stellate cells are innervated almost entirely by AN fibers, while T stellate cells receive

their narrowly tuned excitatory input from AN fibers and other T stellate cells. T stellate cells receive inhibitory inputs from D stellate cells and tuberculoventral cells of the DCN. T stellate cells have larger input resistance, so small changes in the input current produce large voltages that might result in the cell firing. T stellate cells lack the low-voltage-activated potassium channels that hinder repetitive firing in bushy cells. Experiments done on T stellate cells show that they have less synaptic depression which makes them less adaptive. All of these factors contribute to the repetitive firing behaviour of T stellate cells.

T stellate cells fire tonically to incoming stimuli. As the stimulus intensity increases, the frequency of firing also increases and the firing rate of T stellate cells are almost constant. These tonical firing properties makes T stellate cells suitable for propagating the envelope information of the sound signal that is important for speech recognition.

D stellate cells have higher current thresholds than T stellate cells that makes them less excitable. As a result of this property, D stellate cells require powerful or broadband input stimuli to evoke an action potential. This is consistent with the hypothesis that D stellate cells integrate large number of weak AN inputs coming from a range of CFs to provide robust inhibition (Xie and Manis, 2017).

There are on the order of 9400 stellate cells in the VCN. The ratio of T stellate to D stellate cells is about 15:1 (Young and Oertel, 2004).

1.4.2.3 Octopus Cells

Octopus cells (Fig. 1.23) have two to three big dentrites running perpendicularly across multiple AN fibers that indicates they are getting broadly tuned inputs like D

stellate cells. But unlike D stellate cells, octopus cells show an onset type response. Octopus cells exhibit a tightly locked spike to the onset of the stimulus. After the initial spike, the membrane voltage stays in a depolarized state until the end of stimulus (Fig. 1.24). Like bushy cells, octopus cells have low input resistance that make it sensitive only to inputs coming at the same time (synchronous).

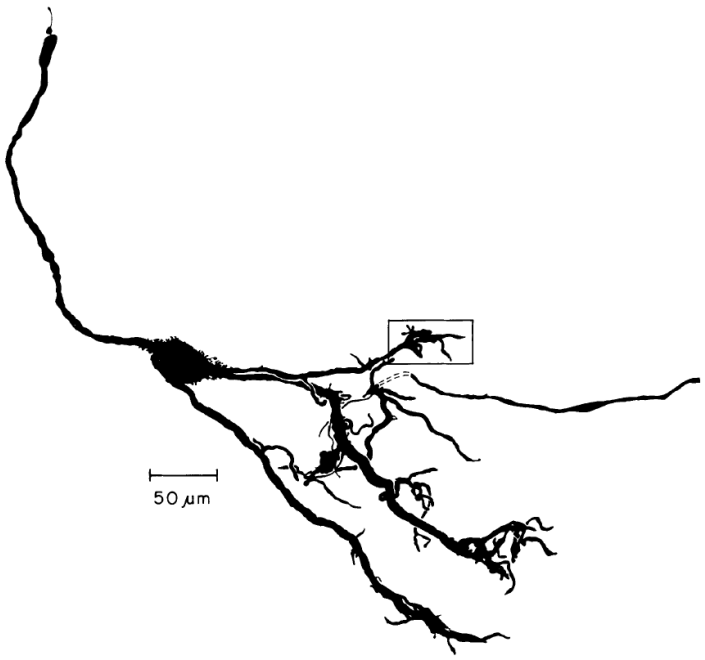

Figure 1.23: Camera lucida drawing of an octopus cell. Reprinted with permission of John Wiley and Sons, from Rhode *et al.* (1983) ©1983.

1.5 Neural Modelling

Nerve cells receive their inputs through their dendrites. When these inputs causes the membrane potential to exceed a certain threshold, the cell produces an action potential (AP), which is also referred to as a spike. The underlying mechanism of creation of these APs can be understood by inspecting ionic changes governed

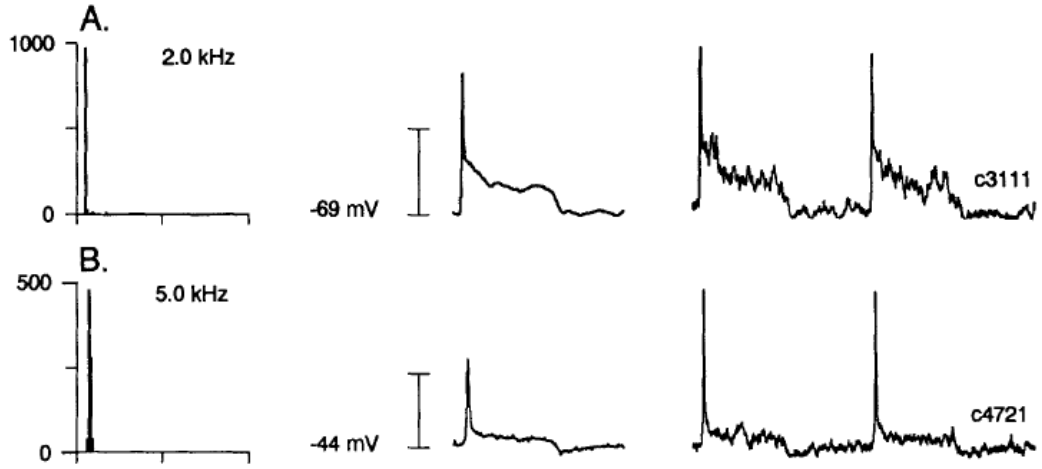

Figure 1.24: Octopus cell response. Left column shows the PSTH of the response to stimuli with 75 and 25 repetitions respectively. The middle column shows the depolarization behaviour of the membrane after initial spike. Right column shows the response to two tones presented back to back. Reprinted with permission of John Wiley and Sons, from Feng *et al.* (1994) ©1994.

by channels in the membrane. In 1952, by using voltage clamping techniques and blocking specific types of ion channels with pharmacological agents on squid giant axon, Hodgkin and Huxley came up with a quantitative model (Fig. 1.25) that explained the characteristics of membrane voltage changes.

According to Hodgkin and Huxley, the total membrane current can be defined as the summation of ionic and capacitive currents,

$$I_{\mathrm{m}}(t) = I_{\mathrm{ionic}}(t) + C_{\mathrm{m}}\frac{dV(t)}{dt}. \tag{1.1}$$

The ionic current consists of two major time and voltage dependent ionic currents, Na^+ and K^+, and a leakage current;

$$I_{\mathrm{ionic}}(t) = I_{\mathrm{Na^+}} + I_{\mathrm{K^+}} + I_{\mathrm{Leak}}, \tag{1.2}$$

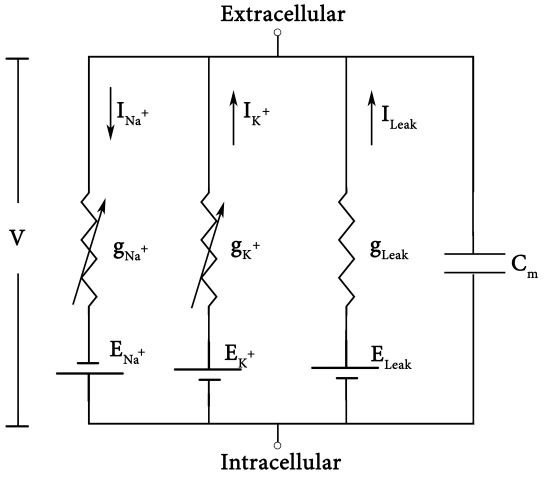

Figure 1.25: Equivalent circuit model of Hodgkin-Huxley model. g_{Na^+} and g_{K^+} are voltage dependent sodium and potassium conductances, C_{m} is membrane capacitance, E_{Na^+}, E_{K^+} and E_{Leak} is reversal potentials.

while the change in the individual ionic currents is governed by;

$$I_{\mathrm{i}}(t) = g_{\mathrm{i}}(V(t), t)(V(t) - E_{\mathrm{i}}), \tag{1.3}$$

where E_{i} is the reversal potential of that particular ion, and g_{i} is the conductance of the ion channel that depends on time and the membrane voltage.

According to the model, the ionic potassium current can be described as;

$$I_k(t, V) = g_k(t, V)(V - E_k) \tag{1.4}$$

The conductance of the potassium channel is:

$$g_{\mathrm{K}}(t, V) = \overline{g}_{\mathrm{K}} n^4(t, V). \tag{1.5}$$

The ionic conductance g_{K} is defined by a maximum conductance value $\overline{g}_{\mathrm{K}}$ multiplied by a *gating particle* that indicates the fraction of open ion channels.

The rate of change of the activating gating particle n is defined by,

$$\frac{dn}{dt} = \frac{n_\infty - n}{\tau_{\mathrm{n}}}, \tag{1.6}$$

where n_∞ is the steady state value of the gating particle and τ_n is the time constant:

$$\tau_n = (\alpha_n + \beta_n)^{-1}. \tag{1.7}$$

The rate constants α_n and β_n can be defined as:

$$\alpha_n = \frac{0.01(10 - V)}{\exp\frac{10 - V}{10} - 1} \tag{1.8}$$

$$\beta_n = 0.125\exp\frac{-V}{80} \tag{1.9}$$

The same set of equations can be written for Na^+ current as,

$$I_{\mathrm{Na^+}}(t, v_m) = g_{\mathrm{Na^+}}(t, V)(V - E_{\mathrm{Na^+}}) \tag{1.10}$$

$$g_{\mathrm{Na^+}}(t, V) = \overline{g}_{\mathrm{Na^+}} m^3(t, V) h(t, V) \tag{1.11}$$

The difference for the Na+ ion channel is that the conductance is governed by two gating particles m and h. m is an activation particle and h is an inactivation particle. For a depolarizing input, the h particle closes the channel and m particle opens the

channel. All three m particles and the h particle have to be open for the channel to conduct.

$$\frac{dm}{dt} = \alpha_m(1-m) - \beta_m m \tag{1.12}$$

$$\frac{dh}{dt} = \alpha_h(1-h) - \beta_h h \tag{1.13}$$

$$m_\infty = \frac{\alpha_m}{\alpha_m + \beta_m} \tag{1.14}$$

$$\tau_m = (\alpha_m + \beta_m)^{-1} \tag{1.15}$$

$$h_\infty = \frac{\alpha_h}{\alpha_h + \beta_h} \tag{1.16}$$

$$\tau_h = (\alpha_h + \beta_h)^{-1} \tag{1.17}$$

$$\alpha_m = \frac{0.01(25-V)}{\exp\frac{25-V}{10} - 1} \tag{1.18}$$

$$\beta_m = 4\exp\frac{-V}{18} \tag{1.19}$$

$$\alpha_h = 0.07exp\frac{-V}{20} \tag{1.20}$$

$$\beta_h = \frac{1}{exp\dfrac{30 - V}{10} + 1} \tag{1.21}$$

The change in the activating and inactivating gating particles of K^+ and Na^+ ionic currents are shown in Fig. 1.26.

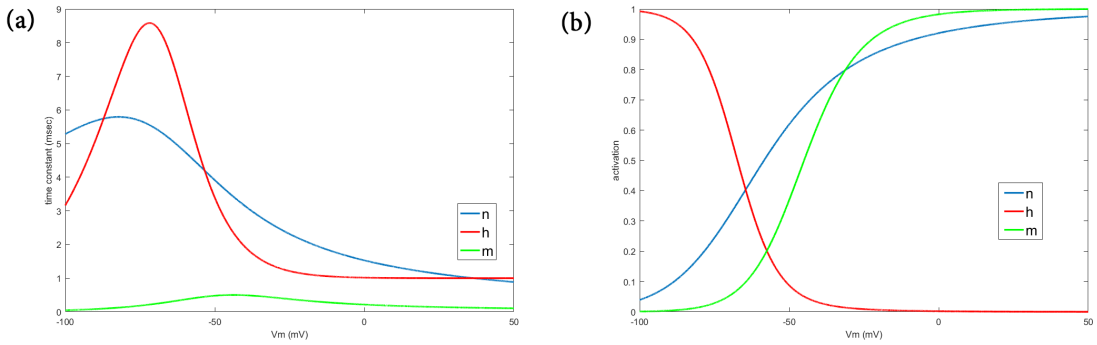

Figure 1.26: The change in the (a) time constants and (b) steady state values of the gating particles regarding to the change membrane voltage.

All of these individual components are summed to calculate the membrane potential for the Hodgkin-Huxley model,

$$C_m \frac{dV}{dt} = \overline{g}_{\mathrm{Na}} m^3 h (E_{\mathrm{Na}} - V) + \overline{g}_{\mathrm{K}} n^4 (E_{\mathrm{K}} - V) + \overline{g}_{\mathrm{leak}} (V_{\mathrm{rest}} - V) + I_{\mathrm{inj}}(t) \tag{1.22}$$

where C_m is the membrane capacitance, $\overline{g}_{\mathrm{leak}}$ represents the membrane leakage conductance, V_{rest} is the membrane resting potential and I_{inj} is the injected current. Hodgkin and Huxley assigned parameter values such as $E_{\mathrm{K}} = 50$ mV, $E_{\mathrm{Na}} = -77$ mV, $E_{\mathrm{rest}} = -54.4$ mV and $\overline{g}_{\mathrm{K}} = 36$ mS/cm^3, $\overline{g}_{\mathrm{Na}} = 120$ mS/cm^3, $\overline{g}_{\mathrm{leak}} = 0.3$ mS/cm^3 to match model responses with the physiological data. The K^+ current depolarizes the membrane ($E_{\mathrm{K}} = 50$ mV) while Na^+ current hyperpolarizes ($E_{\mathrm{Na}} = -77$ mV) it.

This model can reproduce various phenomena of the membrane potential and

can be tested for different inputs such as direct current injection, synaptic inputs etc. Although it is a computationally expensive model, since it succesfully captures the membrane voltage behaviour, it has been used extensively for modelling neural dynamics.

1.6 Synaptic Modelling

In the Hodgkin-Huxley model, voltage gated ion channels located in the membrane are modelled. But in the membrane of the nerve cells there are several other different types of ion channels. One of the most important type of channel is the synaptic channel that allow for inter-neuron communication and computation.

The synaptic process consist of several stages. After the action potential travels along the axon of the presynaptic cell it reaches a synaptic terminal. At this location neurotransmitters are released into the synaptic cleft between the presynaptic cell and the post-synaptic cell. These neurotransmitters then bind to the receptors on the dentrites of the postsynaptic cells. Depending on the transmitter type, the connection between pre and post synaptic cells are excitatory or inhibitory. The main transmitters used by cortical neurons are GABA (inhibitory) and glutamate (excitatory).

The synaptic conductance can be modelled as:

$$I_{\text{syn}}(t) = g_{\text{syn}}(t)(V - V_{\text{rev}}), \tag{1.23}$$

where V is the membrane voltage and V_{rev} is the reversal potential. Unlike the voltage-gated ion channels mentioned before, g_{syn} is dependent on the state of the presynaptic

neuron that depends on the transmission and binding of neurotransmitters at the postsynaptic cell.

The most common way to model the change in g_{syn} is changing by the conductance only when a presynaptic neuron spikes. Each spike alters this conductance, which can be modelled as an exponential function. This assumption is based on the whole cell excitatory-post-synaptic-current (EPSC) and inhibitory-post-synaptic-current(IPSC) recordings from neurons showing such exponential behaviour shown in Fig. (1.27). Depending on the receptors mediating the post-synaptic currents, this exponential change can be fitted as a first order exponential decay, alpha functions or double exponential functions. AMPA and GABA_A receptors has fast kinetics with lower rise and decay times. Therefore modelling them with a first order exponential decay is appropriate. On the other hand NMDA mediated currents has fast rise time and slow decay time while GABA_B mediated currents are observed to have long rise and decay time.

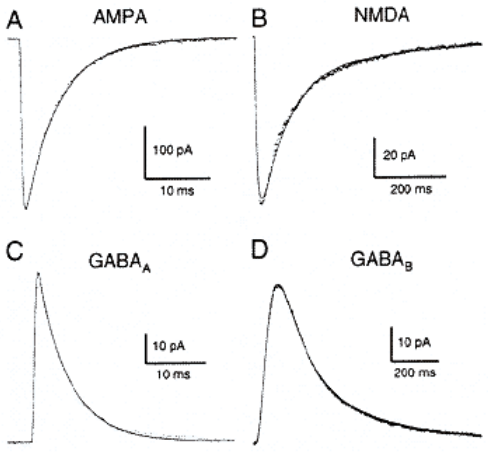

Figure 1.27: Whole cell recordings of AMPA, NMDA, GABA_A and GABA_B mediated currents. Reprinted with permission of the MIT Press, Figure 1.2 from Koch and Segev (1998) ©1998.

In most of the cases, postsynaptic neurons get their inputs from multiple presynaptic neurons. For these cases, the change in conductance can be modelled by adding each neuron's spike train outputs together and convoluting them with the exponential functions depending on the nature of the synaptic input (Fig. 1.28).

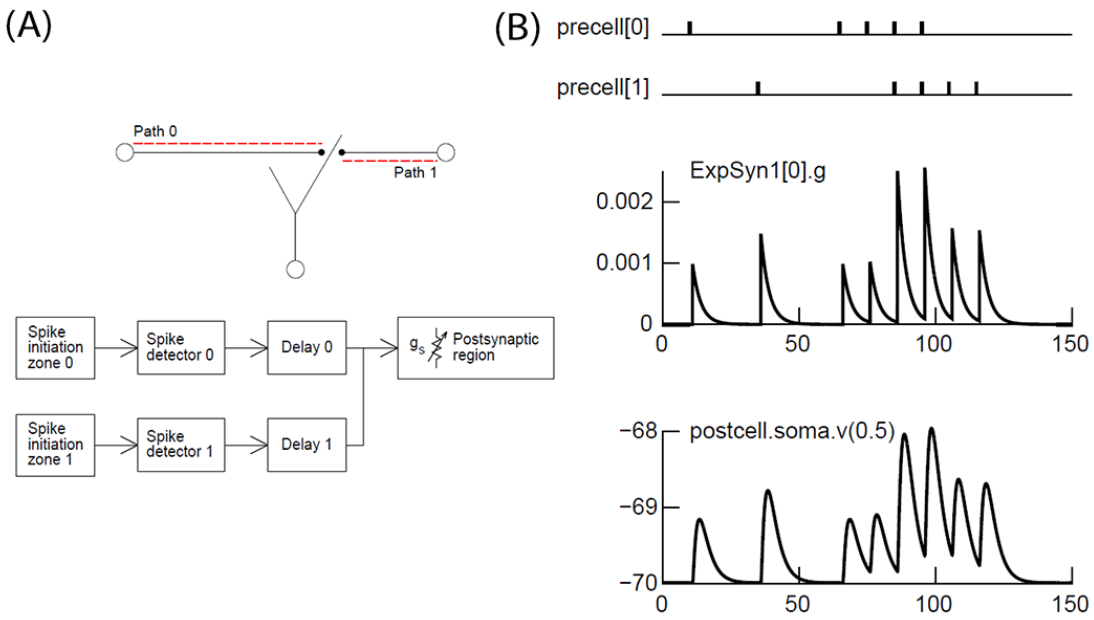

Figure 1.28: (A) Modelling the synaptic convergence. Inputs coming from different sources connects to different points at the dentrites of postsynaptic neuron. This can be modelled as sum of outputs of presynaptic neurons that are represented as delayed spike trains. (B) A demonstration of synaptic processing. Two inputs are summed and convoluted with and exponential function and given the Hodgkin - Huxley type neuron as input. The resulting membrane voltage change can be seen at the bottom figure. Reprinted with permission of Cambridge University Press through PLSclear, from Carnevale and Hines (2006) ©2006.

Chapter 2

Modelling Background

2.1 Auditory Periphery Model

To create detailed neural network models that are capable of capturing the behaviour of the cochlear nucleus, one has to incorporate realistic models of the earlier stages in the auditory system. Auditory periphery modelling is a well established research area that has decades of history. The mechanical processes of middle ear, the non-linearity of the cochlea and the synapse mechanism between hair cells and AN has been inspected through various in vivo acoustical experiments. In the early studies of AN modelling, AN spiking behaviour is described as a renewal process. According to this approach, the spiking behaviour is only dependent on the timing of the last spike, earlier spikes does not have any effect on this process. This kind of spiking behaviour can be modelled as a Poisson process with added recovery effects (absolute and relative refractory periods). According to the Poisson model, the ISI's are distributed exponentially and a refractory period can be included by adding an offset to the exponential distribution. If we want to attribute this behaviour to a synaptic

mechanism between an IHC and the AN, it can be characterized by a large number of synaptic vesicles with a small probability of release. To make the model's behaviour resemble to the actual processing more closely in this specialized synapse, recovery effects must be included. The recovery effects include the absolute refractory period, where an ANF will not generate any spike events, and the relative refractory period, where an ANF will have a reduced probability discharging..

In 1993, Laurel H. Carney came up with a phenomenological model for the auditory periphery (Fig. 2.1). This model was an extention of their earlier 1988 model. The main aim of this model was to produce realistic mean discharge rates and temporal properties in response to different sound pressure level (SPL) of sound stimuli.

The Carney model consists of various stages that implement the different levels of the auditory periphery. The basis of this model was to implement the compressive nonlinearity of the basilar membrane as a narrow band filter. Fluctuations in the input sound level creates a damping effect on the gain of this filter. As the level of input increases, the bandwith of the filter also increases. This damping effect was implemented using a saturating feedback mechanism. This allows the model to make a connection between the change in the mean rate temporal response patterns of AN and the SPL of input stimuli. The output of the filter is delayed to simulate the travelling wave delay that occurs along the length of the basilar membrane.

After the initial cochlear filtering stage, the remaining feedforward path implements the IHC and IHC-AN synapse. The IHC is modelled by a saturating nonlinearity (hyperbolic tangent) that characterizes the IHC input/output functions and two lowpass IIR filters. The adaptation stage regulates the discharge rate of the fiber. The synapse is implemented as a time varying three stage diffusion model. The last

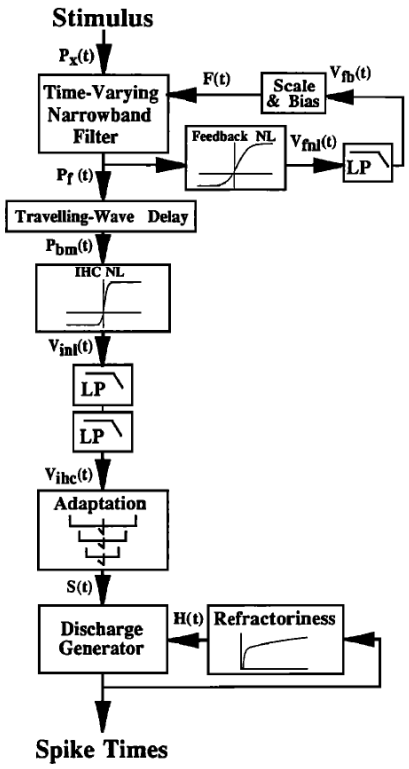

Figure 2.1: Carney (1993) model of auditory periphery. Reprinted with permission of Acoustic Society of America, from Carney (1993) ©1993.

stage takes the output of the IHC-AN synapse and generates a spike train using a Poisson discharge generator. The absolute refractory period is constant and the relative refractory period is implemented as a discharge - history effect that incorporates time dependency using the sum of two exponentials. Outputs produced by this model at different stages are shown in Fig. 2.2.

The model was able to capture the temporal processing and average firing rate of ANFs using simple tone bursts with frequencies different than the CF of fiber and to complex stimuli like wideband noise. The two-tone suppression phenomenon can be defined as one tone's reducing the basilar membrane response to the other tone when presented together. The model was not able to simulate two-tone suppresion effects. So rate and temporal responses to stimuli that has energy dominated by frequencies other than CF cannot be produced correctly by this model. Also the simulations made with this model were limited with low CF, high SR ANFs.

To capture the accurate neural representation of complex stimuli like speech signals, nonlinear interactions between frequency components are important. Zhang *et al.* (2001) is an extention of Carney (1993) that focuses on implementing nonlinear cochlear gain and bandwidth changes that occur with sound level, level dependant phase property and two-tone suppression. All of these properties are attributed to the active cochlear amplifier. The Zhang *et al.* (2001) model aims to capture these properties with a single mechanism.

For stimuli that consist of different frequency components, two-tone suppression effects the response in a drastic way. To implement this property in the model, the feedback control mechanism in the Carney (1993) is replaced with a wideband feed-forward control path. This allows the model to be able to capture the two-tone

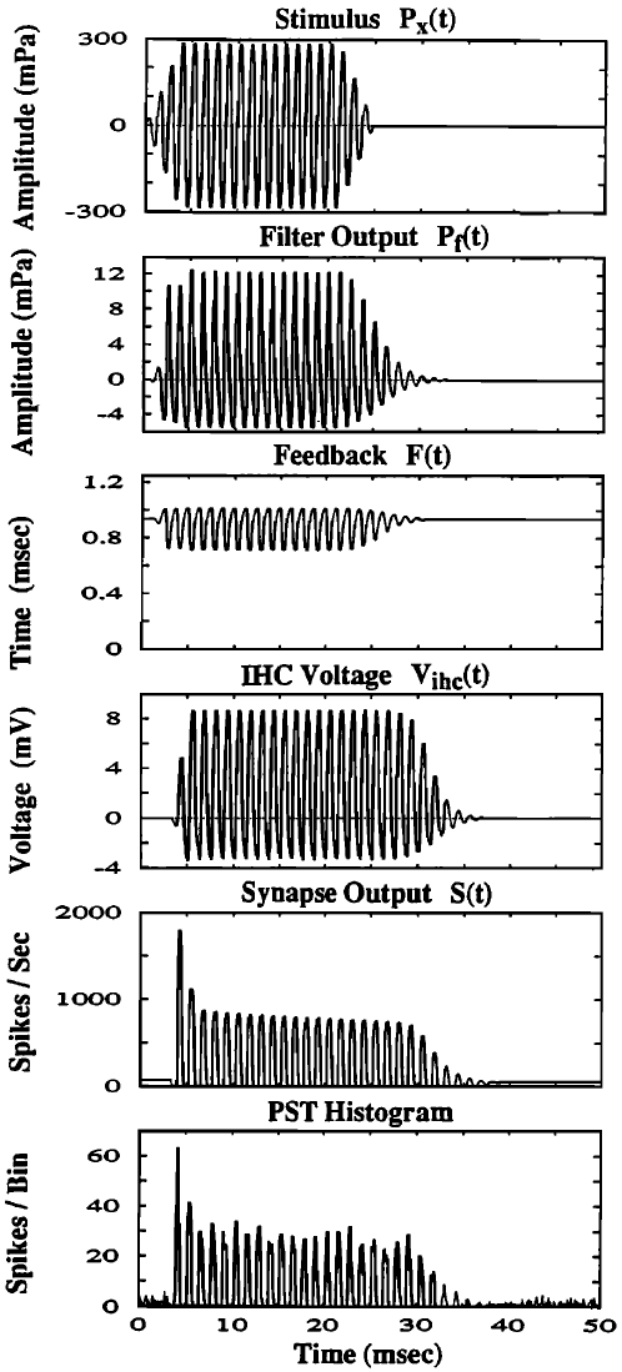

Figure 2.2: Outputs of different stages of Carney (1993). An ANF model with 800 Hz CF is subjected to 25 ms long, 800 Hz input stimulus with a 2.5 ms rise and fall time. Reprinted with permission of Acoustic Society of America, from Carney (1993) ©1993.

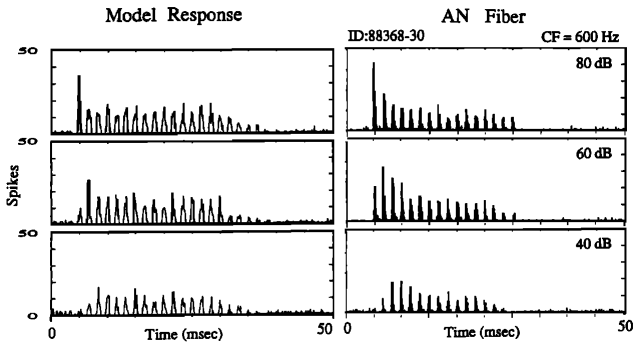

Figure 2.3: Comparison of PSTH's between recordings and model outputs for different SPL's. Real ANF recordings were done by a previous study of Carney. Reprinted with permission of Acoustic Society of America, from Carney (1993) ©1993.

suppression by adjusting the suppression tuning to be broader than the excitatory tuning. The model is shown in Fig. 2.4.

There are two main paths in the model: a signal path and a control path. The signal path consists of a cascaded time-varying narrowband filter and a linear filter. Time-varying narrowband filter is a third-order gammaband filter. The linear filter is a first-order gammatone filter. The linear filter is introduced to eliminate the dc component resulting from the asymetriccal response of the narrowband filter. The gain and bandwidth of narrowband filter is changed according to the control signal.

The control path consists of a time-varying wideband filter that is implemented as third-order gammatone filter, a symmetrical nonlinear function followed by an asymmetrical nonlinear function to characterize the compression dynamics of the cochlear amplifier. A final nonlinear stage controls the level of compression. The wideband filter has more bandwidth then the filter in the signal path.

The IHC model is implemented as a logarithmic compressive function followed by a low pass filter to represent the low pass filtering effect of the IHC. The synapse model

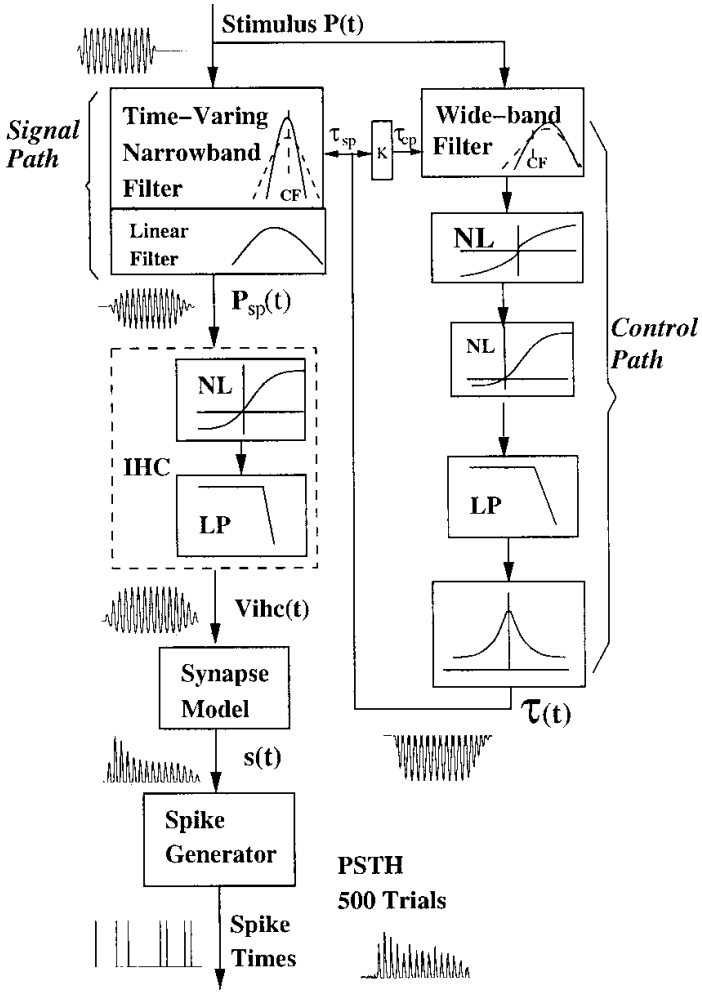

Figure 2.4: Zhang *et al.* (2001) auditory periphery model.Reprinted with permission of Acoustic Society of America, from Zhang *et al.* (2001) ©2001.

used in this study was a simplified version of the synapse model used in Carney (1993) model. The output of the model is a Poisson process modified to include refractory effects. The results taken from different stages of the model is presented in Fig. 2.5.

The compression effect gets more prominent as the CF of the fiber increases. This can be seen from the output of the signal path $P_{sp}(t)$. This model also produces the adaptation property since the model can fire more on the onset of the signal and firing settles down to a steady level in exponential manner.

Since this model is phenomenological, the parameters are fitted in a way to capture the processes that happen in the AN fibers instead of the actual physiological mechanism of the fibers. This model, again, included only high spontaneous rate fibers. Also some properties of AN fiber responses and BM mechanisms such as tails of tuning curves and simple-tone interference which can be explained by other approaches are not addressed in this study. Both the Carney (1993) and Zhang *et al.* (2001) models do not include middle ear or outer ear effects on the stimuli.

In the Bruce *et al.* (2003) model, a middle ear filter is added to Zhang *et al.* (2001) model and modifications are made to implement OHC and IHC impairment (Fig. 2.6). The symmetric nonlinearity after the wideband filter of the control path is removed and its effect is compensated for with a linear scaling of 410^3. The OHC linear filter cutoff frequency is decreased from 800 Hz to 600 Hz. To implement the OHC impairment, a scaling factor C_{OHC} is added at the end of the control path. The value of C_{OHC} is between 0 and 1, lower values indicate more impairment. The OHC impairment effects can be seen in Fig. 2.7. The model also predicts the IHC impairment by introducing a scaling factor, C_{IHC} after the narrowband filter section on the signal path. By doing this the IHC impairment effect on elevated threshold

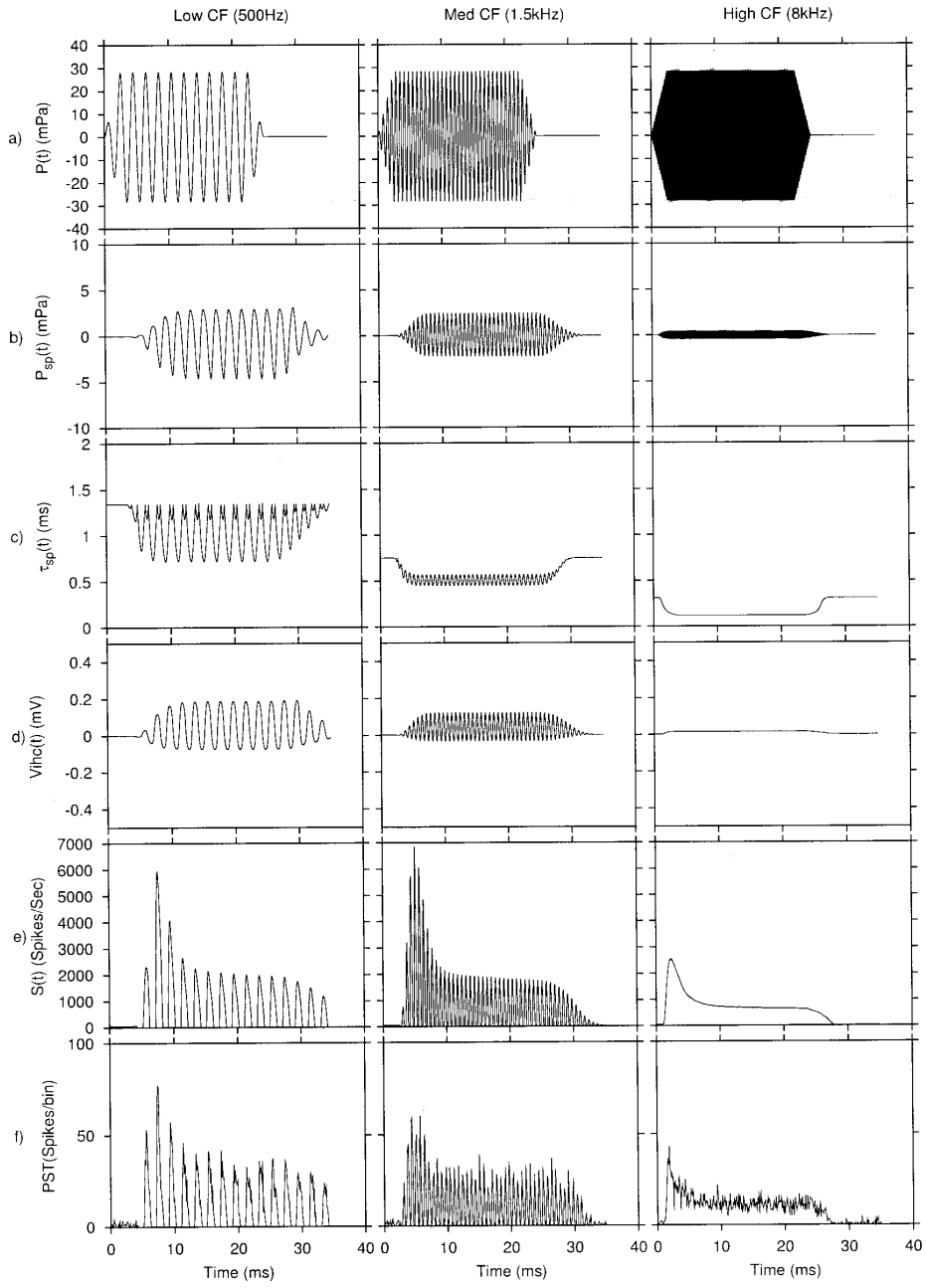

Figure 2.5: Results of three different CF fibers of Zhang *et al.* (2001) model taken from different stages of model. The stimulus is 60 dB tone burst presented for 25 ms with a fall and rise time of 2.5 ms. Reprinted with permission of Acoustic Society of America, from Zhang *et al.* (2001) ©2001.

curves can be achieved while keeping the saturation potential at the same value to retain maximum discharge rate.

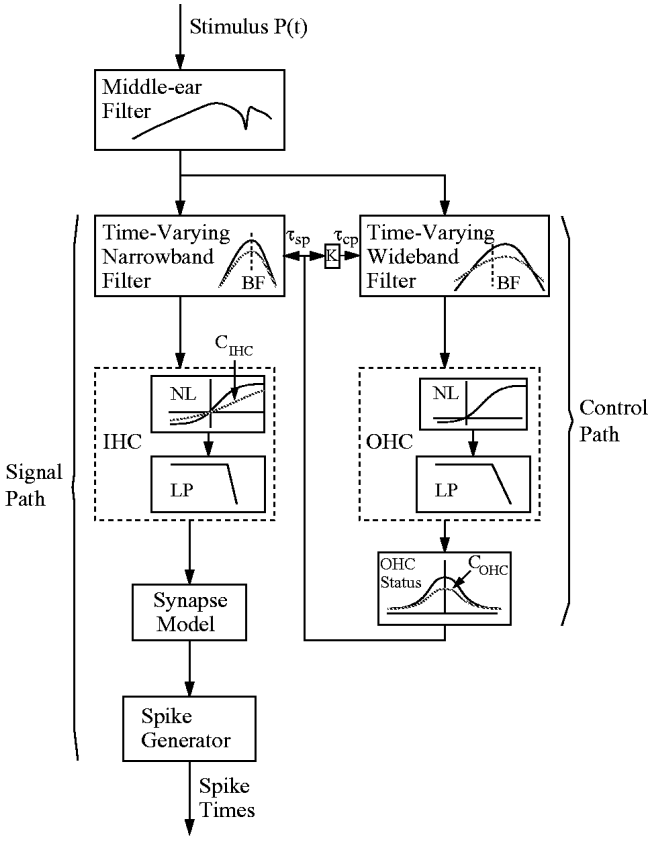

Figure 2.6: Bruce *et al.* (2003) auditory periphery model. Reprinted with permission of Acoustic Society of America, from Bruce *et al.* (2003) ©2003.

In Zilany and Bruce (2006) model, the signal path is divided into two main pathways (Fig. 2.8) to capture the nonmonotonic behaviour of AN fibers such as component 1 - component 2 (C1/C2) transition, peak splitting and BF shift. When AN fibers are subjected to high level stimuli there is a sharp transition in the phase-level function. C1 is defined as the low level response that occurs before the phase shift and C2 is the high level response occuring after the phase shift. According to the

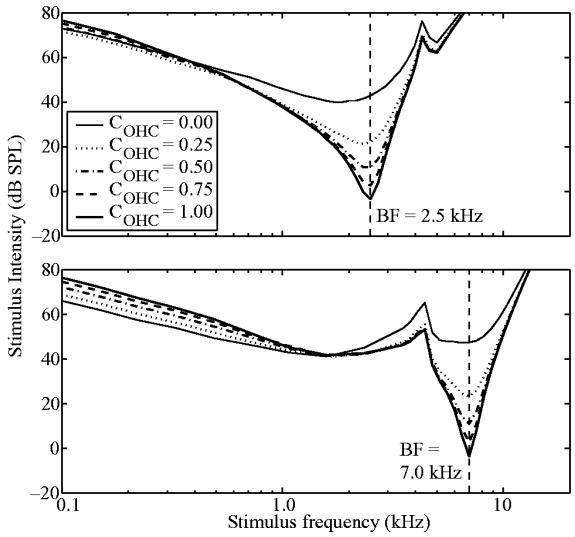

Figure 2.7: OHC impairment effects on AN tuning curve. As the impairment gets worse, the tuning curve gets more broader and the threshold gets higher. Also there is a slight shift in the best frequency (BF) of the AN fiber. Reprinted with permission of Acoustic Society of America, from Bruce *et al.* (2003) ©2003.

C1/C2 transition hypothesis, the C1 component is narrowly tuned and dominates the low level response while the C2 component is broadly tuned and is more prominent at a high level response. The C2 component has a 180 phase difference with respect to C1, so when both of them are the same amplitude, they cancel each other. This creates the C1/C2 transition phenomenon. In the model this is implemented as a narrowband chirp filter (C1) and a broadly tuned linear filter (C2) instead of using one narrowband filter after middle ear stage as in Bruce *et al.* (2003). The C1 filter is characterizes low and medium level stimuli responses. The bandwith and the gain of the C1 filter is regulated by the control band. The C2 filter, followed by an inverting nonlinearity, characterizes high level stimuli responses. The control path and the remaining stages in the model are almost the same with some minor changes on the parameters.

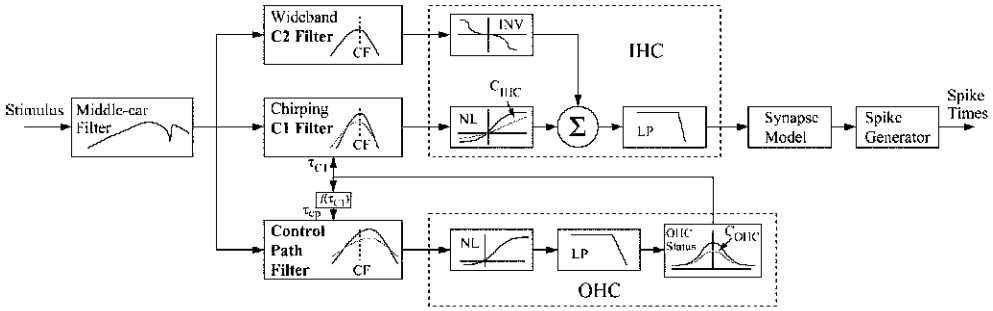

Figure 2.8: Zilany and Bruce (2006) auditory periphery model. Reprinted with permission of Acoustic Society of America, from Zilany and Bruce (2006) ©2006.

Zilany *et al.* (2009) introduces the power law and exponential adaptation (Fig. 2.9). In biological systems, even though the short term behaviour can be exponential, the long term behaviour can be better explained by power law dynamics. When ANFs are subjected to a constant stimulus, adaptation occurs in the firing rate that is understood to be caused by the IHC-AN synapse mechanism. This adaptation behaviour is dependent on many parameters such as stimulus intensity and duration, firing history, spontaneous rate of the fiber etc. Several attempts have been made to model this adaptation behaviour, but these studies used the same exponential adaptation in both the onset and offset responses. However, physiological data shows there is a considerable difference between the onset and offset behaviour. For instance, the offset firing rate might drop below the spontaneous firing rate and slowly recover to the spontaneous rate.

Zilany *et al.* (2009) implements the onset and offset behaviours by adding a new stage to the model. The rest of the model kept the same with a small change in the cut-off frequency of the IHC filter from 3.8 kHz to 3 kHz. The IHC response is feed to an exponential adaptation component with a rapid and short-term time constant. This component is responsible for shaping the onset response of the system. The

exponential adaptation component is followed by a slow and fast power law adaptation element. Slow power law adaptation (PLA) is responsible for the improvement of the offset response and recovery after the stimulus offset. The fast PLA contributes to an unsaturated onset response and an additivity property seen in AN fibers behaviour. The additivity behaviour of ANF responses can be explained as the change in the firing rate in response to the change in the sound level of the sound, but does not depend on the onset timing or subsequent change in the sound level. The adaptation effects on the onset and offset of the response can be seen in Fig. 2.10.

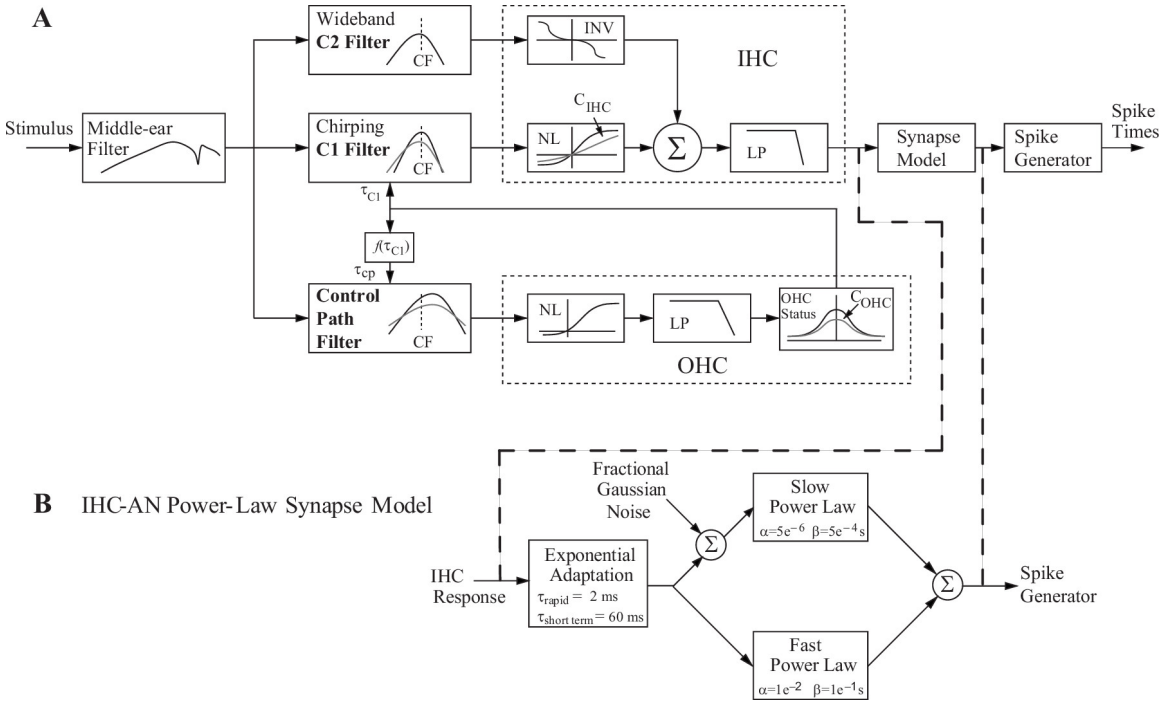

Figure 2.9: Zilany *et al.* (2009) auditory periphery model. Reprinted with permission of Acoustic Society of America, from Zilany *et al.* (2009) ©2009.

The model also introduces Fractional Gaussian Noise (fGn), which is a modified version of white gaussian noise, to implement different SR classes. The fluctuating

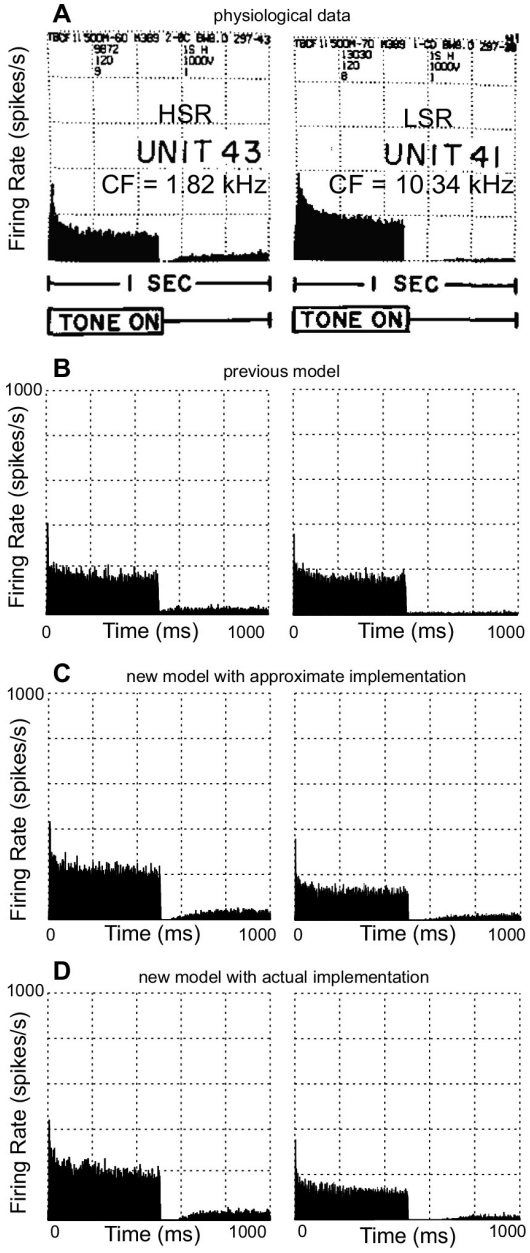

Figure 2.10: The Zilany *et al.* (2009) implementation of adaptation effects on the output PSTH. There is a sharp drop at the end of the stimulus in previous model. But the drop is down to spontaneous firing rate level which is not realistic as it can be seen from the physiological data presented in panel (A). The new model exhibit the notch at the end of the stimulus and the slow recovery to the spontaneous rate firing. Reprinted with permission of Acoustic Society of America, from Zilany *et al.* (2009) ©2009.

fGn, placed before the slow PLA stage, prevent the SR rate from continuously adapting to zero. The fGn stage was placed before the slow PLA component since the slow PLA stage does not change the dynamics of fGn significantly. If the fGn were placed after the PLA components, the noise would have fill the notch after the offset response so the recovery effect would be lost.

Three different parameter sets are used to implement three classes of SR: low (0.1 spikes/sec), medium (5 spikes/sec) and high (100 spikes/sec). This distribution of SRs is in accordance with to physiological data from Liberman (1978) (Fig. 2.11).

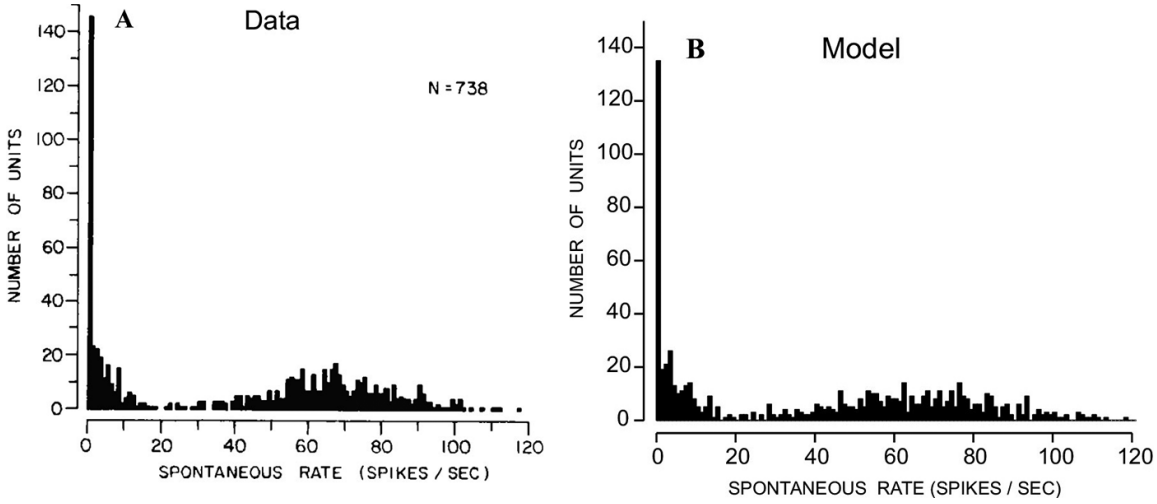

Figure 2.11: Histogram of SR distribution comparison between Liberman (1978) and Zilany *et al.* (2009). The fGn is arranged such that the SR distribution fits the data from Liberman (1978). Reprinted with permission of Acoustic Society of America, from Zilany *et al.* (2009) ©2009.

Studies show that the firing of ANFs is actually dependant on the history of firing and the probability of the firing fluctuates over time. This aspect was added to the model by implementing the fGn in the presynaptic adaptation section. The spike generation was still modeled as a renewal process in Zilany *et al.* (2009) as a Poisson spike generator.

AN fiber excitation is achieved via a special kind of synapse between IHC and AN. This synapse is able to fire at high rates and preserves temporal precision. In Bruce *et al.* (2018) model, a new IHC - AN synapse model is introduced (Fig. 2.12). The implementation of this synapse model into phenomenological AN model and changes made in the previous synapse model used in Zilany *et al.* (2009) are shown in Fig. 2.12.

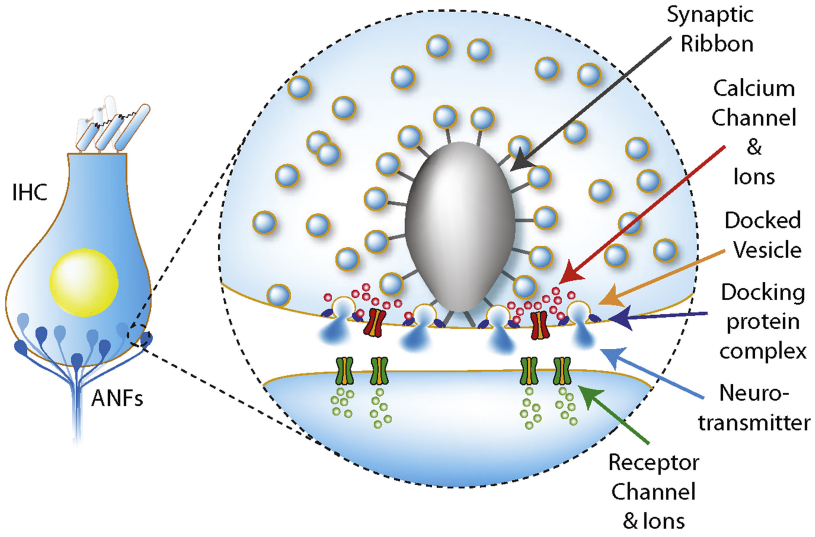

Figure 2.12: Illustration of Bruce *et al.* (2018) synapse model between ANF and IHC. Reprinted from Bruce *et al.* (2018) ©2018, with permission of Elsevier.

According to Peterson *et al.* (2014) the spontaneous firing of the AN model can be explained by 4 vesicle docking sites with redocking times (a new vesicle reaching to an empty docking site) of 13.5 - 17 ms. Even though this approach can implement the rapid exponential adaptation, it fails to implement the short term adaptation component. The longer component of the double exponential refractory recovery is suggested to be caused by a small number of vesicles with small release probability (Peterson *et al.*, 2014) and is modelled according to this. Later, they updated their deterministic model with a probabilistic model. But this study was only focusing on

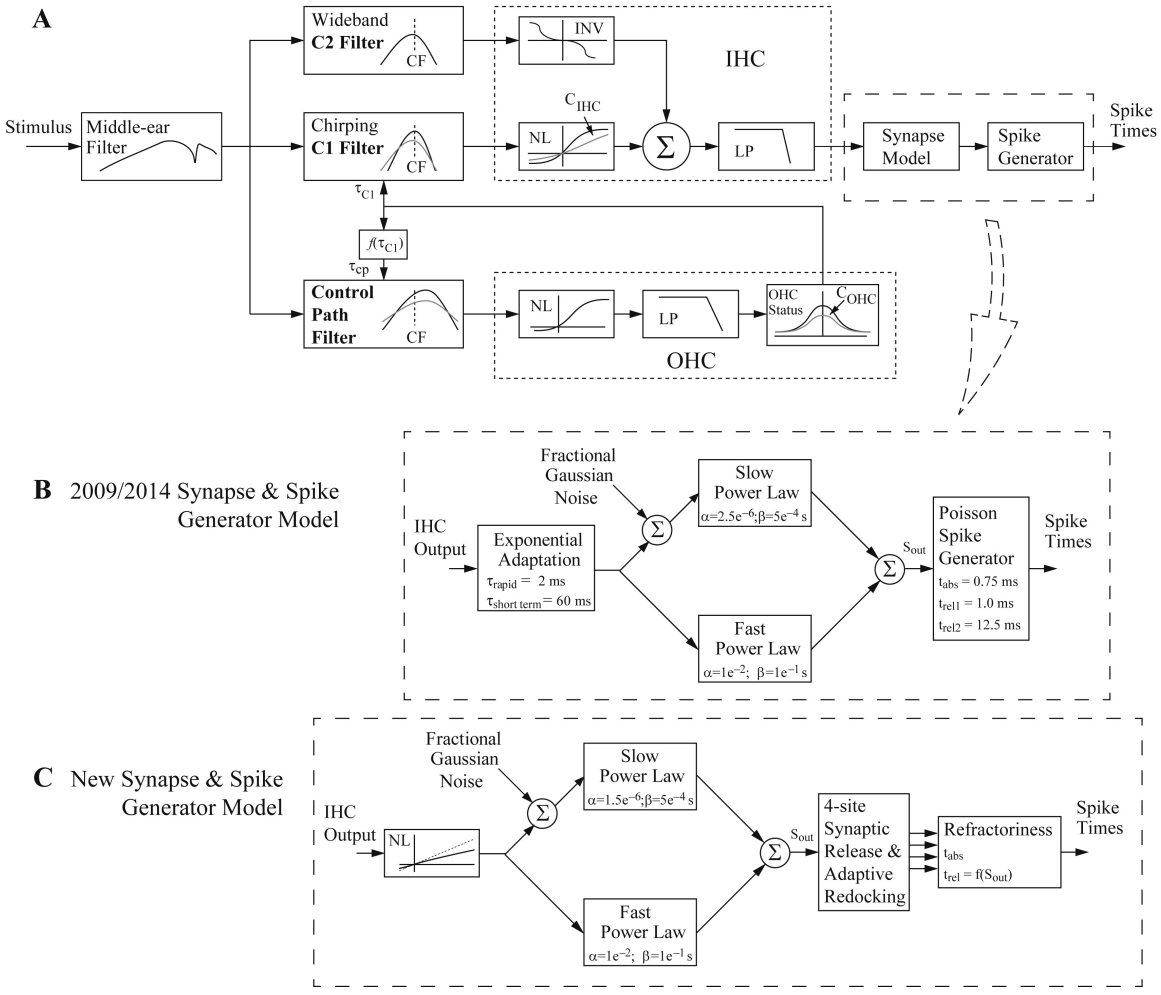

Figure 2.13: Bruce *et al.* (2018) auditory periphery model. Panel B and C compares the old model with the new one. The new model has updated synapse and spike generator. Abbreviations: outer hair cell (OHC), inner hair cell (IHC), low-pass (LP) filter, static nonlinearity (NL), characteristic frequency (CF), and inverting nonlinearity (INV). Reprinted from Bruce *et al.* (2018) ©2018, with permission of Elsevier.

the spontaneous rate of ANFs. Bruce *et al.* (2018) expanded this model to be able to produce sound driven AN fiber responses.

In the new model the spontaneous rate of AN fibers are sampled from a Gaussian distribution with mean, standart deviation and limits given in Table 2.1. Reducing the standard deviation of fGn and having a distribution of SR parameters provides a whole range of SR rates. In the previous model, even though 3 distinct SR classes were implemented, they were clustered into three groups (Fig. 2.14).

Table 2.1: SR distribution of different classes

SR class	Mean	Standart Deviation	Limits
low	0.1	0.1	$[10^{-3}, 0.2]$
medium	4	4	$[0.2, 18]$
high	70	30	$[18, 180]$

Even though the main focus of the thesis is VCN, the AN modelling part is also important in terms of forming one of the basis of the neural encoding of sound signals. Therefore the Bruce *et al.* (2018) model of ANFs used in this study is a powerful step to create a detailed model for VCN microcircuits.

2.2 Rothman and Manis Cell Models of Ventral Cochlear Nucleus

Rothman and Manis (2003c) created HH type neuron models for ventral cochlear nucleus neurons by investigating the potassium (K^+) channels. These currents regulate the cells behaviour to extract different features from the AN input such as phase of the stimulus, fine temporal information, envelope modulation and stimulus

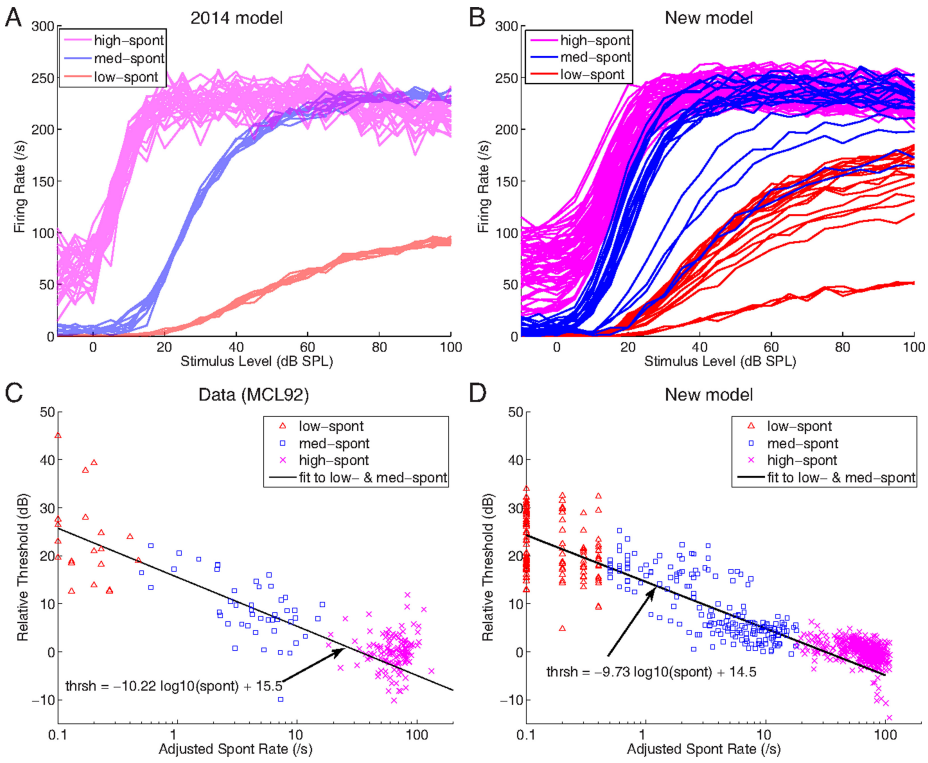

Figure 2.14: Bruce *et al.* (2018) distribution of SR rates effect on rate level curves. It can be seen from (A) and (B) that the new model has more ability to implement a range of SR rates. When compared with physiological data, the model shows a similar trend to real world data (Liberman, 1978). Reprinted from Bruce *et al.* (2018) ©2018, with permission of Elsevier.

intensity. Cells in VCN are able to do this because they have specialised mechanisms like rapid synaptic receptor kinetics, dentritic filtering, coincidence detection and specialized membrane currents. According to whole cell recordings taken from the individually isolated VCN neurons, three main distinct K^+ channels were identified: a high-threshold-delayed-rectifier-like current I_{HT}, a fast inactivating current I_A and a slow-inactivating low-threshold current I_{LT}. These channels regulate the spike timing, the shape of the spikes, regularity and the adaptation properties. Depending on how active the different channels are, individually or together, VCN cells show different discharge behaviour. In Rothman and Manis (2003a) cells are classified as Type I-c, Type I-i, Type I-t and Type II. Type I-c and Type II cells are the two main response types. Type I-t (transient) is a Type I-c (classic) cell with an I_A current. Type I-i (intermediate) shows an intermediate character between Type I and Type II. The typical responses of these distinctive cells are shown in Fig. 2.15.

K^+ currents in Type I-c cells only consist of I_{HT} currents. The arrow in Fig. 2.15 B1 indicates that Type I-t cell responses also involves I_A. Isolated recordings show that I_A activates 15 mV below I_{HT} and shows fast inactivation compared with other current types. The arrowhead in Fig. 2.15 B1 indicates that Type I-t cells have hyperpolarization-activated inward current (I_h). Fig. 2.15 C1 shows a typical Type II current clamp response. Unlike Type I-c cells, these cells have a strong presence of I_{LT} besides I_{HT}. The effects of I_{LT} on the voltage clamp recordings are indicated by arrowheads. Fig. 2.15 D1 shows a typical Type I-i cell response, which is close to Type II cell response, but I_{LT} current effects are not as prominent as in Type II cell.

Each channel has a different type of effect on the firing behaviour and this contributes to create different characteristics in cells. By blocking the other channels

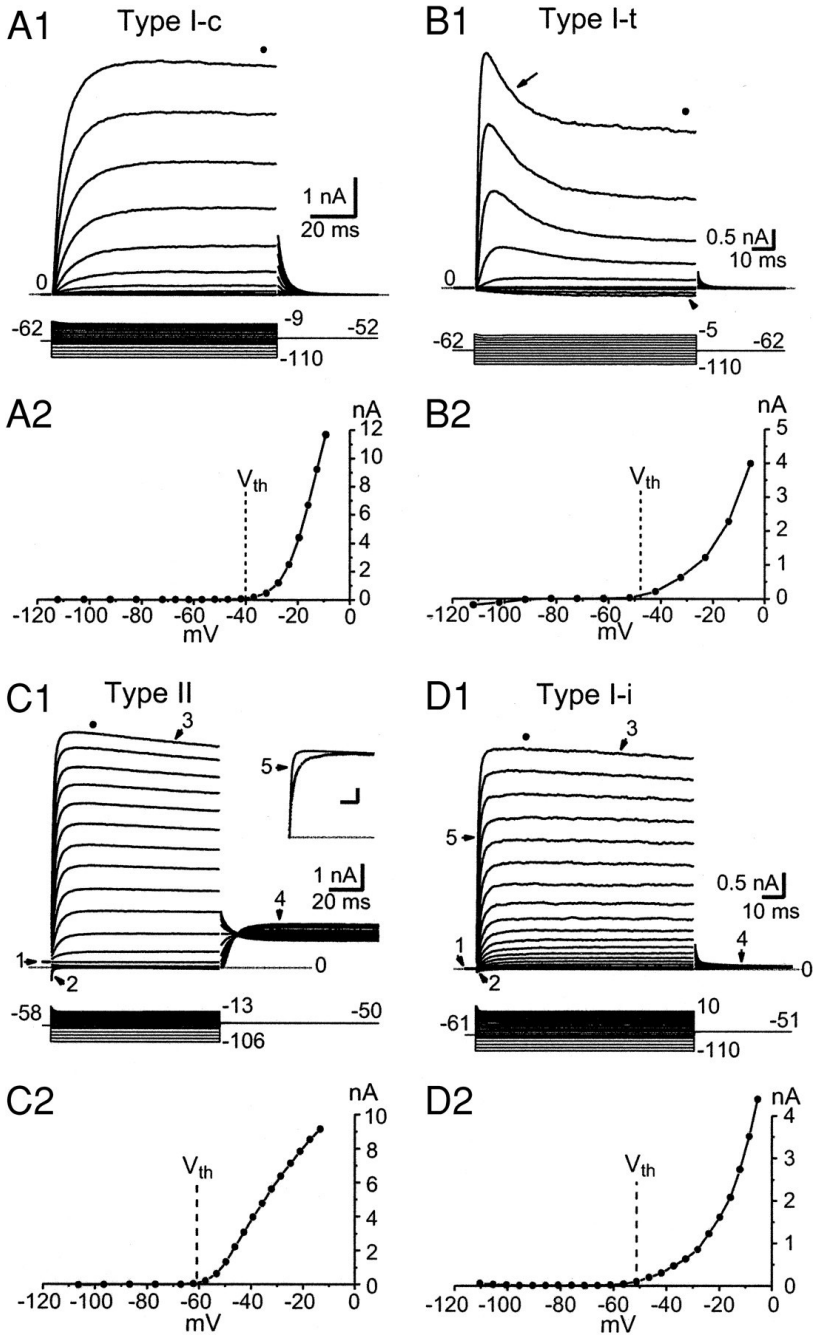

Figure 2.15: Four main types of voltage clamp responses observed in VCN neurons. A1 - B1 - C1 and D1 shows whole cell recordings. Bottom figures shows the I-V characteristics of cells. Reprinted with permission of The American Physiological Society, from Rothman and Manis (2003a) ©2003.

with receptor antagonists, Rothman and Manis (2003a) isolated individual channels to inspect their effect on firing behaviour. According to the physiological data, I_{LT} is responsible for the hyper-conductance state after the initial firing in bushy cells when it is excited with an external steady current injection. I_{LT} contributes to the cell's ability to phase lock and act as a coincidence detector. I_{HT} is detected in bushy and stellate cells of the VCN. This channel allows cells to fire at a high rate since it improves the rapid repolarization of the membrane.

In Rothman and Manis (2003b), kinetic analyses of these currents are made and a set of differential equations are created to model the behaviours of the individual channels. According to this study, the behaviour of I_{A} can be defined with fourth order activation kinetics (a^4), and inactivates with two time constants to implement its recovery from inactivation (a^4bc). I_{LT} also has a fourth order activation (w^4) but shows a slower inactivation. I_{HT} has two individual activation particles ($n^2 + p$), and activation of these particles lead to two distinct currents.

Rothman and Manis (2003c) inspects how three K^+ currents affect the firing behaviour of the cells by using the differential expressions obtained from their previous study to build a single compartment HH type model. This model also includes a fast inactivating Na^+ current ($I_{\mathrm{Na^+}}$), a hyperpolarization activated cation current (I_{h}), a leakage current (I_{leak}), a synaptic current channel to include dentritic inputs coming from other cells (I_{e}), and I_{ext} to simulate the injected current mechanism. The change in the membrane voltage is calculated as:

$$C_m \frac{dV}{dt} = -(I_{\mathrm{HT}} + I_{\mathrm{LT}} + I_{\mathrm{A}} + I_{\mathrm{h}} + I_{\mathrm{lk}} + I_{\mathrm{e}} - I_{\mathrm{ext}}) \tag{2.1}$$

where C_m is the membrane capacitance.

The differential expressions govern the behaviour of the fast inactivating I_A current are given as:

$$I_A = \overline{g}_A a^4 bc(V - V_k) \tag{2.2}$$

where g_{A} is the maximum conductance and V_{k} is the reversal potential of K^+ ions. The activating and inactivating particles are changing according to:

$$a_\infty = [1 + \exp(-(V + 31)/6)]^{-1/4} \tag{2.3}$$

$$b_\infty = [1 + \exp((V + 66)/7)]^{-1/2} \tag{2.4}$$

$$c_\infty = b_\infty \tag{2.5}$$

And the time constants for these particles are calculated as:

$$\tau_a = 100[7\exp((V + 60)/14) + 29\exp(-(V + 60)/24)]^{-1} + 0.1 \tag{2.6}$$

$$\tau_b = 1000[14\exp((V + 60)/27) + 29\exp(-(V + 60)/24)]^{-1} + 1 \tag{2.7}$$

$$\tau_c = 90[1 + \exp(-(V + 66)/17)]^{-1} + 10 \tag{2.8}$$

From the simulations, it is found that I_{A} is responsible for the regulation of rate of repetitive firing in Type-I cells.

The low-threshold K^+ current I_{LT} can be modelled as:

$$I_{LT} = \overline{g}_{LT} w^4 z (V - V_k) \tag{2.9}$$

While the activation and inactivation particles are modelled such as:

$$w_\infty = [1 + \exp(-(V + 48)/6)]^{-1/4} \tag{2.10}$$

$$z_\infty = (1 - \zeta)[1 + \exp((V + 71)/10)]^{-1} + \zeta \quad (\zeta = 0.5) \tag{2.11}$$

The time constants for these particles are calculated as:

$$\tau_w = 100[6\exp((V + 60)/6) + 16\exp(-(V + 60)/45)]^{-1} + 1.5 \tag{2.12}$$

$$\tau_z = 1000[\exp((V + 60)/20) + \exp(-(V + 60)/8)]^{-1} + 50 \tag{2.13}$$

From simulations I_{LT} is found to be responsible for the phasic response of Type-II cells, which is in agreement with the physiological recordings.

I_{HT} is mainly responsible for the repolarization of the membrane during the firing.

The I-V relation of high - threshold K^+ current I_{HT} is:

$$I_{HT} = \overline{g}_{HT}[\varphi n^2 + (1-\varphi)p](V - V_k)(\varphi = 0.85) \tag{2.14}$$

The activating and inactivating particle behaviours are represented as:

$$n_\infty = [1 + \exp(-(V+15)/5)]^{-1/2} \tag{2.15}$$

$$p_\infty = [1 + \exp((V+23)/6)]^{-1} \tag{2.16}$$

The time constants for these particles are calculated as:

$$\tau_n = 100[11\exp((V+60)/24) + 21\exp(-(V+60)/23)]^{-1} + 0.7 \tag{2.17}$$

$$\tau_p = 100[4\exp((V+60)/32) + 5\exp(-(V+60)/22)]^{-1} + 5 \tag{2.18}$$

The fast Na^+ current I_{Na} used in this model is obtained from other voltage clamp recordings done in other studies. The I-V relation of this current is:

$$I_{Na} = \overline{g}_{Na} m^3 h (V - V_{Na}) \tag{2.19}$$

The activating and inactivating particle behaviours can be modelled as;

$$m_\infty = [1 + \exp(-(V+38)/7)]^{-1} \tag{2.20}$$

$$h_\infty = [1 + \exp((V + 65)/6)]^{-1} \tag{2.21}$$

And the time constants used in above equations are;

$$\tau_m = 10[5\exp((V + 60)/18) + 36\exp(-(V + 60)/25)]^{-1} + 0.04 \tag{2.22}$$

$$\tau_h = 100[7\exp((V + 60)/11) + 10\exp(-(V + 60)/25)]^{-1} + 0.6 \tag{2.23}$$

Like I_{Na}, the hyperpolarization-activated cation current I_h is modeled based on other studies. The I-V relationship for this current is:

$$I_h = \overline{g}_h r(V - V_h) \tag{2.24}$$

The activating particle r is modelled as:

$$r_\infty = [1 + \exp(-(V + 76)/7)]^{-1} \tag{2.25}$$

The time constant for this particle is calculated as:

$$\tau_r = 10^5[237\exp((V + 60)/12) + 17\exp(-(V + 60)/14)]^{-1} + 25 \tag{2.26}$$

The leakage current used in this model is;

$$I_{lk} = \overline{g}_{lk}(V - V_{lk}) \tag{2.27}$$

Table 2.2 shows parameters that are used to simulate the behaviour of different type of neurons in VCN. Reversal potentials for the channels are; $V_{\mathrm{K}} = -70$ mV , $V_{\mathrm{Na}} = +55$ mV, $V_{\mathrm{h}} = -43$ mV, $V_{\mathrm{lk}} = -65$ mV.

Table 2.2: Model Parameters and Properties

	Model Type				
	I-c	I-t	I-II	II-I	II
$\overline{g}_{\mathrm{Na}}$, nS	1000	1000	1000	1000	1000
$\overline{g}_{\mathrm{HT}}$, nS	150	80	150	150	150
$\overline{g}_{\mathrm{LT}}$, nS	0	0	20	35	200
$\overline{g}_{\mathrm{A}}$, nS	0	65	0	0	0
$\overline{g}_{\mathrm{h}}$, nS	0.5	0.5	2	3.5	20
$\overline{g}_{\mathrm{lk}}$, nS	2	2	2	2	2
V_{rest}, mV	-63.9	-64.2	-64.1	-63.8	-63.6
R_{rest}, MΩ	473	453	312	244	71
τ_m, ms	7.0	4.0	3.7	2.9	0.9
V_{th}, mV	-38.3	-34.9	-51.2	-58.0	-62.2
$S_{-50/-70}$, nS	0.3	0.3	5.0	12.6	49.5
$\overline{g}_{E\theta}$ @ 22°, nS	2.0	2.2	2.8	3.2	8.6
$\overline{g}_{E\theta}$ @ 38° , nS	11	12	15	17	34

The model responses to a steady current injection applied using similar protocols with in vitro studies are shown in Fig. 2.16.

Type I cells respond to a depolarizing current pulse with a regular firing. The I_{A} effect on the firing behaviour of Type I cells can be seen in Fig. 2.16 A and Fig. 2.16 B. The change in the firing rate of Type I cells are a strong indicator of I_{A} presence. Type II cells show a precise timed spike on the onset of the depolarizing input. The membrane voltage stays in a depolarized state after the spike. The anodal break spike seen at the end of the hyperpolarizing input is another characteristic indicator of Type II model response.

Physiological recordings show that I_{LT} is responsible for the Type II responses

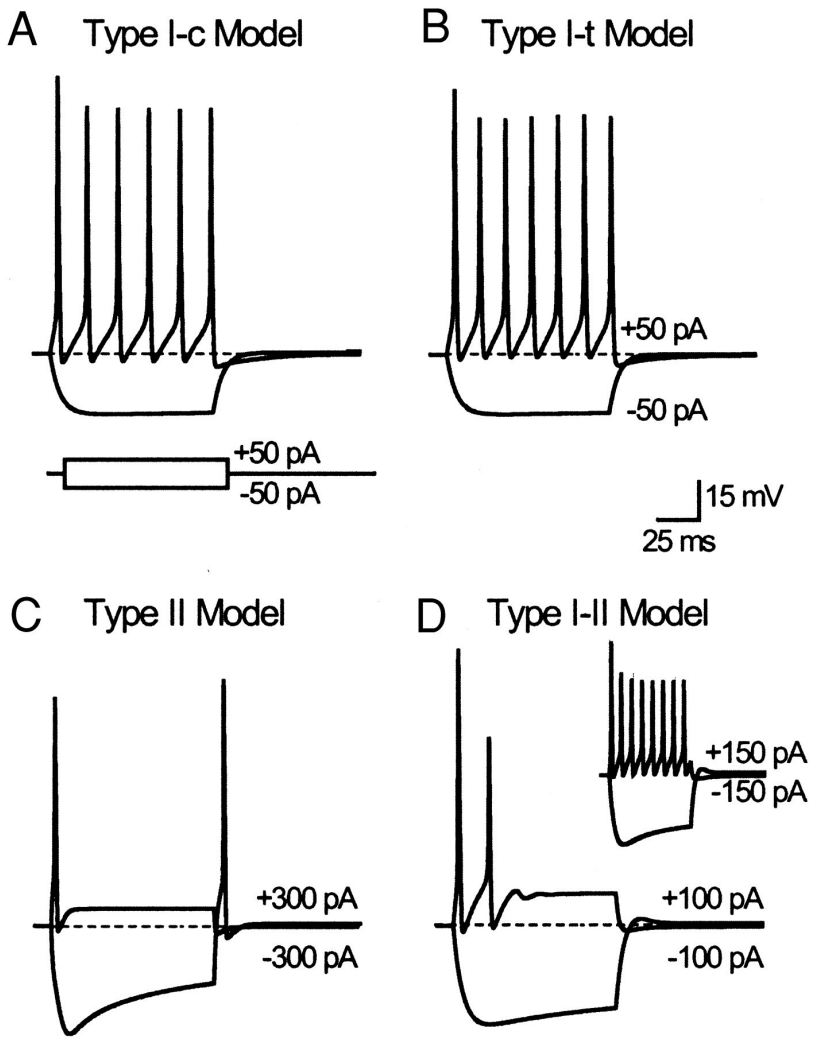

Figure 2.16: Rothman and Manis (2003c) type models of VCN neurons' current clamp responses to positive and negative current injections. Reprinted with permission of The American Physiological Society, from Rothman and Manis (2003c) ©2003.

(Rothman and Manis, 2003b). When I_{LT} is blocked in the model, Type II cells begin to show Type I responses (Fig. 2.17). The effect of I_{LT} is also supported by the results that the absence of other currents does not make a difference in the firing behaviour of the cell to depolarizing current inputs.

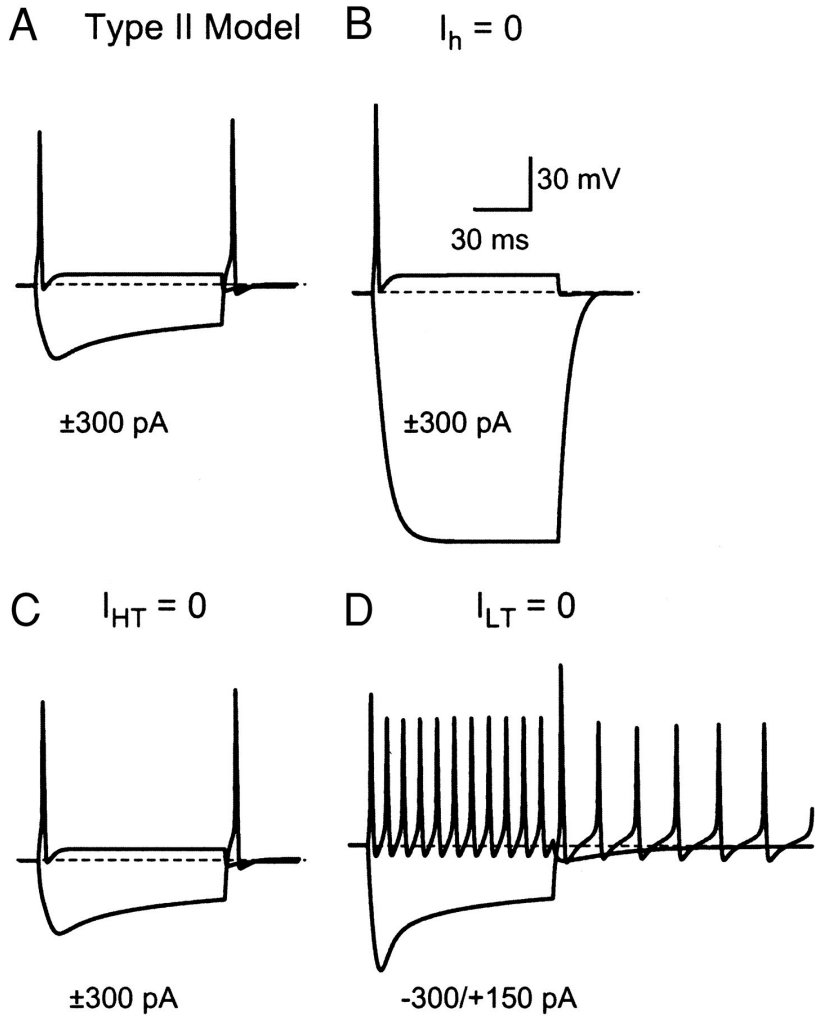

Figure 2.17: Individual current effects on RM'03 Type II cells response. I_{LT} is responsible for the firing behaviour of the Type II cells. Reprinted with permission of The American Physiological Society, from Rothman and Manis (2003c) ©2003.

The membrane resistance (R_{rest}) is the inverse of membrane conductance which

is calculated by summing all of the individual conductances when the membrane is at rest. Type I cells have larger membrane resistances than Type II cells. The membrane time constant τ_m is defined as the product of the membrane capacitance and the membrane resistance. Higher membrane resistance leads to higher τ_m values for Type I cells since the membrane capacitance is the same for all cell types. This is important in terms of defining the cell's behaviour on synaptic input trains. Rothman and Manis (2003c) show effects of τ_m on the behaviour of Type I-c. Since Type I cells have higher τ_m, they act as an integrator, while Type II cells shows a coincidence detector behaviour (Fig. 2.18) when subjected to a subthreshold ($g_E = 0.5\ \overline{g}_E$) input spike train.

Rothman and Manis (2003c) identified Type II cells as bushy cells and Type I cells as stellate cells. Comparing the physiological data presented in the previous chapter, PSTH responses, and regularity analysis of the modelled cells (Fig. 2.19), it can be said that this classification is consistent.

2.3 Bushy Cell Responses to Vowel Stimuli

Blackburn and Sachs (1990) inspected representation of the vowel /ε/ in cat anteroventral cochlear nucleus neurons. They examined bushy and T stellate microcircuit responses by creating rate-place and temporal-place representations. Rate-place representations are created by plotting average discharge rate versus the best frequency (BF) of units. Vowel formants can be seen as peaks in relevant BF locations in these plots. Temporal-place representations quantify the phaselocking of ANFs to vowel components. The frequency spectrum representation of the vowel /ε/ can be seen in Fig. 2.20.

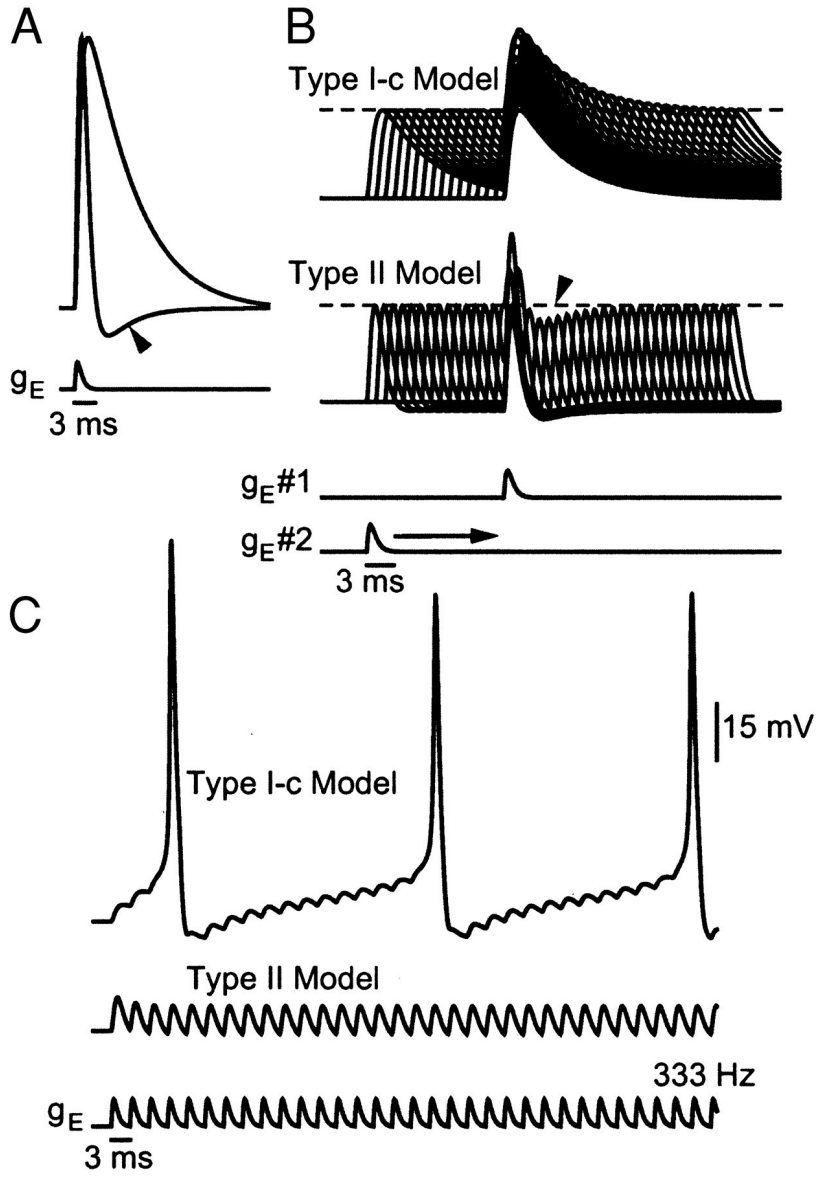

Figure 2.18: RM'03 type cell models response to subthreshold synaptic inputs. (A) shows the individual excitatory-post-synaptic-potential (EPSP) traces of Type I-c and Type II cells to a single spike input. Type II cell's EPSP decays faster and has an afterhyperpolarization (AHP) component after the EPSP which is shown by the arrowhead. (B) Two subthreshold synaptic inputs (one is moving and the other is static) to show the EPSP summation responses of the cells. Type I-c cells show a much longer summation interval than Type II cell. Type II cells show a significant drop after the summation which is useful in terms of enhancing the coincidence detection information. (C) shows the integration behaviour of the Type I-c model. Since the Type II model has a small τ_m it is able to follow the input and preserve the timing information of the spikes. Reprinted with permission of The American Physiological Society, from Rothman and Manis (2003c)[75]©2003.

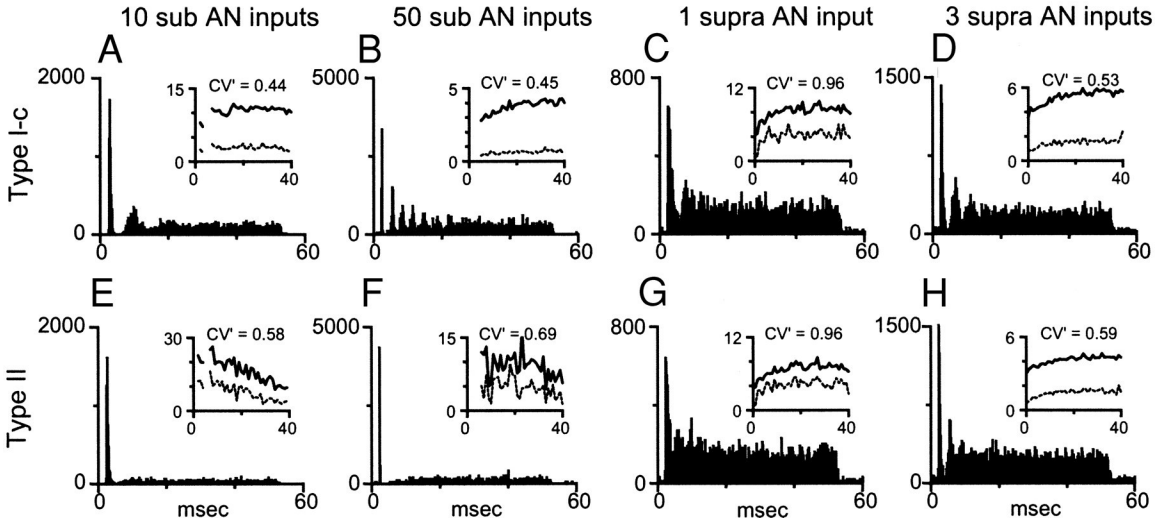

Figure 2.19: PSTH of RM'03 type cell models responses to subthreshold ($g_E = 0.5\ \overline{g}_E$) and suprathreshold ($g_E = 3\ \overline{g}_E$) AN like inputs. Type I cell shows a chopper like response with regular firing. Type II cells show an onset response for subthreshold inputs and primary-like response for suprathreshold inputs. Reprinted with permission of The American Physiological Society, from Rothman and Manis (2003c) ©2003.

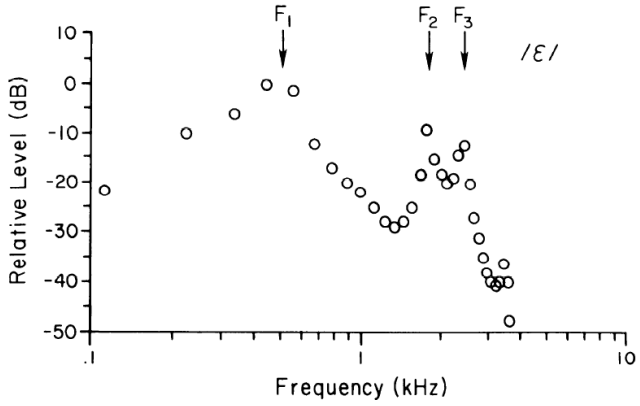

Figure 2.20: Frequency spectrum representation of vowel /ε/. The arrows show the formant frequencies: F1 = 512 Hz, F2 = 1.792 kHz, F3 = 2.432 kHz. Reprinted with permission of The American Physiological Society, from Blackburn and Sachs (1990) ©1990.

Rate saturation causes a big problem for mean-rate representations of high SPL sound stimuli. High SR fibers provide good mean-rate representation of vowel formants in low SPL inputs. However, high SR fibers saturate at lower SPLs than low SR fibers. Therefore, to create an accurate mean-rate representation of a broadband complex stimulus, a selective listening process has been suggested (Delgutte, 1982; Winslow and Sachs, 1987). According to this hypothesis, the rate processor would need to listen to low SR inputs at high levels and high SR inputs at low levels.

Temporal-place representations of vowels are not affected by rate saturation. For this information to be useful in the central auditory system it has to be protected or coded in firing rates of CN neurons. Temporal-place representations are well preserved in the bushy cell populations since they have primary-like responses. They have a strong phase-locking characteristic which helps preserving this type of information.

To reflect the representation of sound signals among the population of cells, average localized synchronized rate (ALSR) is used. ALSR is computed as the average firing rate of units which have their BF within one-quarter octave of the harmonic frequency of stimuli (Blackburn and Sachs, 1990).

Another useful tool to investigate the population of cell responses to stimuli is boxplots. Boxplots show the population distribution of average synchronized rates to stimuli. An example boxplot created from ANF population response to vowel /ε/ can be seen in Fig. 2.22.

2.4 VCN Microcircuit Models

Two recent VCN microcircuit models are taken as a basis for this thesis. Eager (2013) and Manis and Campagnola (2018) used modified neuron models of Rothman and

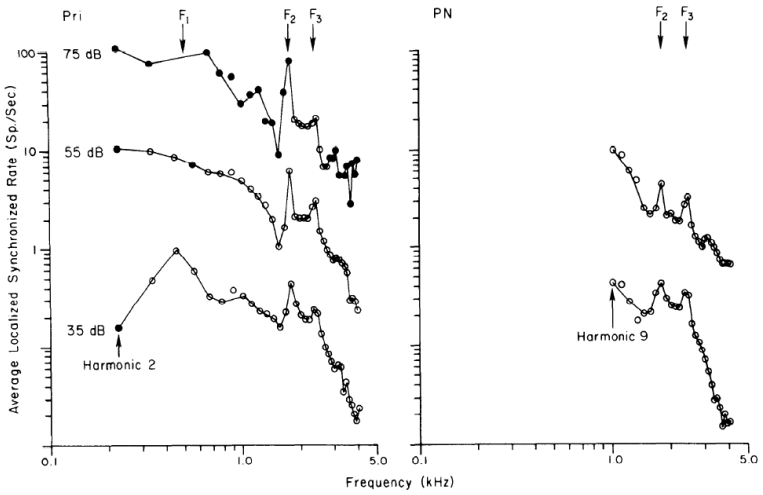

Figure 2.21: Recorded ALSR responses of Pri and PriN units to vowel /ε/. Reprinted with permission of The American Physiological Society, from Blackburn and Sachs (1990) ©1990.

Manis (2003c) to create microcircuits that reside in the VCN. Eager (2013) focused more on creating stellate microcircuits. The parameters used in this model are a mix of physiological parameters obtained from in vitro studies and parameters which are fitted to physiological recordings using optimization techniques. The stellate microcircuit model used in this study is shown in Fig. 2.23.

Eager (2013) used the Zilany *et al.* (2009) model but took out the fGn to obtain a fixed distribution of SR. The validity of the model responses are checked by inspecting PSTHs, rate level curves and response maps. In his study, genetic algorithms were used to fit the parameters by creating a cost function comparing the model responses of cells to tones, noise and click stimuli to physiological data.

Manis and Campagnola (2018) used modified Rothman and Manis (2003c) cell models according to their recent works (Xie and Manis, 2013, 2017; Campagnola and Manis, 2014). The auditory periphery model used in this system is Zilany *et al.* (2009,

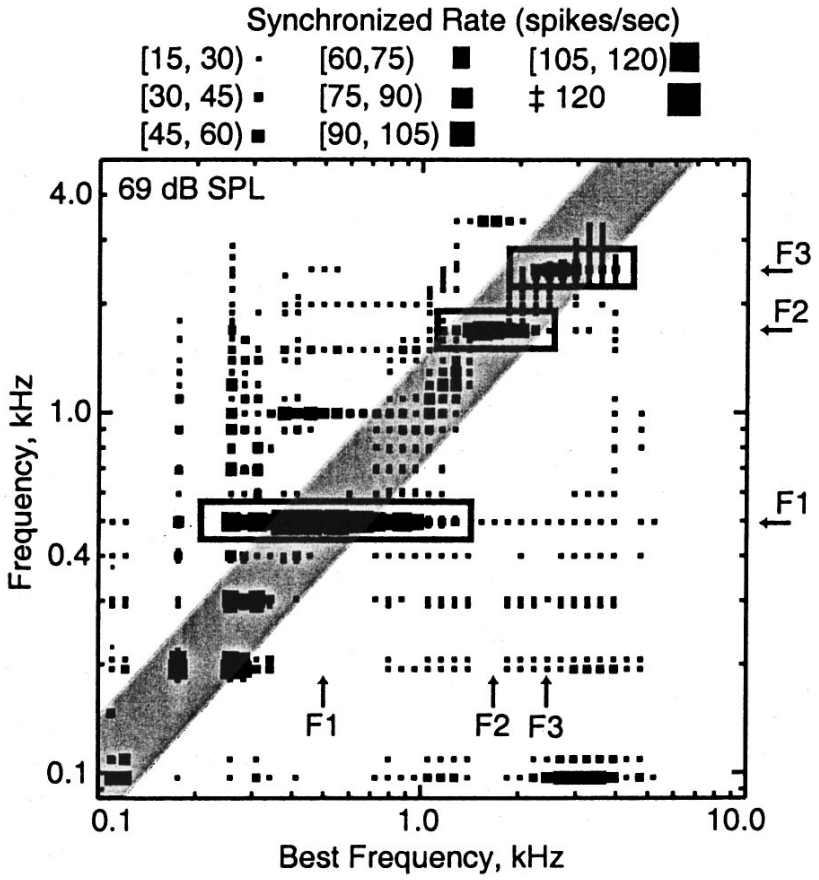

Figure 2.22: Boxplot of ANF population response to vowel /ε/. horizontal axis represents the CF of ANFs. The size of each box shows how strong the response of ANFs within a bin of 0.133 octave to corresponding stimulus component frequency. Formant frequencies of stimuli are indicated by horizontal arrows at the right side of the figure. BF responses to the formant frequencies are indicated by vertical arrows at the bottom of the figure. Reprinted with permission of Springer Nature, from Sachs *et al.* (2002) ©2002.

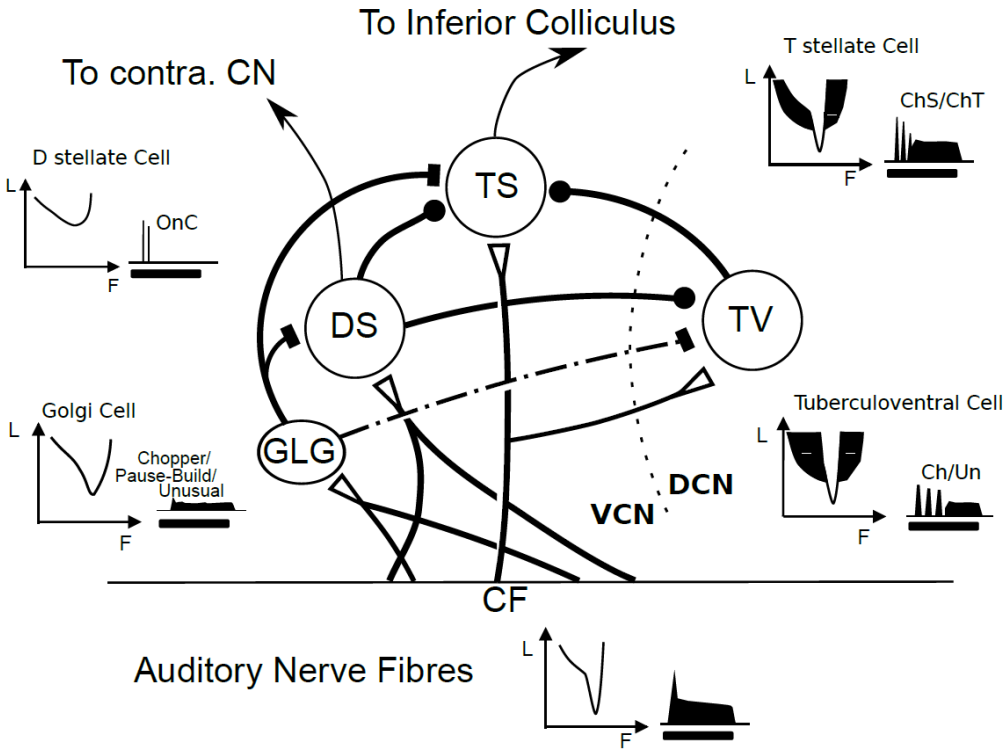

Figure 2.23: Eager (2013) model of stellate microcircuit in VCN. Unfilled triangles indicate excitation, filled rectangle and circles indicate inhibition. From Eager (2013).

2014). The network structure suggested by Manis and Campagnola (2018) can be seen in Fig. 2.24.

Individual cell models are tested with current injections (Fig. 2.25) and a bushy cell microcircuit (Fig. 2.26) is tested to see if the model responses are in agreement with recorded data. Fig. 2.26 shows that DS cells provide broadly tuned and TV cells provide sharply tuned inhibitory input to bushy cells. The third column shows that bushy cells produce a strong AP to the onset of the stimulus. TV cells respond to the tone burst with regular firing patterns. These results are consistent with physiological data. The parameters used in Manis and Campagnola (2018) to create individual cell models are based on Xie and Manis (2013) and given in Table 2.3. Reversal potentials for channels are: $V_{\mathrm{K}} = -84$ mV, $V_{\mathrm{Na}} = +50$ mV, $V_{\mathrm{h}} = -43$ mV, $V_{\mathrm{lk}} = -65$ mV the membrane capacitance $\mathrm{C_m} = 26$ pF. Parameters used for TV cells are based on TS model responses fit to physiological data from Kuo *et al.* (2012). Resulting reversal potentials for TV cell's channels are: $V_{\mathrm{K}} = -81.5$ mV, $V_{\mathrm{Na}} = +50$ mV, $V_{\mathrm{h}} = -43$ mV, $V_{\mathrm{lk}} = -72$ mV and the membrane capacitance $\mathrm{C_m} = 35$ pF.

Table 2.3: Model Parameters and Properties

	Model Type				
	bushy-II	bushy-II-I	tstellate	bushy-I-II	tuberculoventral
$\overline{g}_{\mathrm{Na}}$, nS	1000	1000	3000	1000	5800
$\overline{g}_{\mathrm{HT}}$, nS	58	58	500	150	400
$\overline{g}_{\mathrm{LT}}$, nS	80	14	0	20	0
$\overline{g}_{\mathrm{A}}$, nS	0	0	0	0	0
$\overline{g}_{\mathrm{h}}$, nS	30	30	18	2	2.5
$\overline{g}_{\mathrm{lk}}$, nS	2	2	8	2	2
V_{rest}, mV	-63.9	-64.2	-64.1	-63.8	-63.6

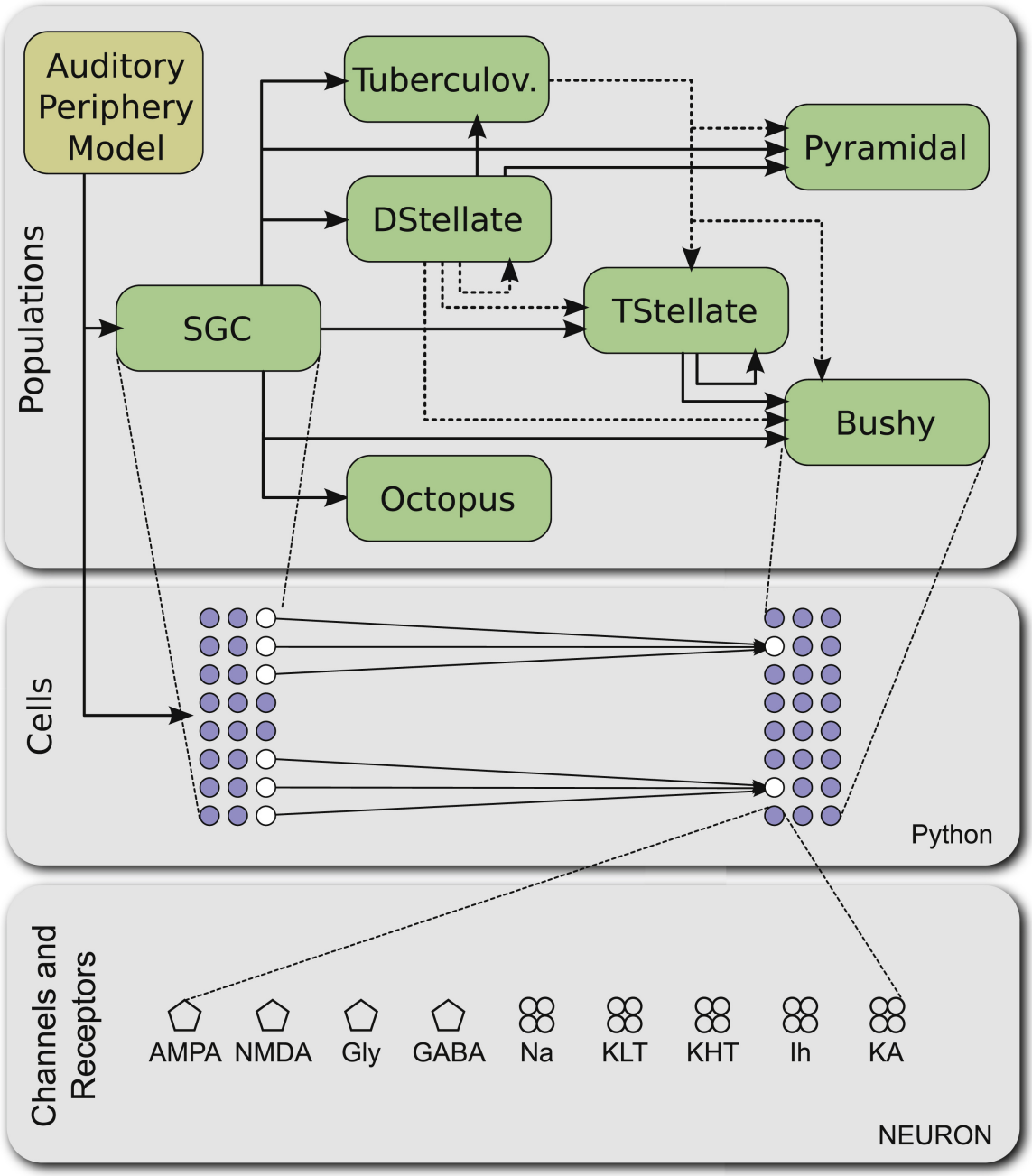

Figure 2.24: Manis and Campagnola (2018) model of the VCN. Solid lines indicate excitatory connections while dashed lines are inhibitory. The model takes channel equations from NEURON and create cells in a Python environment. Parameters used in this system to create cells and specific connectivity parameters can be found in the repository; `http://www.github.com/cnmodel`. From Manis and Campagnola (2018).

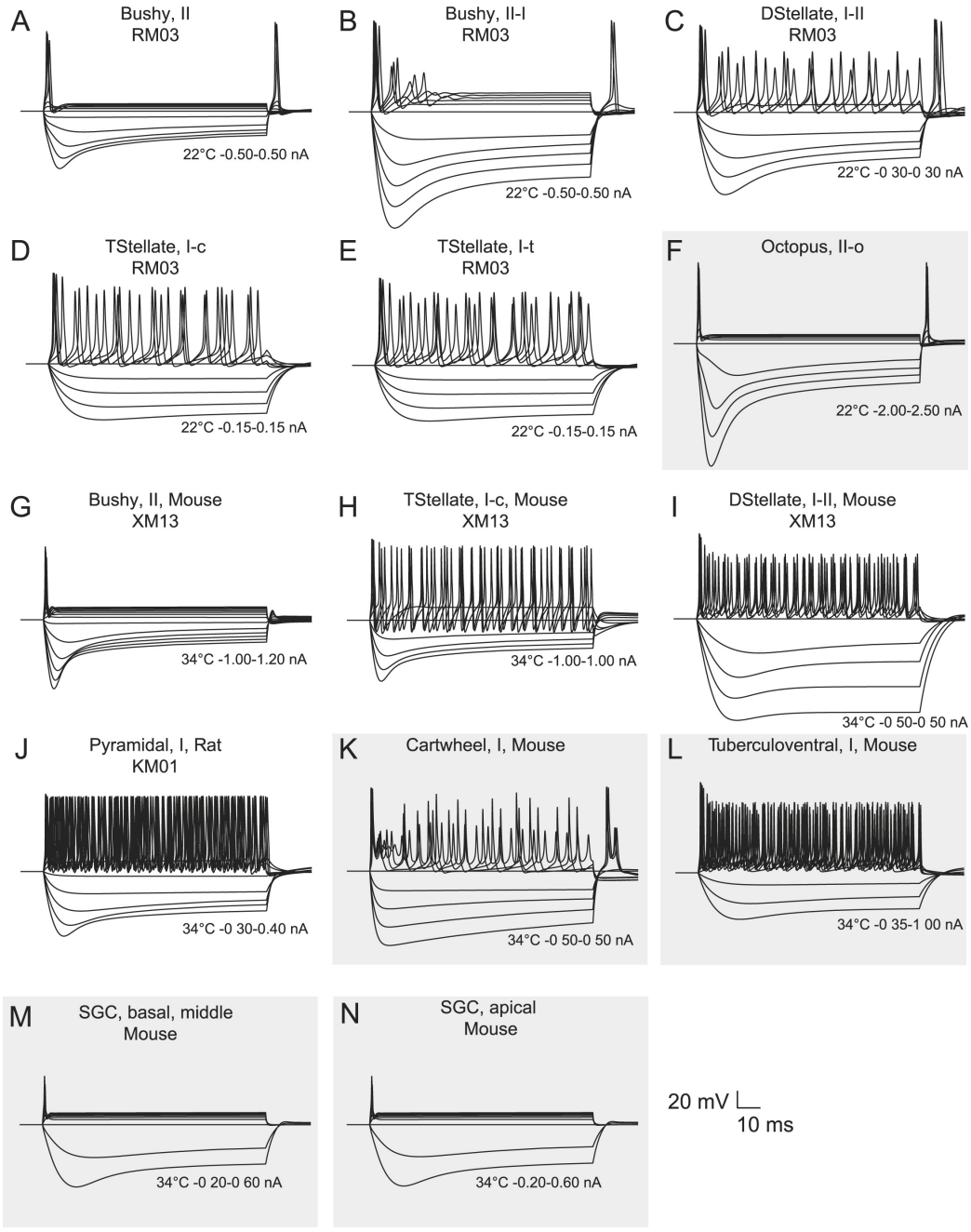

Figure 2.25: Individual cell responses of Manis and Campagnola (2018); Xie and Manis (2013); Rothman and Manis (2003c) to current injections. The numbers on the bottom right of each figure indicates the temperature and the range of current injection in nA. From Manis and Campagnola (2018).

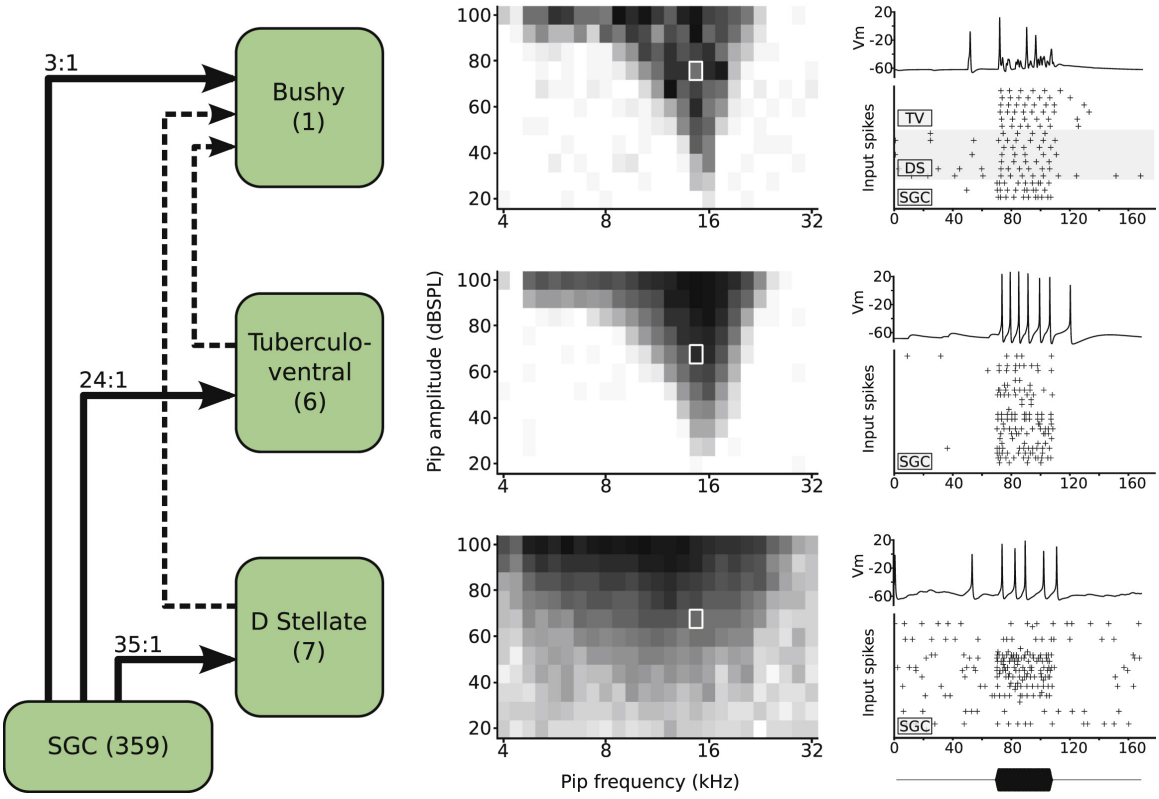

Figure 2.26: A microcircuit created with Manis and Campagnola (2018) modelling platform. The first layer consists of 7 DS cells take input from 35 AN fibers with various SR. The second layer has 6 TV cells taking excitatory inputs from 24 AN fibers with low and medium SR. The inhibitory input from DS to TV is disregarded for this simulation. The output bushy cell receives 3 excitatory AN inputs and receives inhibitory inputs from TV and DS cells. The middle column shows the response maps of cells to different frequency and amplitude tone stimuli. Third column shows a 76 dB 15kHz instance of the response map. From Manis and Campagnola (2018).

The connection parameters between the cells are given in Table 2.4. and Table 2.5. Rows indicate postsynaptic cell types while the columns represents the presynaptic cells. Table 2.4 shows the number of presynaptic cells (rows) to connect to the single postsynaptic cell (columns). Table 2.5 shows the variance of presynaptic cell frequency range. The values indicates the sigma of lognormal distribution in units of octaves.

Table 2.4: Synaptic Convergence Parameters (number of cells)

	Model Type					
	bushy	tstellate	dstellate	octopus	pyramidal	tuberculoventral
ANF	3.3	6.5	35	60	48	24
dstellate	7	20	3	0	15	15
tstellate	0	0	0	0	0	0
tuberculoventral	6	6	0	0	21	0
pyramidal	0	0	0	0	0	0

Table 2.5: Synaptic Convergence Range Parameters (octaves)

	Model Type					
	bushy	tstellate	dstellate	octopus	pyramidal	tuberculoventral
ANF	0.05	0.1	0.4	0.5	0.1	0.1
dstellate	0.208	0.347	0.5	0	0.2	0.2
tstellate	0.1	0.1	0	0	0	0
tuberculoventral	0.069	0.111	0	0	0.15	0
pyramidal	0	0	0	0	0	0

Eager *et al.* (2004) created a TS microcircuit model to check the representation of the vowel /ε/ in firing patterns of TS cells. They used the Heinz *et al.* (2001) ARLO model as auditory nerve inputs and the Rothman and Manis (2003c) model as VCN cell models. In their microcircuit, TS cells receive excitatory input from ANFs while receiving inhibitory inputs from DS and TV cells. The inhibition recevied from DS cells is wide-band and from TV cells is narrow-band. TV cells are modelled as Type I-c, and excited by ANFs while receiving strong inhibition from DS cells. DS cells

are modelled as Type I-II and receive wide-band inputs from ANFs. DS cells show On-C response to tone stimuli. TS cells modelled as Type I-t.

They found that when TS cells are stimulated with only high SR ANFs, they show chopper type responses. When inhibition from TV and DS cells are included, the response turns into onset type. If low SR inputs are also added, the response type becomes a transient chopper (Fig. 2.27). Using this configuration, their network succesfully captured formant frequencies in its firing pattern (Fig. 2.28).

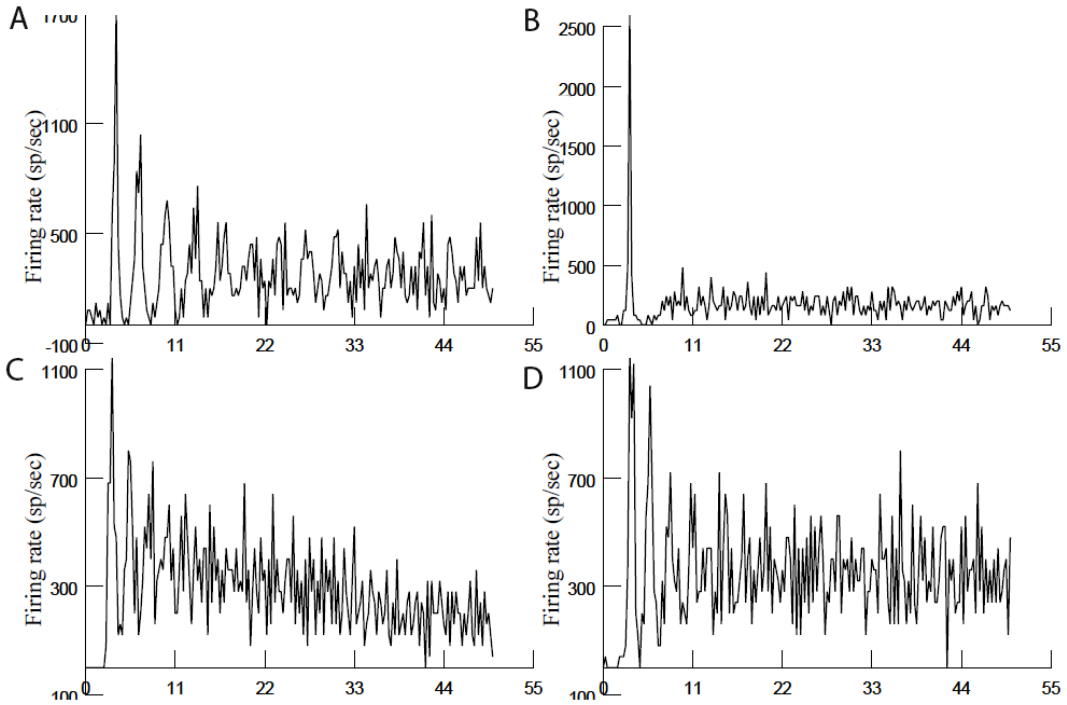

Figure 2.27: TS microcircuit response for different excitatory-inhibitory input configurations. (A) High SR excitatory ANF input only. Chopper response is observed. (B) Inhibition from TV and DS cells added to the configuration. Onset response is obtained instead of chopper. (C) High SPL low SR ANF input only. (D) PSTH of TS cells receive high and low SR ANF input and inhibition from DS and TV cells. Transient chopper response is observed. From Eager *et al.* (2004).

One of the biggest challenges in network modelling research is the reproducibility

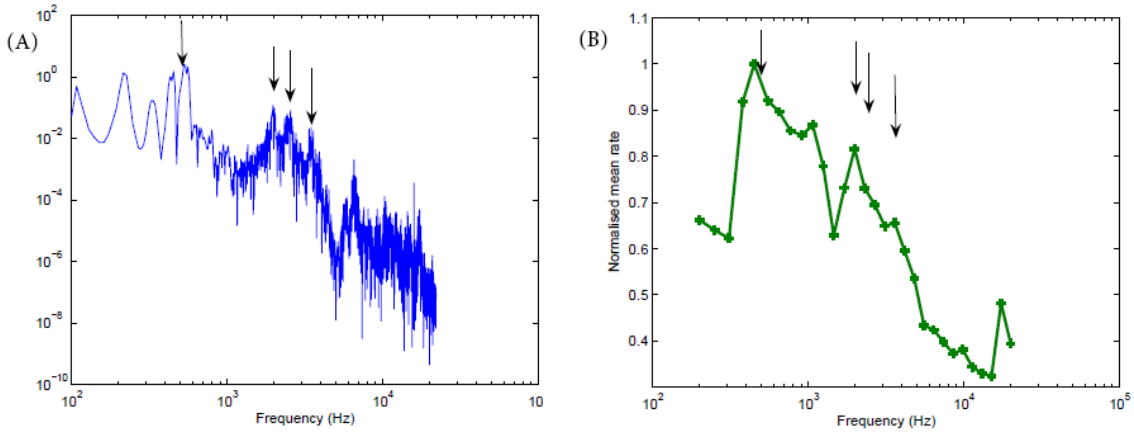

Figure 2.28: (A) FFT spectrum of vowel /ε/. (B) Representation of vowel /ε/ in Eager *et al.* (2004) in the firing profile of TS microcircuit. Arrows indicate formant frequencies. From Eager *et al.* (2004).

of the network by other researchers. Eager (2013) used the Nordlie *et al.* (2009) model summary table framework to represent parameters and protocols used in the model to create VCN microcircuits. Manis and Campagnola (2018) stores parameters in table format on their code repository so that researchers can easily access, see, or make changes in the parameters. The problem faced while creating the network model in this thesis was the modelling platform issue. In this thesis all of the synaptic and channel mechanisms are built by the writer in MATLAB while the base studies are using Python and NEURON. This makes some of the mechanisms used in other models ambiguous and makes it difficult to reproduce the same results.

Chapter 3

Methods and Results

In this thesis, a bottom-up approach is used to model microcircuits of the VCN. First, individual cell models are tested by applying current injection. Then the synapse model is tested by connecting ANFs with a bushy cell model to check if correct membrane voltage changes are obtained. By using this synapse model, cells are connected so that AN-like inputs can be presented to cell models to create and compare PSTHs. After the cell model behaviour is confirmed by checking PSTHs and regularity of firing, a small microcircuit is created to reproduce results presented in Manis and Campagnola (2018). Each step is tested and compared with physiological and simulation data presented in previous sections.

3.1 Individual Cell Model Simulations

Cell models presented in Rothman and Manis (2003c) and Manis and Campagnola (2018) are implemented using MATLAB 2016a on a computer with Intel® Core™i7-7700HQ CPU @ 2.80GHz with 16GB DDR4 RAM. Differential expressions that represent cells behaviour are written in a function called mainODE to be later solved by a built-in ordinary differential equation (ODE) solver, ODE45, in MATLAB. In simulations, cells are kept in a resting state prior to applying the input stimuli. To find values of resting state variables (membrane voltage and activating/inactivating gating particles) the cell is simulated using random parameter set and without presenting any input stimuli so that the system comes to the resting state. After a sufficient simulation time has passed, final steady state values are stored in vector form to be used in later simulations as initial values of variables.

Each cell model was tested by applying an external current (I_{ext}) to simulate the direct current injection procedure. In Chapter 2, Fig. 2.25 shows individual cell models responses. Fig. 3.1 shows some cell types current injection simulation results. The results are in line with those presented in Fig. 2.25.

3.2 Synaptic Process Simulations

After individual cell models are validated, synapse mechanisms are tested. The synaptic model used in this thesis is a simple exponential model. EPSPs caused by a single synaptic input spike are modelled as an exponential decay with a time constant of 0.4 msec. Inhibitory-post-synaptic-potentials (IPSPs) are modeled as double exponential functions with a rise time of 0.4 msec and a fall time of 2.5 msec. In the Manis and

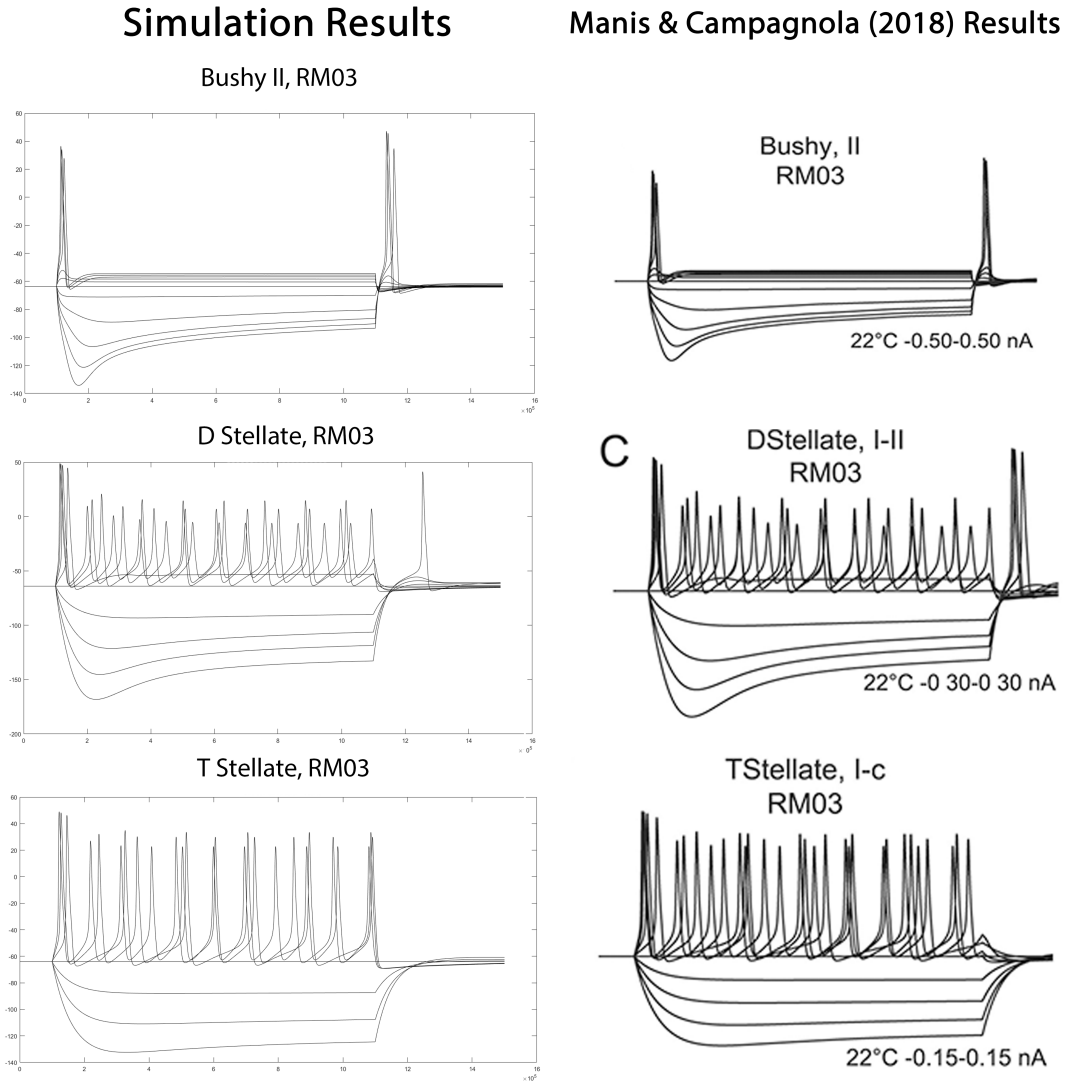

Figure 3.1: Current injection simulation results and comparison with results presented in Manis and Campagnola (2018).

Campagnola (2018) modelling environment, some built-in NEURON functions are used. In their modelling platform, there are two types of synaptic models: a basic synapse model which uses NEURON's 'exp2syn' function and a more detailed synapse model based on the synaptic model of Graham *et al.* (2001). The exp2syn function created for this research is based on Carnevale and Hines (2006) exp2syn function from NEURON. In NEURON, the 'weight' parameter is used to model individual spike's contribution to EPSPs/IPSPs. In this study g_{e} is used for this purpose in mainODE. The weight parameters used in Manis and Campagnola (2018) are provided in a table format in their source code. But when weight parameters were directly implemented in the code used in this thesis, the same results could not be obtained since the modelling platforms are different and intrinsic mechanisms are working in different ways. Therefore test code was written in Python so that the magnitude of each cell model EPSPs can be recorded then the parameters in mainODE were tuned to get same results in MATLAB.

To create a network out of individual cells, a synaptic model that is able to connect multiple presynaptic cells to one postsynaptic cell (synaptic convergence) and connect one presynaptic cell to multiple post synaptic cells (synaptic divergence) is needed. The signal is propagated through the network in the form of spike trains. Presynaptic neurons' voltage outputs are turned into spike trains according to a threshold value. The threshold value for the membrane voltage to be considered as a spike is -20 mV for all simulations. The exp2syn function takes spike train and connection type (whether the connection is excitatory or inhibitory) as inputs and produces a signal that represents the relevant conductance change in the postsynaptic neuron. The function uses MATLAB's built-in 'filter' function to convolve the spike train with the

exponential function. This conductance change is modelled in the membrane voltage Eq. 1.22 as I_e. An example of how exp2syn connects cells can be seen in Fig. 3.2.

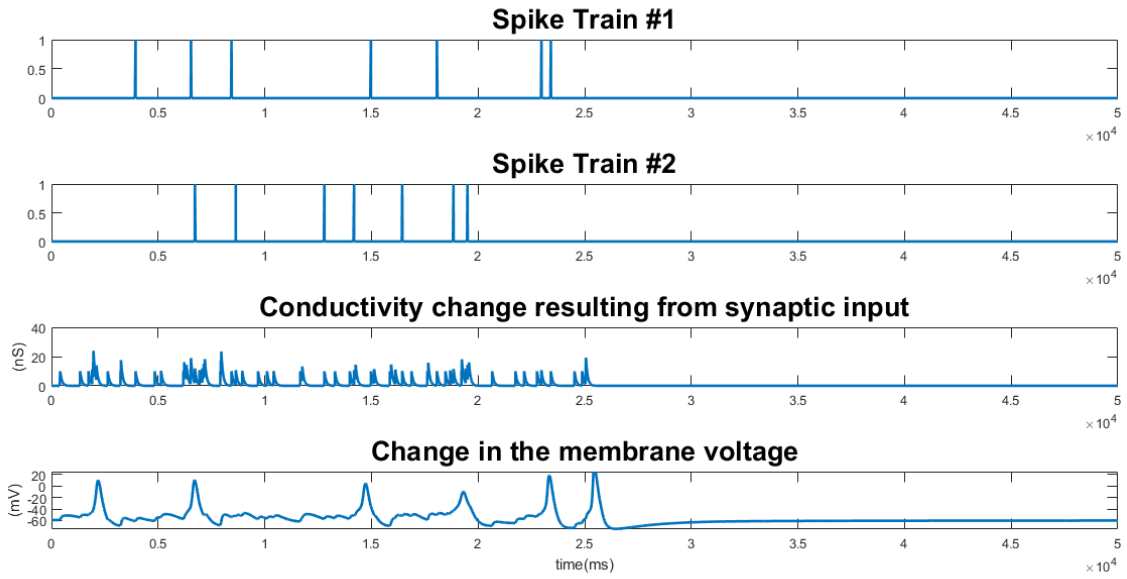

Figure 3.2: Bushy cell membrane voltage change over time to 10 low SR AN inputs.

3.3 PSTH Responses of Cells

In Chapter 2 different cell types' PSTH responses to tone bursts are presented. The procedures used in Rothman and Manis (2003c) and Eager (2013) are followed to recreate PSTH responses.

Type I-c cells show chopper response while Type II cells show primary-like responses. To see if the model mechanisms are working properly, PSTH responses of Type I-c and Type II cells stimulated with 10 or 50 (Figures 3.4, 3.5, 3.8 and 3.9) subthreshold AN inputs and 1 or 3 (Figures 3.6, 3.7, 3.10 and 3.11) suprathreshold

AN inputs are checked. The model is presented with a 100 ms tone burst with rise/-fall time of 2.5 ms. The stimulus has a frequency of 5 kHz with 30 to 60 dB SPL. The CF of AN fibers are 5 kHz for all simulations. The ANF model parameters are arranged in a way to not to have any IHC or OHC damage. The PSTH bin width is 0.1 ms. The bin width used for calculating CV is 1 ms. PSTHs are created by combining 500 trials.

The regular firing behaviour of Type I-c cells can be clearly seen in Fig. 3.3. Each dot in the raster plot represent a spike in that particular time bin. The regularity decreases with time and the firing becomes random close to the end of the stimulus. Low CV values of Type I-c cells also indicates the firing is regular. The chopping behaviour gets more prominent as the number of inputs increase.

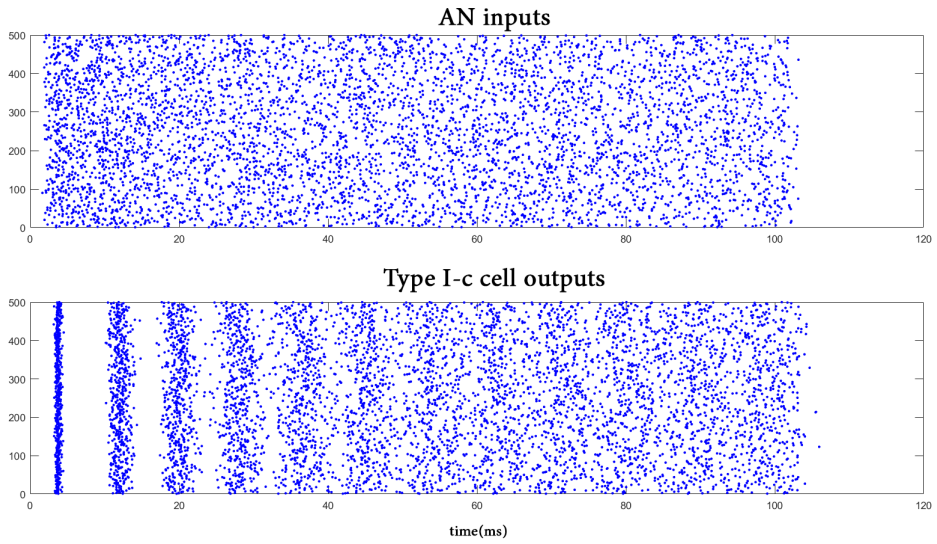

Figure 3.3: Raster plot of Type I-c cell response to AN like inputs.

For subthreshold inputs, Type II cells show onset type response while for suprathreshold inputs, cells perform better at following the input response (primary-like response). Higher CV values indicate the firing is not as regular as Type I-c cells.

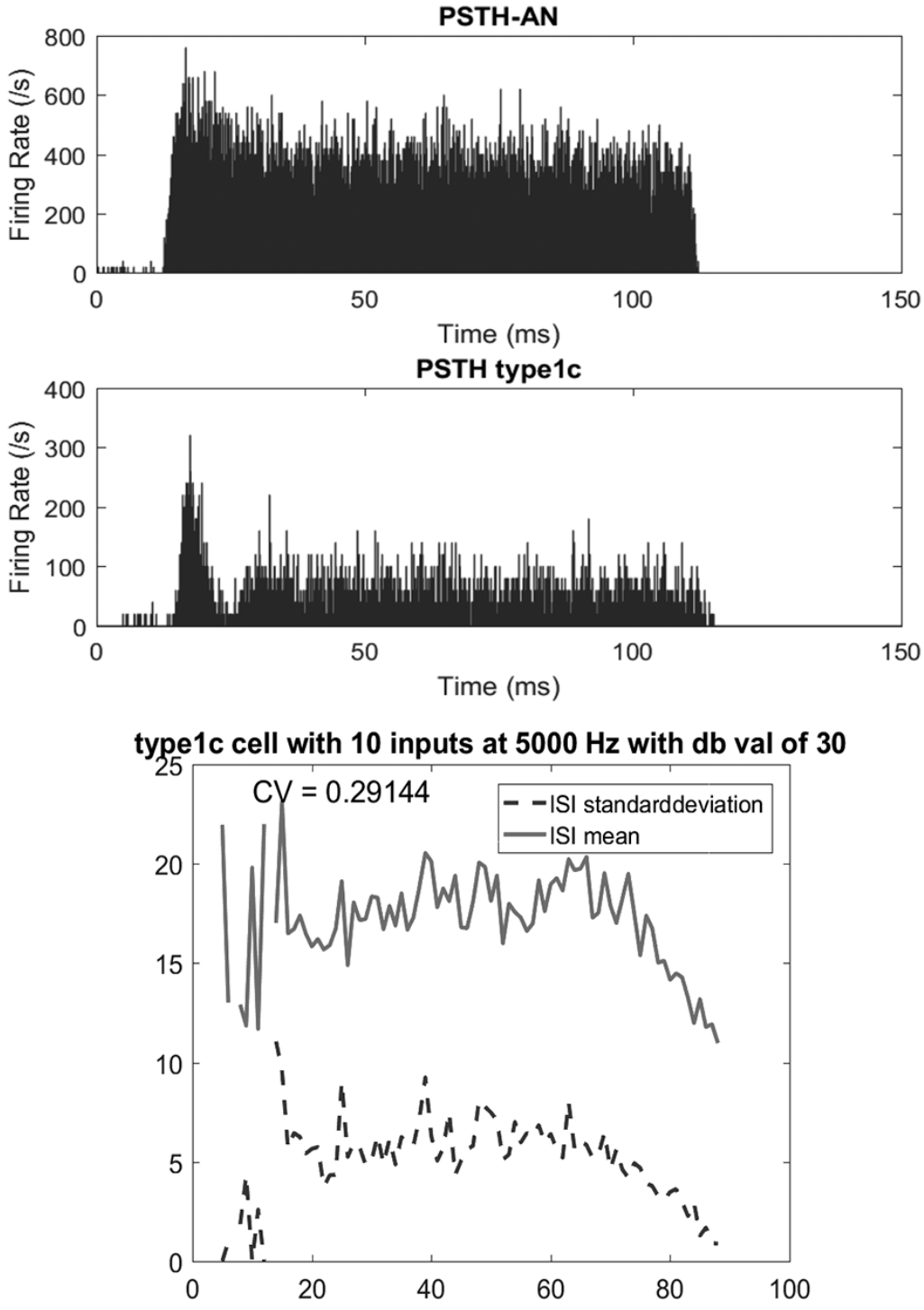

Figure 3.4: PSTH of Rothman and Manis (2003c) Type I-c cell response to 10 subthreshold AN inputs. Top figure shows the histogram of AN fibers.

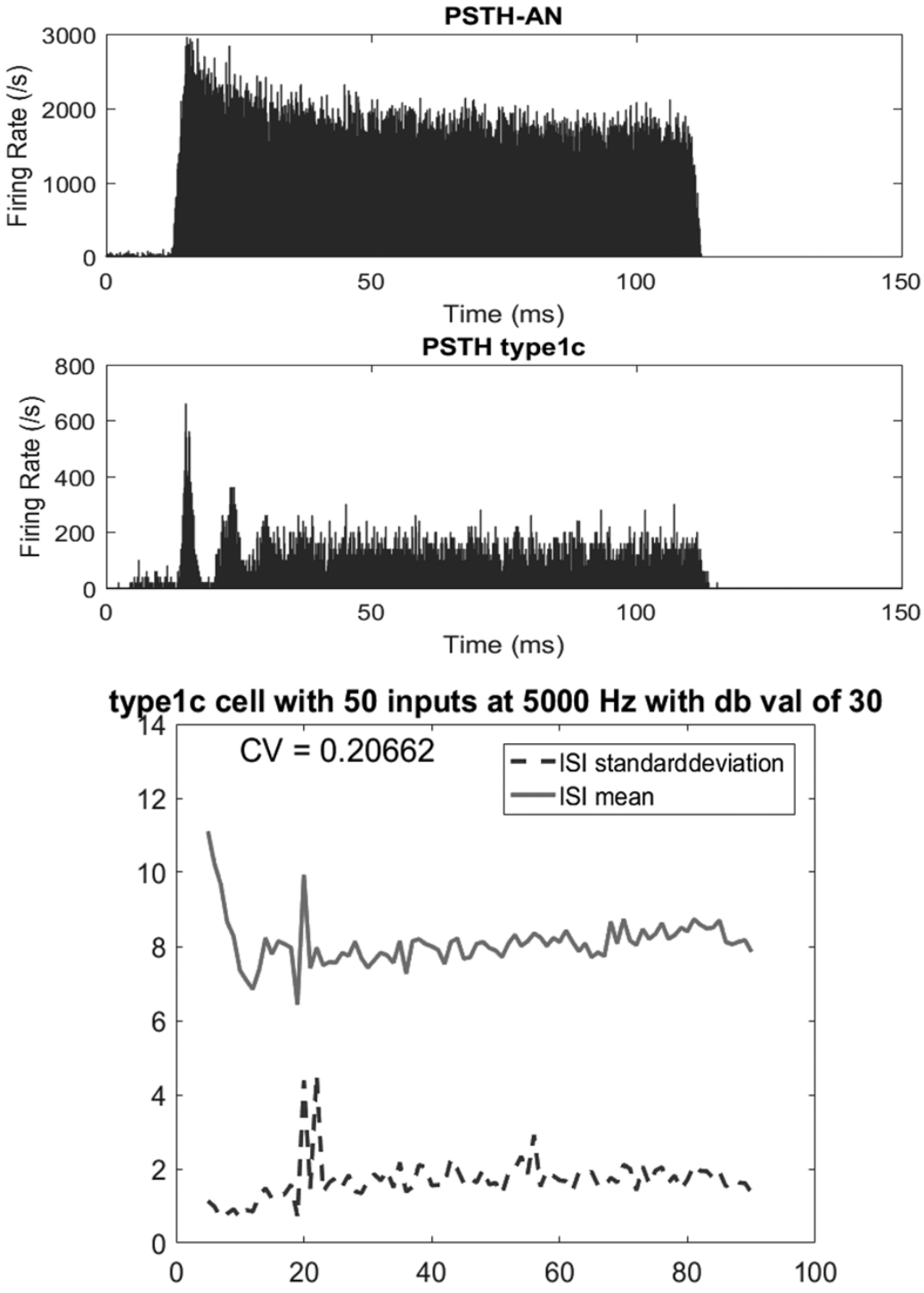

Figure 3.5: PSTH of Rothman and Manis (2003c) Type I-c cell response to 50 subthreshold AN inputs. Top figure shows the histogram of AN fibers.

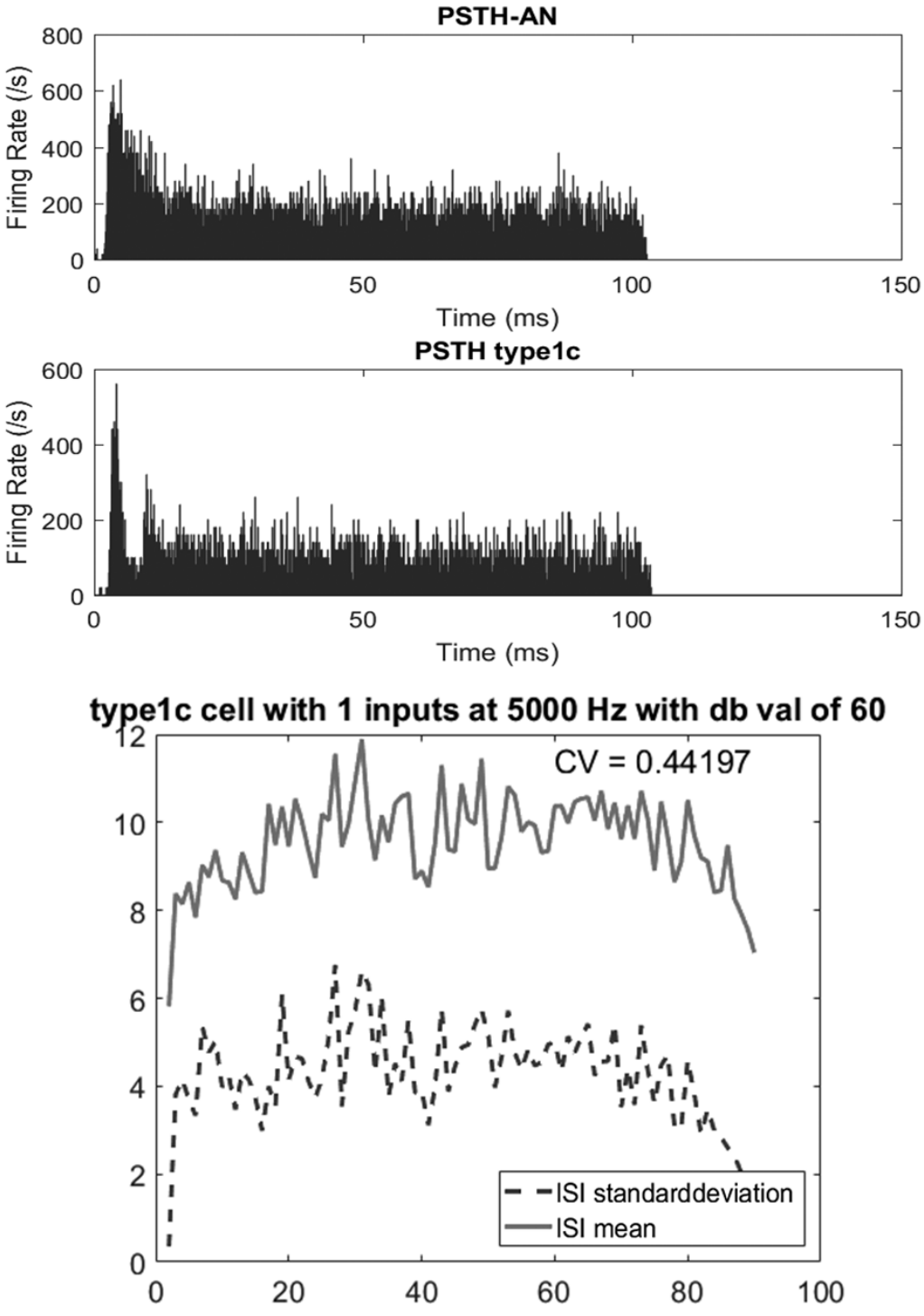

Figure 3.6: PSTH of Rothman and Manis (2003c) Type I-c cell response to 1 suprathreshold AN input. Top figure shows the histogram of AN fibers.

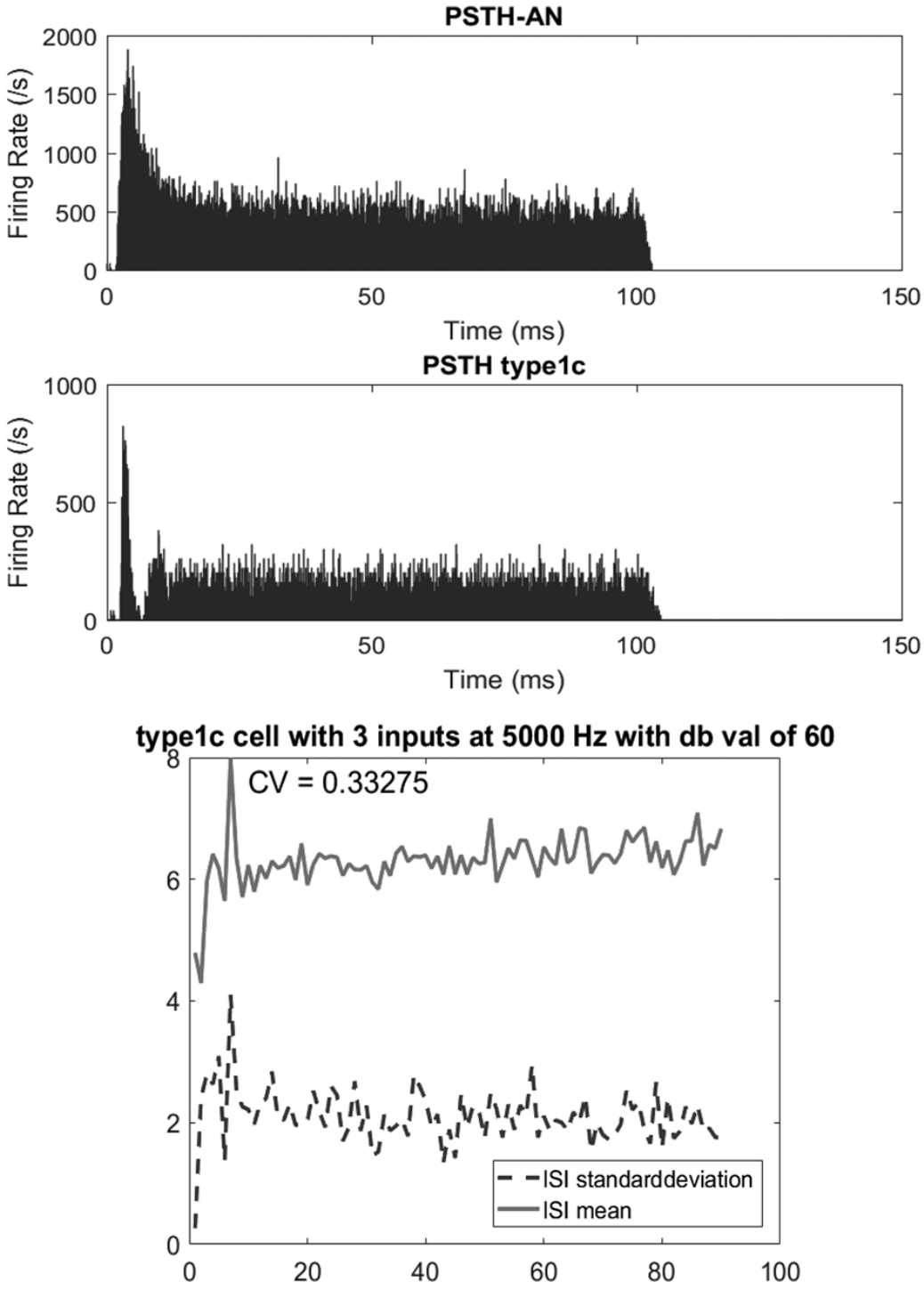

Figure 3.7: PSTH of Rothman and Manis (2003c) Type I-c cell response to 3 suprathreshold AN inputs. Top figure shows the histogram of AN fibers.

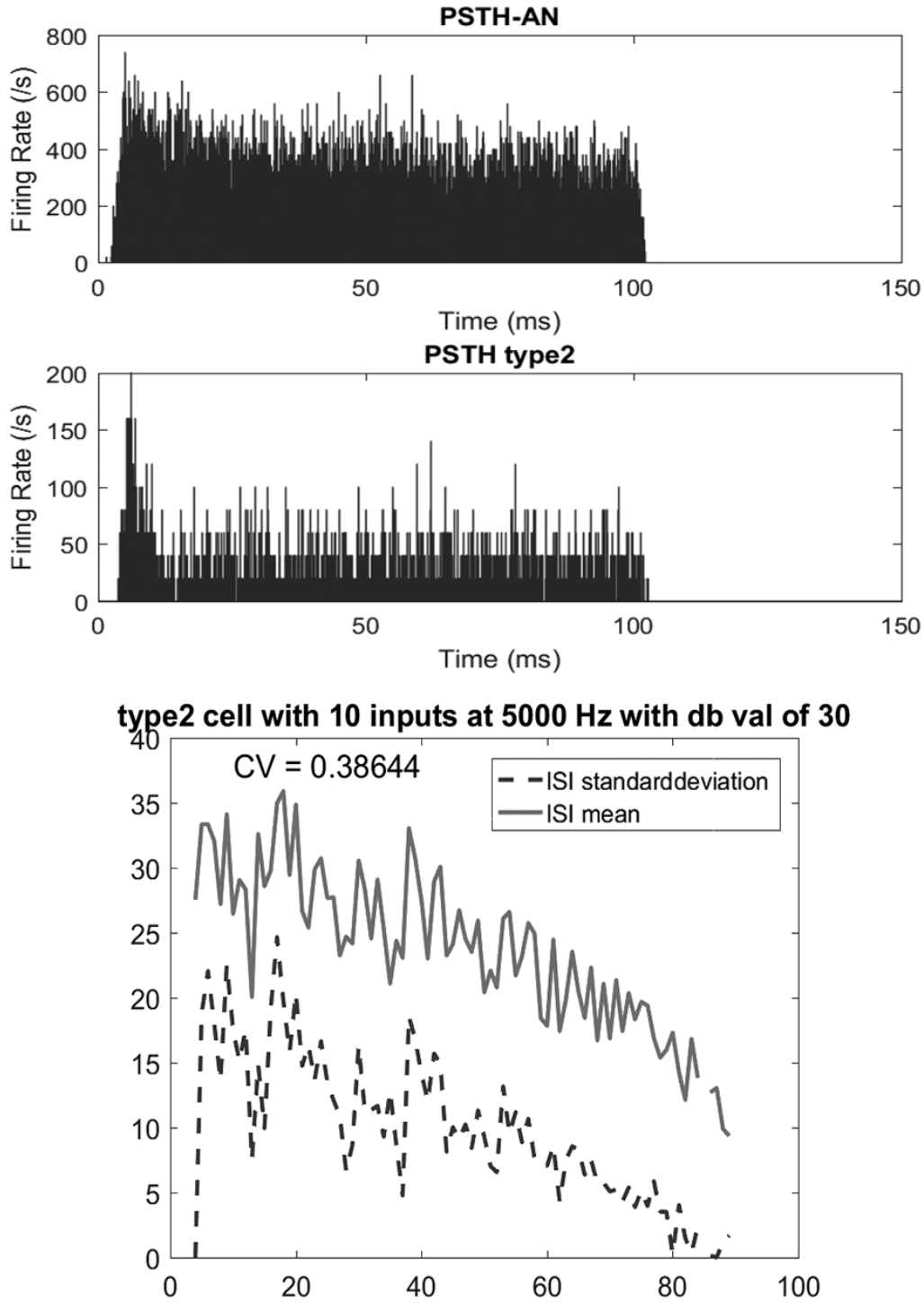

Figure 3.8: PSTH of Rothman and Manis (2003c) Type II cell response to 10 subthreshold AN inputs. Top figure shows the histogram of AN fibers.

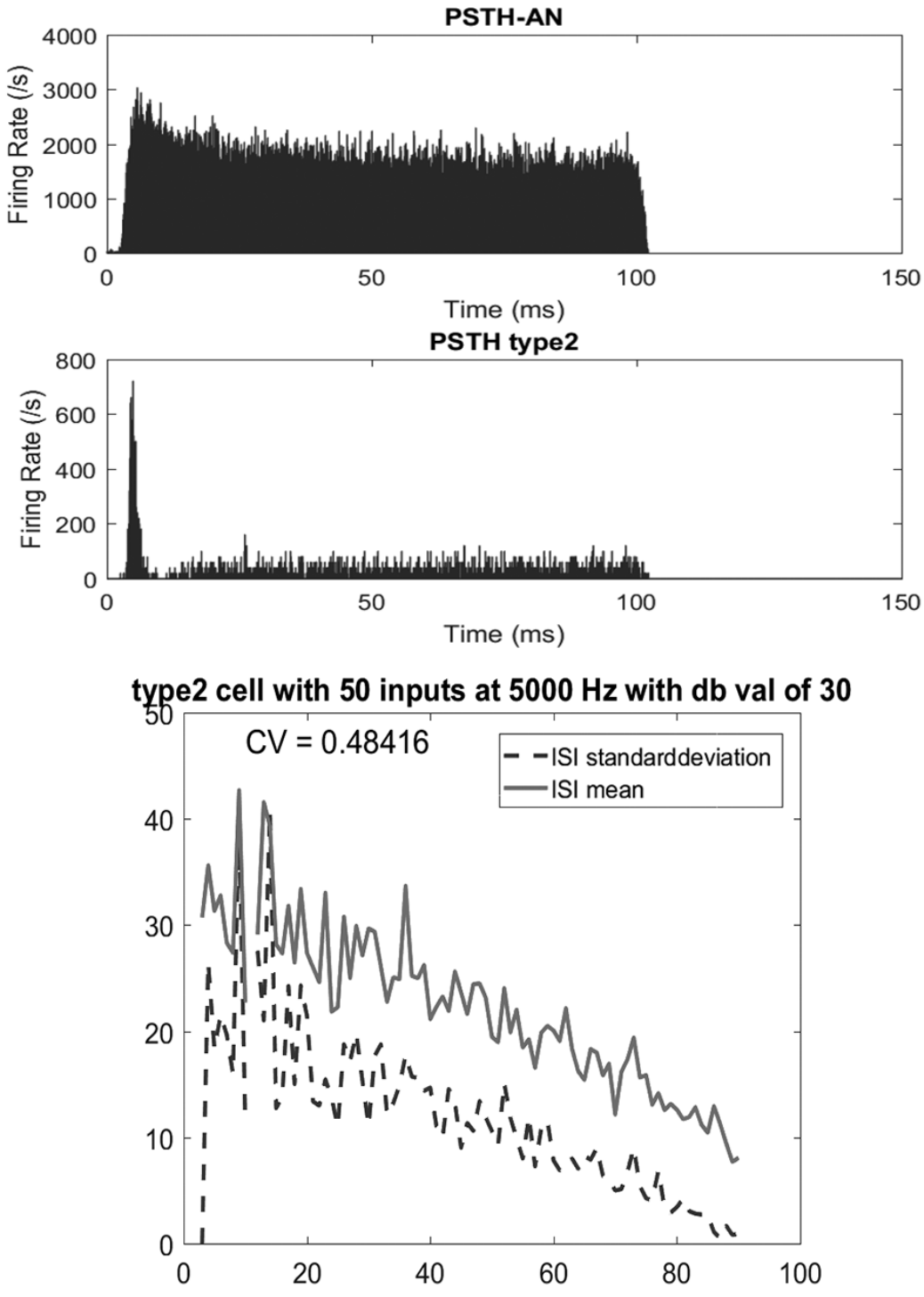

Figure 3.9: PSTH of Rothman and Manis (2003c) Type II cell response to 50 subthreshold AN inputs. Top figure shows the histogram of AN fibers.

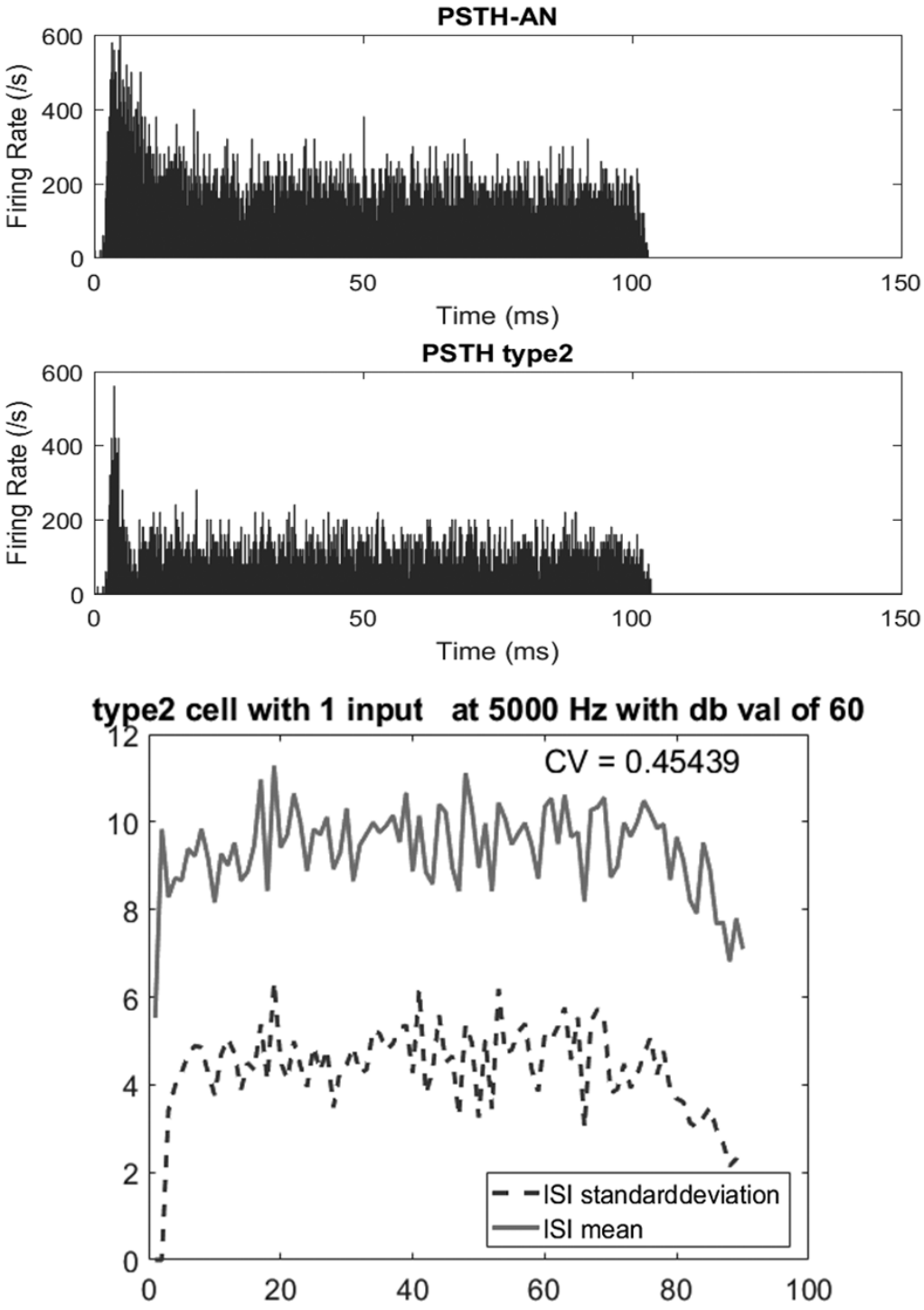

Figure 3.10: PSTH of Rothman and Manis (2003c) Type II cell response to 1 suprathreshold AN input. Top figure shows the histogram of AN fibers.

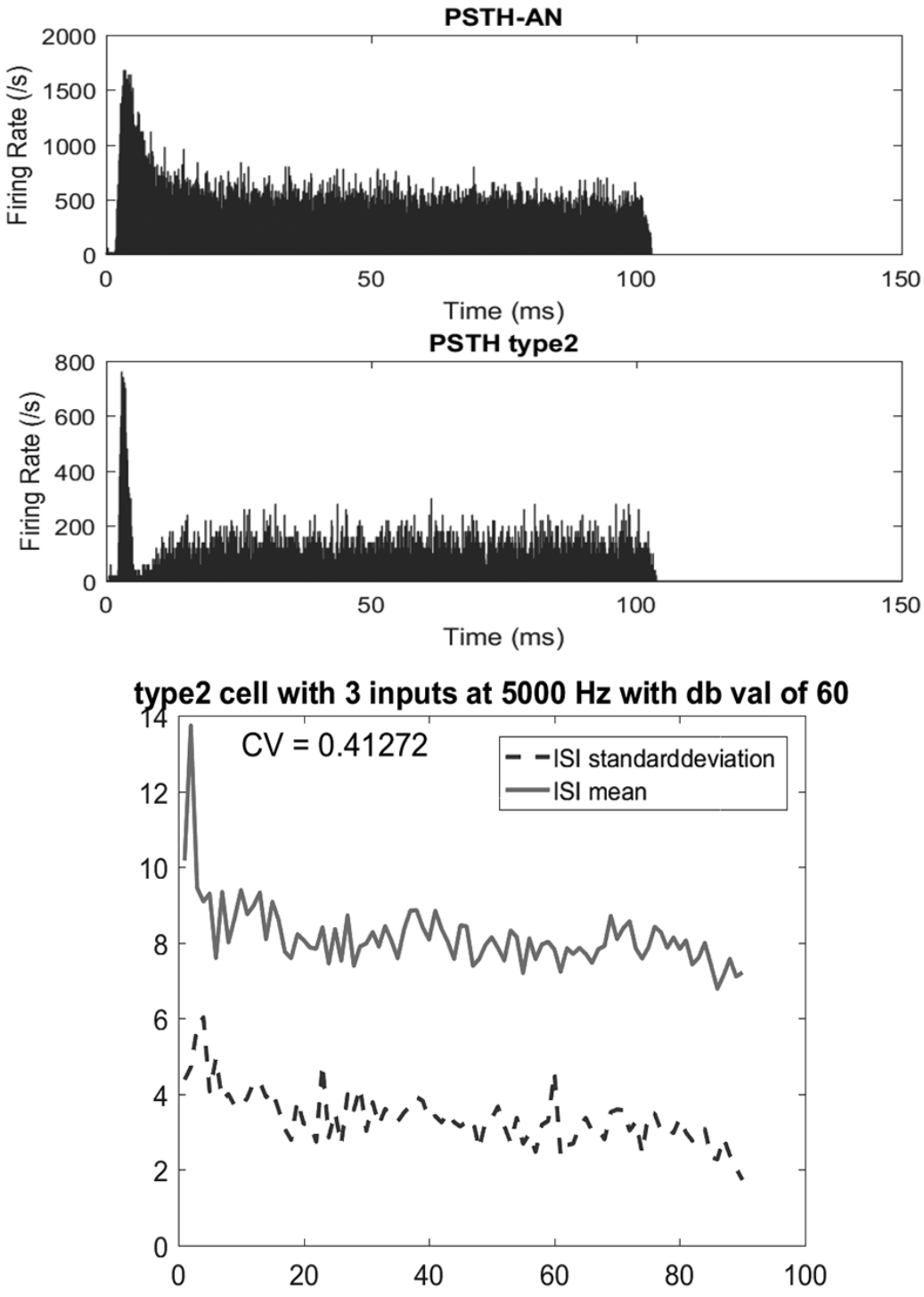

Figure 3.11: PSTH of Rothman and Manis (2003c) Type II cell response to 3 suprathreshold AN inputs. Top figure shows the histogram of AN fibers.

These results are in agreement with the results presented in Rothman and Manis (2003c). This indicates that the mechanisms used in this thesis are working correctly. The same procedures are used for testing updated Manis and Campagnola (2018) cell types. Bushy cells show onset and primary-like responses to sub and suprathreshold tone burst inputs like Type II cells do. TV cells show chopper responses similar to classic Type I-c cell responses. Updated DS cell models show unexpected results in these simulations. The cause of this should be inspected further.

3.4 Inhibition Effect on PSTH Responses

T stellate cells are one of the main cell types that propagates information to the upper levels of the ascending auditory pathway. They take excitatory inputs from ANFs and inhibitory inputs from DS and TV cells. In the previous section, PSTHs of Type I-c cells are examined. However, these simulations only include the excitatory inputs from ANFs. When an inhibitory input is presented to the cell along with excitatory inputs, the cell response drastically changes (Fig. 3.14). When a Type I-c cell is subjected to low SR ANF inputs with the same CF, it shows a chopping response, but when an inhibitory input is also presented to the system, the cell exhibits an onset type response. When both low SR and high SR inputs are presented with inhibition, the response becomes an transient chopper since the firing is highly irregular (CV = 0.63175). Inhibitory input used in these simulations is a spike train with uniformly distributed spike times.

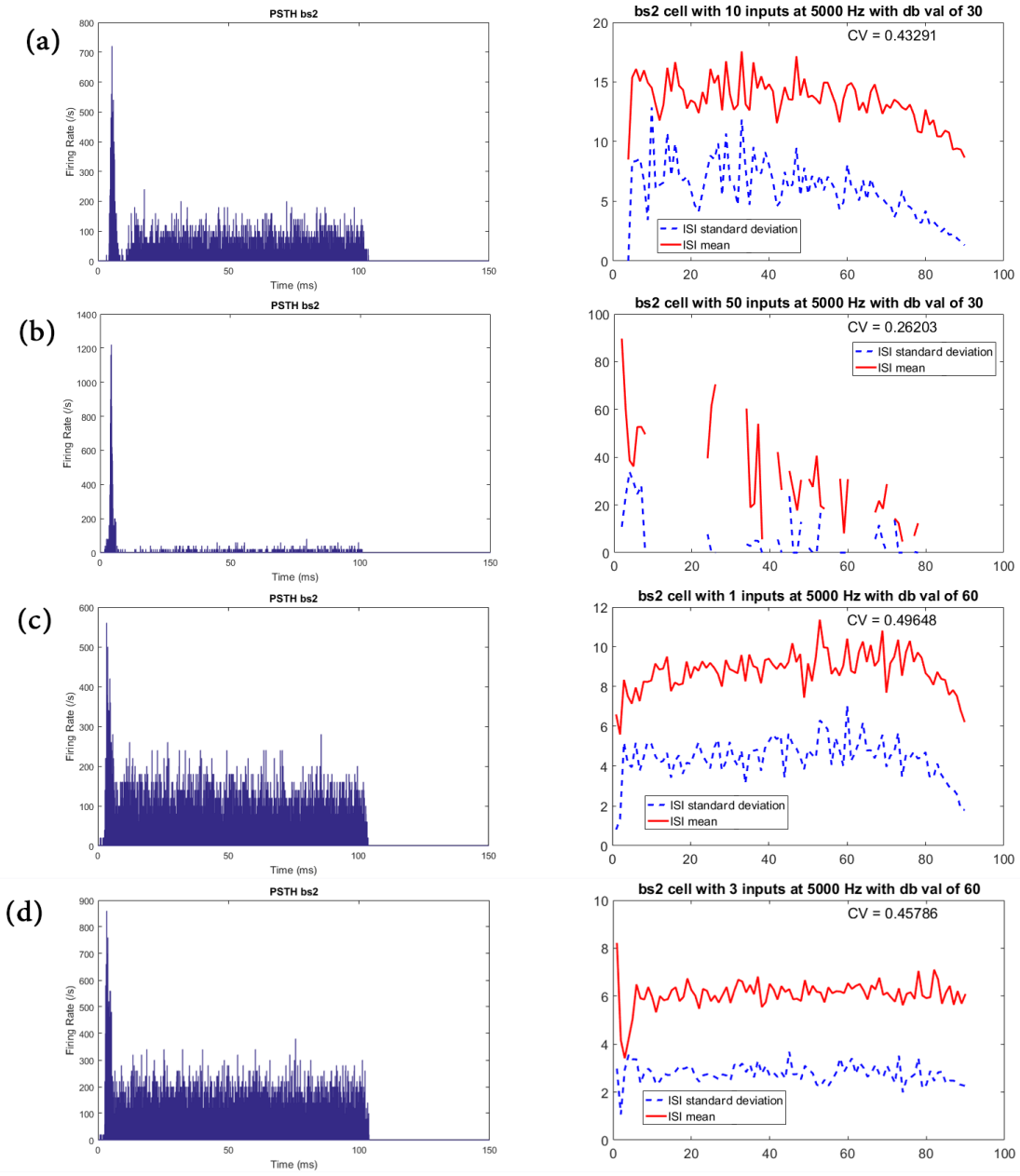

Figure 3.12: PSTH responses and CV of Manis and Campagnola (2018) bushy cell model to (a) 10 subthreshold (b) 50 subthreshold (c) 1 suprathreshold (d) 3 suprathreshold medium SR ANF inputs.

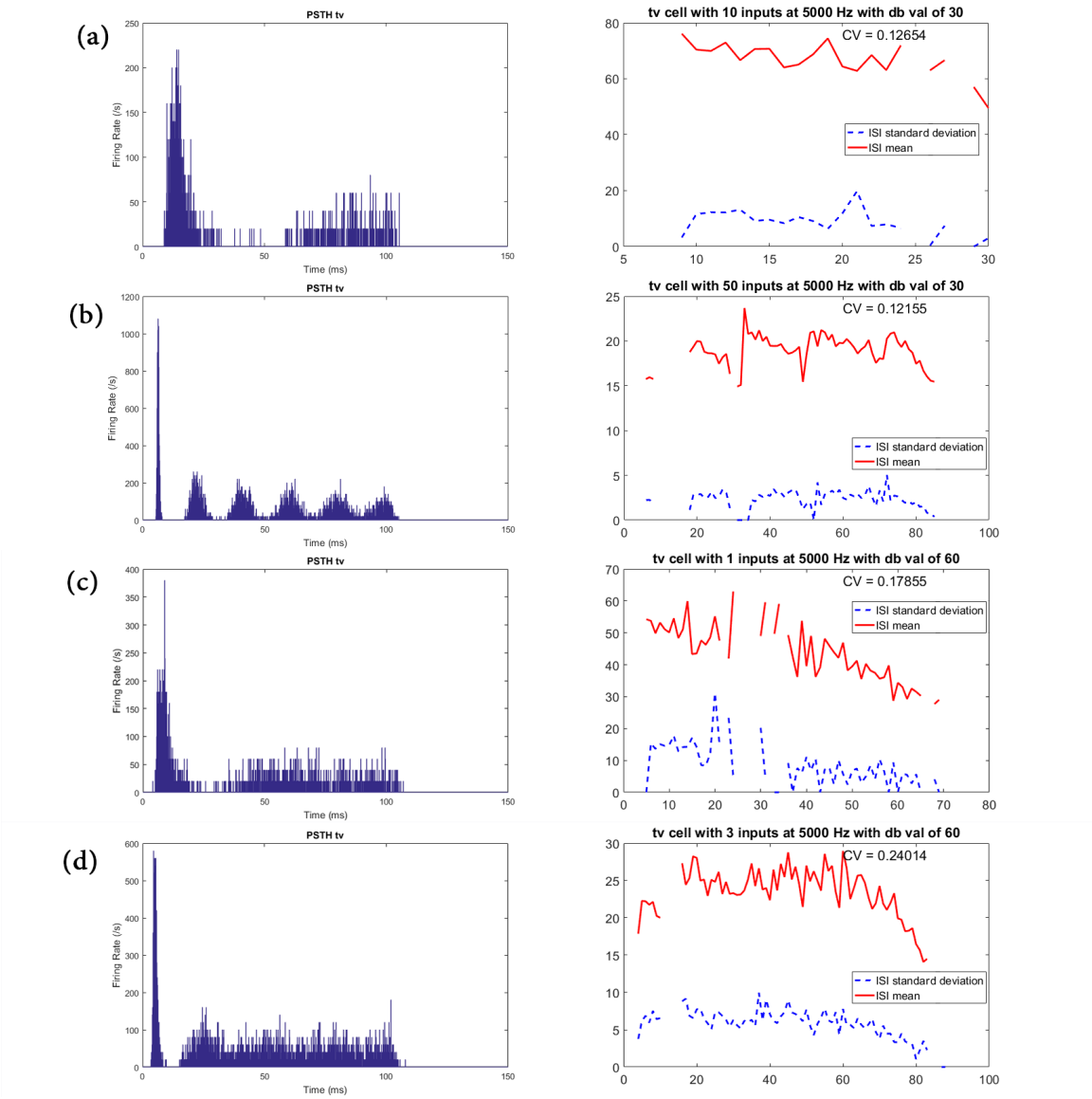

Figure 3.13: PSTH responses and CV of Manis and Campagnola (2018) TV cell model to (a) 10 subthreshold (b) 50 subthreshold (c) 1 suprathreshold (d) 3 suprathreshold medium SR ANF inputs.

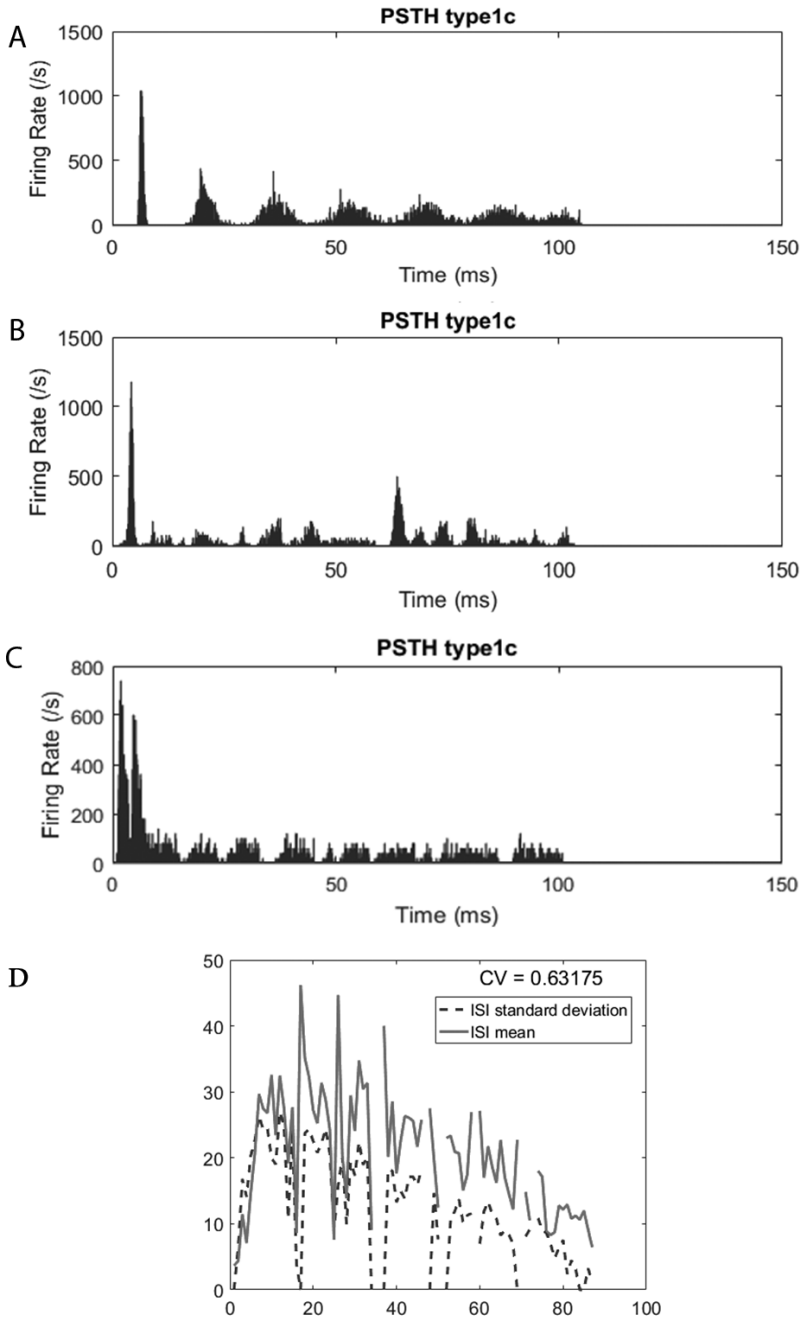

Figure 3.14: Type I-c cells PSTH response to different excitatory - inhibitory input configurations. (A) Type I-c cell PSTH with 50 excitatory subthreshold low SR ANF inputs. (B) PSTH with 50 low SR ANF excitatory and arbitrary inhibitory input. (C) PSTH with 50 low SR and 50 high SR ANF excitatory and arbitrary inhibitory input. (D) CV of the latest configuration.

3.5 Response Maps of Manis and Campagnola (2018) Type Cells

Manis and Campagnola (2018) type cell models are also tested by creating response maps and comparing them with results presented in their paper. Response maps are created by applying tone bursts with different frequencies and SPLs to cells with a range of CFs. The connection parameters are based on Table 2.4. Manis and Campagnola (2018) made a demonstration by creating a small microcircuti model shown in Fig. 2.26. In this thesis, the same network structure is created. DS cells receive 36 inputs from low, medium and high SR ANFs. TV cells receive 24 inputs from low and medium SR ANFs. DS cells receive wideband excitation ($\sigma = 0.4$), TV cells receive more narrowband excitation ($\sigma = 0.1$). This can be seen in response maps. When compared with the response of TV cells, DS cell response map shows the cell responds to a wider range of inputs. This behaviour is propagated to bushy cells as a wideband inhibition and TV cells provide a more narrow band inhibition.

When presented with only 3 excitatory inputs from medium SR ANFs, bushy cell demonstrates a sharply tuned response map characteristic. As inhibition coming from DS and TV cells increased, the response map of bushy cell sharpens but eventually the response becomes more sparse (Fig. 3.16). TV cells are modelled as Type I-c cells for this simulations since the response map of Type I-c cell is sharper than what is obtained in TV cell simulation.

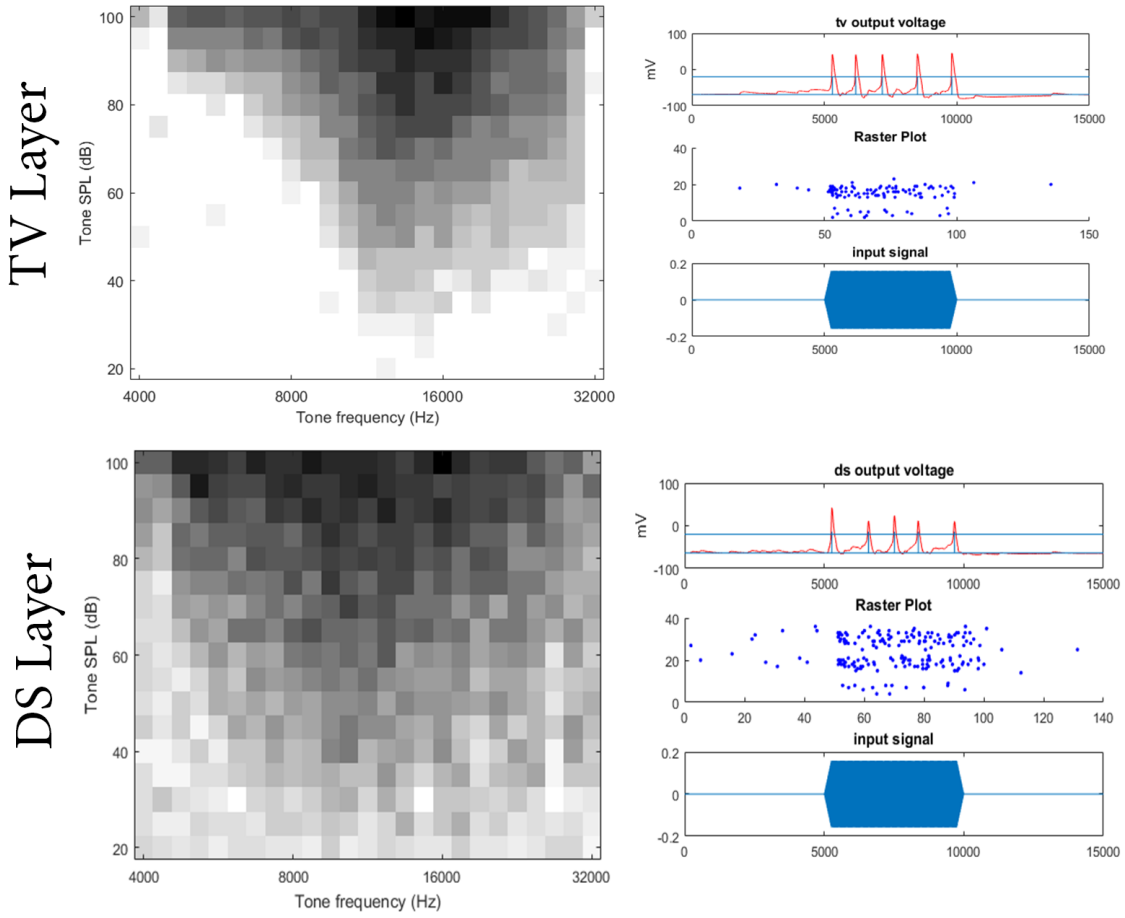

Figure 3.15: Manis and Campagnola (2018) type DS and TV cell response maps. Right column shows an iteration of the simulation when the stimulus intensity is 75 dB and the frequency is 14.672 kHz. Top plot shows the membrane voltage of cells and spike trains created from them. Middle panel shows the raster plot of AN inputs. Bottom panel shows the input tone burst.

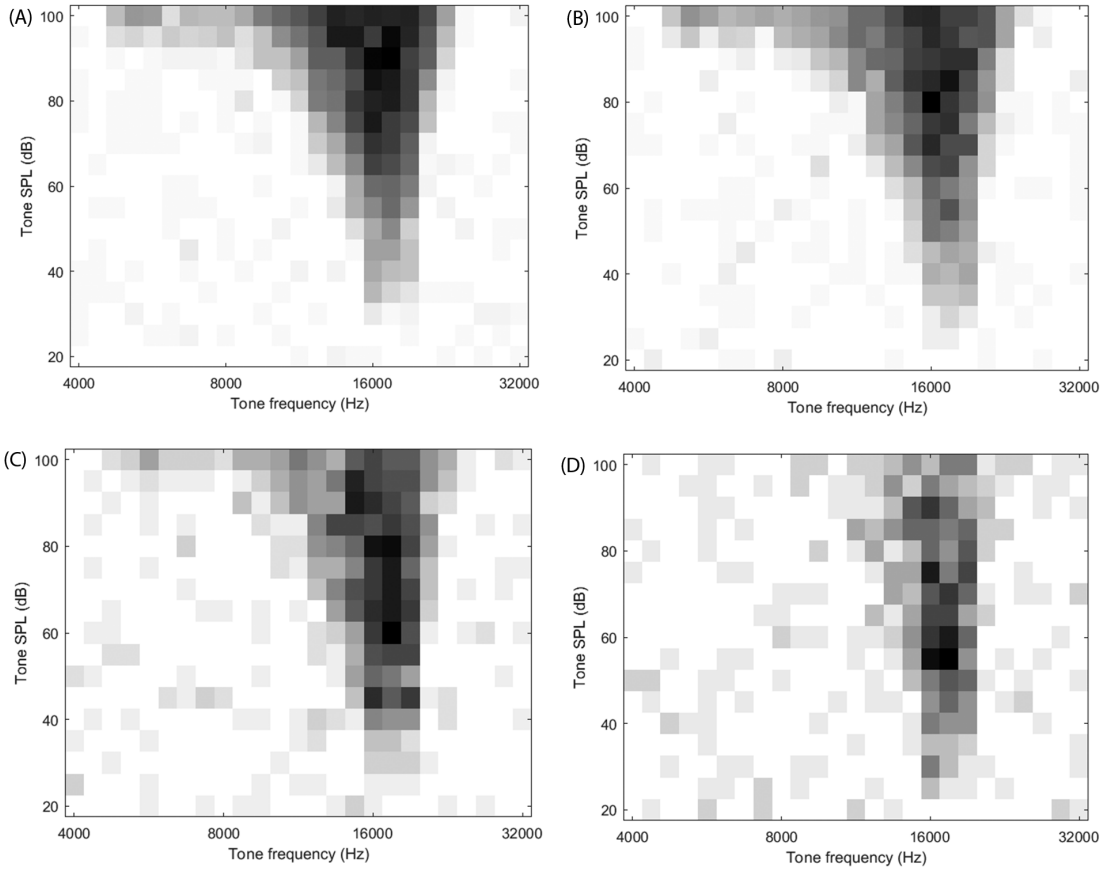

Figure 3.16: Manis and Campagnola (2018) type bushy cell response map for different inhibitory input configurations. (A) No inhibition, 3 suprathreshold AN inputs are applied. (B) With inhibition from DS and TV cells multiplied by 0.1. (C) The inhibitory multiplier raised to 0.25. (D) The inhibitory multiplier raised to 0.5.

3.6 Simulation Results of Pri and PriN Cells Response to Vowels

Blackburn and Sachs (1990) took recordings from Pri and PriN cell populations and created ALSR response plots to 35 dB, 55 dB and 75 dB input stimuli. Earlier this chapter, simulated Type II cell's response is obtained as Pri for 1 suprathreshold ANF input and PriN for 3 suprathreshold ANF inputs. Considering this, to investigate cell types' ALSR responses, either 1 or 3 suprathreshold ANF inputs are presented to Type II cells. ANFs were stimulated with the vowel /ε/ at different SPLs. The model's ALSR responses are presented in Fig. 3.17. Blackburn and Sachs (1990) presented that Pri cells are following the vowel representation in AN firing patterns better than PriN cells. Our simulation results are in agreement with their recordings in terms of Pri cells following ANF firing patterns to vowels better than PriN cells.

Type II cells in PriN configuration (3 suprathreshold inputs) are tested to see the inhibition effects. An arbitrary inhibitory input is presented. From 3.18 it can be seen that the inhibitory inputs reduction of the response is more prominent on high frequency harmonics. For lower stimulus SPL, the strength of the population response is weaker than higher ones as expected. This can be derived from the size of the boxes getting smaller.

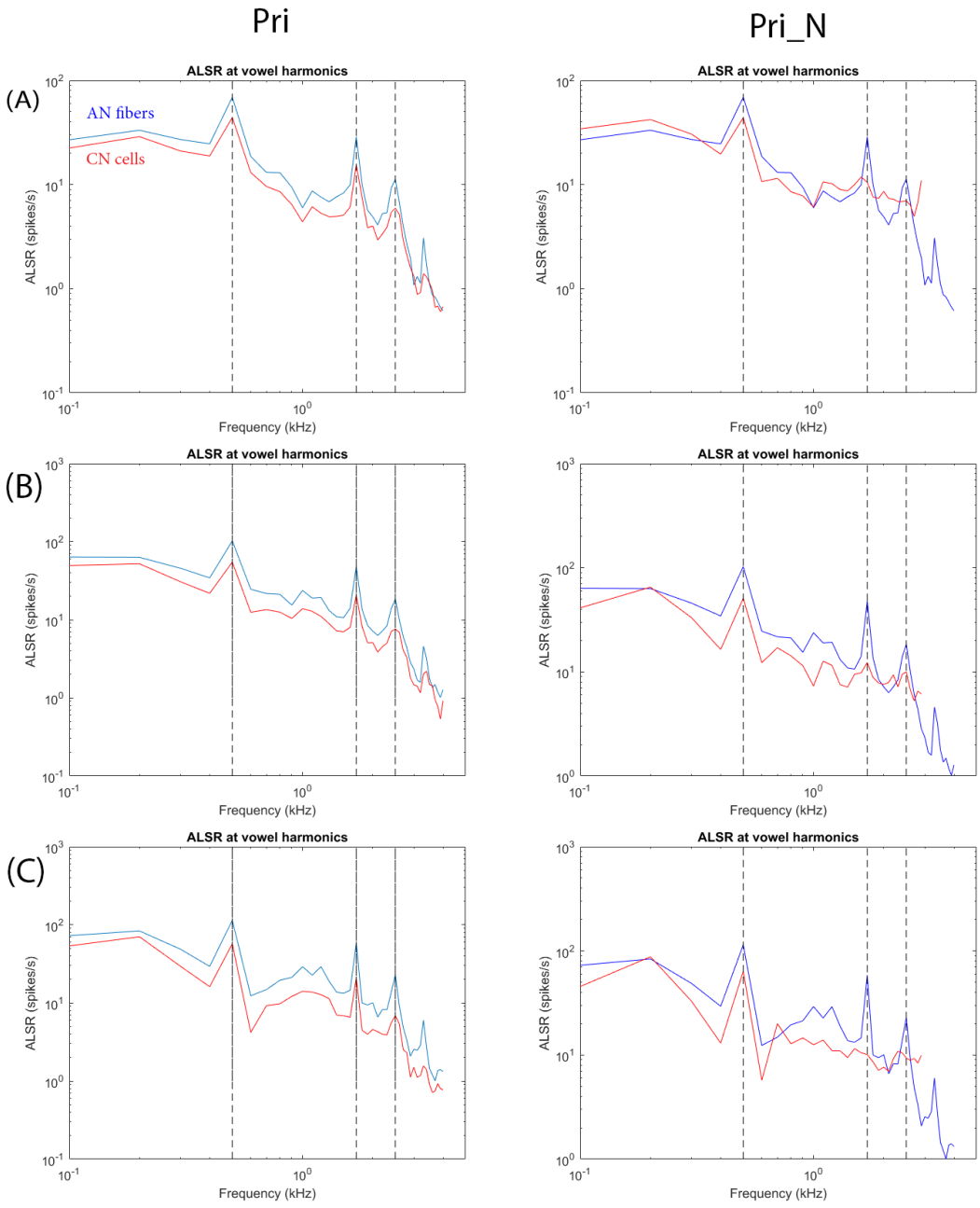

Figure 3.17: Comparison of ALSR simulation results for Pri and PriN cells. Blue lines indicate ANF ALSR response while red lines indicate Pri or PriN ALSR response. Vertical lines show first, second and third formant frequencies. (A) ALSR responses of Pri and PriN cells to 35 dB input stimuli. (B) ALSR responses of Pri and PriN cells to 55 dB input stimuli. (C) ALSR responses of Pri and PriN cells to 75 dB input stimuli.

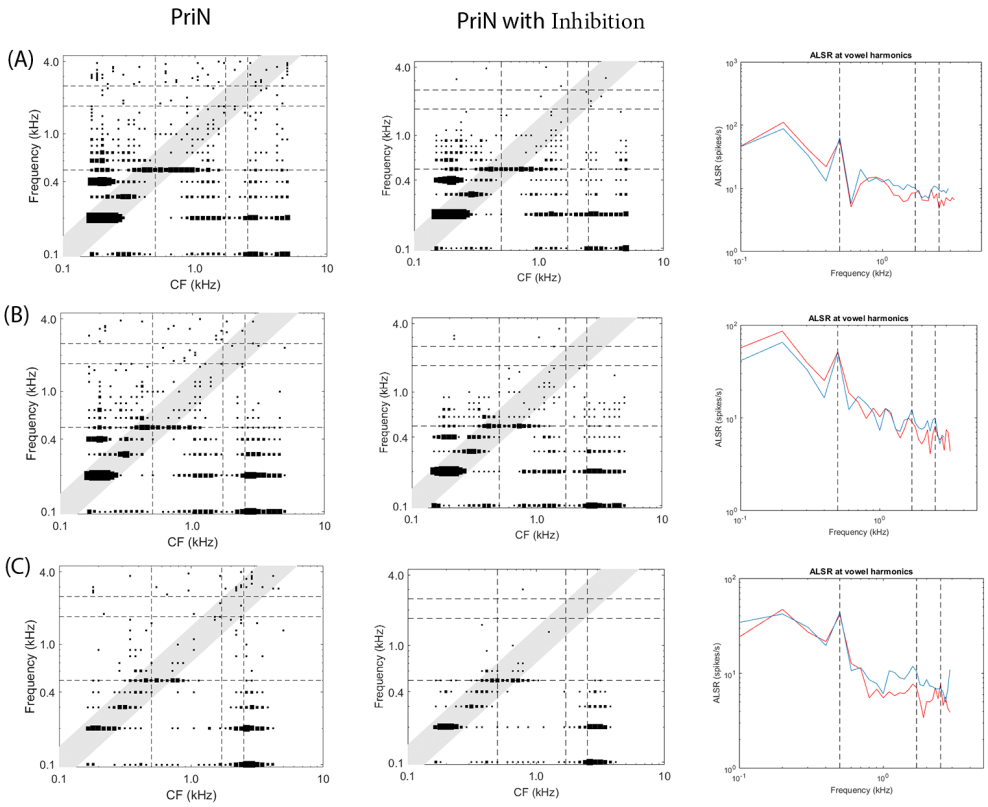

Figure 3.18: Comparison of ALSR and boxplot simulation results for PriN and PriN with inhibition. Left column presents boxplots of Type II cells (PriN response) to 3 suprathreshold inputs taken from (A) ANF response to 75 dB vowel /ε/, (B) ANF response to 55 dB vowel /ε/, (C) ANF response 35 dB vowel /ε/. Middle column shows the boxplot responses of PriN cells with excitatory and inhibitory inputs. Right column shows the ALSR responses to vowel stimuli of PriN cells with (red) and without (blue) inhibition.

Chapter 4

Conclusions and Future Work

4.1 Conclusion

In this thesis, model responses of principal cell types and microcircuit responses of the VCN to current injections, tone bursts and the phoneme /ɛ/ are inspected. Individual cell models and microcircuit structures were stimulated with outputs of the latest phenomenological Bruce *et al.* (2018) AN model. PSTHs and response maps were created to validate model mechanisms. Rothman and Manis (2003c) type models of the VCN cells are well established and tested throughout various research and extensively used in VCN modelling studies. Recently, Manis and Campagnola (2018) came up with updated versions of Rothman and Manis (2003c) cell models and provided a modelling platform for simulating microcircuits of the VCN.

Manis and Campagnola (2018) cell models are also tested through the same procedures as Rothman and Manis (2003c). Unfortunately, since the modelling platform is new, updated cell models provided in their work are not extensively tested yet. Therefore the results obtained in this thesis could not be compared with simulation

results from other research. However, by taking physiological data and Rothman and Manis (2003c) cell model responses into consideration, the updated Manis and Campagnola (2018) cell models developed in this thesis are seen to have close resemblence to the real world data.

In this thesis, inhibition effects on firing behaviour of cells were inspected by introducing arbitrary inhibitory input to Type I-c cell and creating a bushy cell microcircuit. In this microcircuit inhibition were presented by DS and TV cells. The results show that inhibitory inputs have a huge effect on regulating the firing behaviour of main cell types of VCN. As the inhibitory input's effect get stronger, the tuning of bushy cell responses to excitatory ANF inputs becomes sharper.

Inhibition's effect on bushy cells response to vowel /ε/ was also inspected by creating boxplots and ALSR plots. When inhibition was not presented, Pri cells follows the ANF firing pattern closer than PriN cells. This result was in agreement with what is presented in Blackburn and Sachs (1990). When an arbitrary inhibitory input was also included to PriN configuration, responses to high frequency components of the input decreases.

4.2 Suggestions for Future Work

The PSTH and ALSR responses presented in this thesis include arbitrary inhibitory inputs. Only bushy cell microcircuit model receives inhibition coming from bottom layers. Therefore PSTH and ALSR codes should be updated to include whole microcircuit model instead of just receiving excitatory ANF inputs and arbitrary inhibitory inputs. The network implementation to PSTH and ALSR results could not presented in this thesis due to time constraints. To create PSTH plots, 500 iterations are used.

ALSR plots use a whole range of CF of ANFs that receives a range of inputs with different frequencies and SPL levels. Therefore, simulations to create these plots need a huge amount of time and computational power. One possible solution is parallelizing the code and using SHARCNET system for submitting jobs with different parameter sets. This will allow us to explore the effects of different configurations of inhibitory inputs on microcircuit responses. When the parallelization achieved, the microcircuit structures will be implemented in the ALSR code. In this thesis, only bushy cell microcircuit responses are inspected to be able to have a comparison with results presented in Manis and Campagnola (2018). The code will be expanded to investigate the tone and vowel responses of TS microcircuits.

One of the powerful aspect of Bruce *et al.* (2018) AN model is to be able to succesfully capture IHC and OHC impairments. In this thesis, only non-imparied ANF inputs are used. After microcircuit structures are implemented and tested in various ways, AN impairment's effect on the firing patterns of primary cell types of the VCN can be explored.

Another future direction for this work will be exploring the responses of TS and bushy cell microcircuits to speech stimuli and compare it with results presented in Delgutte (1997); Delgutte *et al.* (1998).

Our main reason to create microcircuits of the VCN is to implement these models in the phsyiological based speech intelligibitily metrics.

Appendix

```
% main_ODE_v2.m

function [d_out] = main_ODE_v2(t,init_cond)

global I_A
global I_lt
global I_ht
global I_h
global I_lk
global I_na
global type
global response_type
global I_ext_val
global g_e
global freq_e
global freq
global start_epsc
global spike_train
global step_size
global step_size_syn
global epsp_const
global g_syn_exct
global g_syn_inh
global ext_stim_time
global step_intrp
global input_level
global input_onset
global input_length


if strcmp(type,'sgc')

    %type sgc
    C_m = 12;
    g_na = 350;
    g_ht = 58;
    g_lt = 80;
```

```
38      g_A = 0;
39      g_h = 3;
40      g_lk = 2;
41      weight = 2;
42      V_K = -84;
43      V_na = 50;
44      V_h = -41;
45      V_lk = -65;
46
47
48  elseif strcmp(type,'bs2')
49      %bushy-II
50      C_m = 26;
51      g_na = 1000;
52      g_ht = 58;
53      g_lt = 80;
54      g_A = 0;
55      g_h = 30;
56      g_lk = 2;
57      %weight = 0.027;
58      weight_exct = 44.50;
59      weight_inh = 44.50;
60      %weight = 30;
61      V_K = -84;
62      V_na = 50;
63      V_h = -43;
64      V_lk = -65;
65
66  elseif strcmp(type,'bs21')
67      % bushy-II-I
68      C_m = 26;
69      g_na = 1000;
70      g_ht = 58;
71      g_lt = 14;
72      g_A = 0;
73      g_h = 30;
74      g_lk = 2;
75      weight = 0.027;
76      V_K = -84;
77      V_na = 50;
78      V_h = -43;
79      V_lk = -65;
80
81  elseif strcmp(type,'bs12')
82      % bushy-I-II
83      C_m = 26;
84      g_na = 1000;
```

```
85      g_ht = 150;
86      g_lt = 20;
87      g_A = 0;
88      g_h = 2;
89      g_lk = 2;
90      weight = 0.027;
91      V_K = -84;
92      V_na = 50;
93      V_h = -43;
94      V_lk = -65;
95
96  elseif strcmp(type,'ts')
97      % t stellate
98      C_m = 25;
99      g_na = 3000;
100     g_ht = 500;
101     g_lt = 0;
102     g_A = 0;
103     g_h = 18;
104     g_lk = 8;
105     %weight = 0.006;
106     %weight = 5.85;
107     weight = 5;
108     V_K = -84;
109     V_na = 50;
110     V_h = -43;
111     V_lk = -65;
112
113
114 elseif strcmp(type,'tv')
115     % tuberculoventral
116     C_m = 35;
117     g_na = 5800;
118     g_ht = 400;
119     g_lt = 0;
120     g_A = 65;
121     g_h = 2.5;
122     g_lk = 4.5;
123     %weight = 0.0029;
124     weight_exct = 3.5;
125     weight_inh = 3.5;
126     V_K = -81.5;
127     V_na = 50;
128     V_h = -43;
129     V_lk = -72;
130
131
```

```
elseif strcmp(type,'ds')
    %d stellate
    C_m = 12;
    g_na = 1000;
    g_ht = 150;
    g_lt = 20;
    g_A = 0;
    g_h = 2;
    g_lk = 2;
    %weight = 0.00064;
    weight_exct = 0.75;
    weight_inh = 0.75;
    V_K = -70;
    V_na = 55;
    V_h = -43;
    V_lk = -65;



elseif strcmp(type,'type1c')

    %type I-c
    C_m = 12;
    g_na = 1000;
    g_ht = 150;
    g_lt = 0;
    g_A = 0;
    g_h = 0.5;
    g_lk = 2;
    weight_exct = 11;
    weight_inh = 11;
    V_K = -70;
    V_na = 55;
    V_h = -43;
    V_lk = -65;

elseif strcmp(type,'type2')
    %type II
    C_m = 12;
    g_na = 1000;
    g_ht = 150;
    g_lt = 200;
    g_A = 0;
    g_h = 20;
    g_lk = 2;
    weight_exct = 34;
    weight_inh = 34;
```

```
179      V_K = -70;
180      V_na = 55;
181      V_h = -43;
182      V_lk = -65;
183
184  elseif strcmp(type,'type12')
185      C_m = 12;
186      g_na = 1000;
187      g_ht = 150;
188      g_lt = 20;
189      g_A = 0;
190      g_h = 2;
191      g_lk = 2;
192      weight_exct = 15;
193      weight_inh = 15;
194      V_K = -70;
195      V_na = 55;
196      V_h = -43;
197      V_lk = -65;
198
199
200  elseif strcmp(type,'type1t')
201      C_m = 12;
202      g_na = 1000;
203      g_ht = 80;
204      g_lt = 0;
205      g_A = 65;
206      g_h = 0.5;
207      g_lk = 2;
208      weight_exct = 12;
209      weight_inh = 12;
210      V_K = -70;
211      V_na = 55;
212      V_h = -43;
213      V_lk = -65;
214
215  end
216
217
218  d_out = zeros(11,1);    % a column vector
219
220  V = init_cond(1);
221  a = init_cond(2);
222  b = init_cond(3);
223  c = init_cond(4);
224  w = init_cond(5);
225  z = init_cond(6);
```

```
226 n = init_cond(7);
227 p = init_cond(8);
228 m = init_cond(9);
229 h = init_cond(10);
230 r = init_cond(11);
231
232 % fast transient K+ current
233 tao_a = 100*(7*exp((V+60)/14) + 29*exp(-(V+60)/24))^(-1) + 0.1;
234 tao_b = 1000*(14*exp((V+60)/27) + 29*exp(-(V+60)/24))^(-1) + 1;
235 tao_c = 90*(1 + exp(-(V+66)/17))^(-1) + 10;
236
237 a_inf = (1 + exp(-(V+31)/6))^(-1/4);
238 b_inf = (1 + exp((V+66)/7))^(-1/2);
239 c_inf = b_inf;
240
241 da = (a_inf - a)/tao_a;
242 db = (b_inf - b)/tao_b;
243 dc = (c_inf - c)/tao_c;
244
245
246 % low threshold K+ current
247 w_inf = (1 + exp(-(V+48)/6))^(-1/4);
248 zeta = 0.5;
249 z_inf = (1-zeta) * ((1 + exp((V+71)/10))^(-1)) + zeta;
250
251 tao_w = 100*(6*exp((V+60)/6) + 16*exp(-(V+60)/45))^(-1) + 1.5;
252 tao_z = 1000*(exp((V+60)/20) + exp(-(V+60)/8))^(-1) + 50;
253
254 dw = (w_inf - w)/tao_w;
255 dz = (z_inf - z)/tao_z;
256
257
258 % high threshold K+ current
259 sgm = 0.85;
260 n_inf = (1 + exp(-(V+15)/5))^(-1/2);
261 p_inf = (1 + exp(-(V+23)/6))^(-1);
262
263 tao_n = 100*(11*exp((V+60)/24) + 21*exp(-(V+60)/23))^(-1) + 0.7;
264 tao_p = 100*(4*exp((V+60)/32) + 5*exp(-(V+60)/22))^(-1) + 5;
265
266 dn = (n_inf - n)/tao_n;
267 dp = (p_inf - p)/tao_p;
268
269
270 % Fast Na+ Current
271 m_inf = (1 + exp(-(V+38)/7))^(-1);
272 h_inf = (1 + exp((V+65)/6))^(-1) ;
```

```
273
274 tao_m = 10*(5*exp((V+60)/18) + 36*exp(-(V+60)/25))^(-1) + 0.04;
275 tao_h = 100*(7*exp((V+60)/11) + 10*exp(-(V+60)/25))^(-1) + 0.6;
276
277 dm = (m_inf - m)/tao_m;
278 dh = (h_inf - h)/tao_h;
279
280 % Hyperpolarization activated cation current
281 r_inf = (1 + exp((V+76)/7))^(-1);
282 tao_r = (10^5)*(237*exp((V+60)/12) + 17*exp(-(V+60)/14))^(-1) + ↩
      25;
283 dr = (r_inf - r)/tao_r;
284
285 I_A  = g_A * (a^4) * b * c *(V-V_K) ;
286 I_lt = g_lt * (w^4) * z * (V-V_K);
287 I_ht = g_ht * ((sgm * (n^2)) + (1-sgm)*p )* (V-V_K);
288 I_na = g_na * (m^3) * h * (V-V_na);
289 I_h  = g_h * r * (V-V_h) ;
290 I_lk = g_lk * (V-V_lk);
291
292 if strcmp(response_type,'epsp')
293
294     g_e = epsp_const*g_e; % comment this part when you're ↩
          simulating current clamp responses
295     freq = 1000/freq_e;
296     tao_e = 0.4;
297
298     I_ext = 0;
299     I_e = 0;
300     if t > start_epsc && t<(start_epsc+200)
301         I_e = g_e * ((mod(t,freq))/tao_e) .* exp(1-((mod(t,freq))/↩
              tao_e))*(V-V_exct);
302         %I_e = g_e * ((t-start_epsc)/tao_e) .* exp(1-((t-↩
              start_epsc)/tao_e))*(V-V_E);
303
304         %I_e_n = g_e * ((t-5)/tao_e) .* exp(1-((t-5)/tao_e))*(V-↩
              V_E);
305         %I_e = I_e + I_e_n;
306
307     else
308         I_e = 0;
309     end
310
311     %     if start_epsc == 5;
312     %        I_e = g_e * ((t-start_epsc)/tao_e) .* exp(1-((t-↩
          start_epsc)/tao_e))*(V-V_E);
```

```
313     %         I_e_n = g_e * ((t-start_epsc+1)/tao_e) .* exp(1-((t-start_epsc+1)/tao_e))*(V-V_E);
314     %         I_e = I_e + I_e_n;
315     %     end
316
317 elseif strcmp(response_type,'synaptic')
318
319     if strcmp(input_level,'sub')
320         g_reg = 0.5;
321     else
322         g_reg = 3;
323     end
324
325     V_exct = 0; %0
326     V_inh = -75; %potassium equilib
327     I_ext = 0;
328     I_e_exct = g_reg * weight_exct * g_syn_exct(floor(t/step_size_syn)+1) * (V-V_exct);
329     I_e_inh = g_reg * weight_inh * g_syn_inh(floor(t/step_size_syn)+1) * (V-V_inh);
330     I_e = I_e_exct + I_e_inh;
331
332
333 elseif strcmp(response_type,'synaptic_test')
334
335     V_exct = 0; %0
336     %V_inh = -75; %potassium equilib
337     I_ext = 0;
338     I_e_exct = g_syn_exct(floor(t/step_size_syn)+1);% * (V-V_exct);
339     %I_e_inh = weight * g_syn_inh(floor(t/step_intrp)+1) * (V-V_inh);
340     I_e = -I_e_exct;
341
342
343 elseif strcmp(response_type,'synaptic_exct')
344
345     if strcmp(input_level,'sub')
346         g_reg = 0.5;
347     else
348         g_reg = 3;
349     end
350
351     V_exct = 0; %0
352     V_inh = -75; %potassium equilib
353     I_ext = 0;
```

```
354      I_e_exct = g_reg * weight_exct * g_syn_exct(floor(t/↩
             step_size_syn)+1) * (V-V_exct);
355      I_e = I_e_exct;
356
357  elseif strcmp(response_type,'ext')
358
359      I_ext = 0;
360      if (t> input_onset) && (t<input_length + input_onset)
361          I_ext = I_ext_val;
362      else
363          I_ext = 0;
364      end
365      I_e = 0;
366
367
368
369  elseif strcmp(response_type,'spike')
370
371
372      I_ext = 0;
373      I_e = spike_train(floor(t/step_size) + 1);%-init_cond(1);
374
375  end
376
377
378
379  d_out(1) = (1/C_m) * (-I_A - I_lt - I_ht - I_na - I_h - I_lk - I_e↩
         + I_ext);
380  d_out(2) = da;
381  d_out(3) = db;
382  d_out(4) = dc;
383  d_out(5) = dw;
384  d_out(6) = dz;
385  d_out(7) = dn;
386  d_out(8) = dp;
387  d_out(9) = dm;
388  d_out(10) = dh;
389  d_out(11) = dr;
390  % d_out(12) = I_A;
391  % d_out(13) = I_lt;
392  % d_out(14) = I_ht;
393  % d_out(15) = I_h;
394  end
```

```
1  % exp2syn.m
2
```

```
3  function [syn_out] = exp2syn(syn_in,connection_type)
4  % synapse model
5  global step_size_syn
6  t_syn = 0:step_size_syn:100-step_size_syn;
7
8  if strcmp(connection_type, 'exct')
9  tao_exc = 0.4; %in msec
10 g_exc = exp(-t_syn/tao_exc);
11 syn_out = filter(g_exc,1,syn_in);
12
13 elseif strcmp(connection_type, 'inh')
14 tao_inh1 = 0.4;
15 tao_inh2 = 2.5;
16
17 t_norm = log(tao_inh2/tao_inh1)*(tao_inh1*tao_inh2)/(tao_inh2-↩
      tao_inh1);
18 norm_const = 1/(exp(-t_norm/tao_inh2)-exp(-t_norm/tao_inh1));
19 g_inh = norm_const * (exp(-t_syn/tao_inh2) - exp(-t_syn/tao_inh1))↩
      ;
20 syn_out = filter(g_inh,1,syn_in);
21 end
22
23 end
```

```
1  % resting_state_values.m
2
3  clear all,
4  global start_epsc
5  global type
6  global I_ext_val
7  global response_type
8  global step_size
9  global ext_stim_time
10
11 dbstop if error % if there is an error, this stops the function, ↩
      goes into debug mode
12 % and show you the parameters
13
14 step_size = 0.005; % or 2500/Fs if you want to use ANModel and ↩
      this together
15 response_type = 'ext'; % response type; epsp-->synaptic, ext-->↩
      external,
16 %                 neural --> from other types,
17 %                 spike--> spike train
18
19 I_ext_val  = 0; % external current input value (in pA)
```

```
20
21 type = 'ds'; % cell type
22 % load(['rest_val_' type]);
23 t = 0:step_size:5000-step_size;
24 start_epsc = 30;
25 ext_stim_time = 200;
26 %init_cond = rest_val;
27 init_cond = [-63.9 0.10 0.2 0.3 0.2 0.1 0.2 0.2 0.4 0.2 0.2] % ↩
      some dummy values these will converge
28
29 %options = odeset('MaxStep',0.005);
30 my_ODE = @main_ODE_v2;
31 [t_out,d_out] = ode45(my_ODE,t,init_cond);
32
33
34 plot(d_out(:,11),'r'),title(type) ,%ylim([-75 0])
35
36 rest_val = d_out(length(d_out),:);
37 save_name = [ 'rest_val_' type];
38 save ( save_name , 'rest_val')
```

```
1  % response_map_bushy.m
2
3  clear all, %close all
4
5  global type
6  global response_type
7  global step_size
8  global step_size_syn
9  global sim_time
10 global g_syn_exct
11 global g_syn_inh
12
13 load response_map_ds_thesis_3.mat ;
14 ds_out = new_cell_out_psth_cell;
15 load response_map_type1c_0_03_reduction.mat ;
16 tv_out = new_cell_out_psth_cell;
17
18 %
19 % load response_map_ds_last_try
20 % ds_out = new_cell_out_psth_cell;
21 % tv_out = new_cell_out_psth_cell;
22
23 %% setting up simulation environment
24 Fs = 1e5;
25 sim_time = 0.15;
```

```
step_size = 1/Fs;
step_size_syn = step_size/1e-3;
t_sim = 0:step_size_syn:(sim_time*1e3)-step_size_syn;
threshold = -20;
psth_try = 5;
seed_number = 1000;
response_type = 'synaptic'; % response type; epsp-->synaptic, ext-->external,
%                neural --> from other types,
%                spike--> spike train
input_level = 'supra'

pip_sweep_start = 4000; % the characteristic freq of the postsynaptic cell
pip_sweep_end = 32000;
pip_sweep_step = 1/8; % in octaves
pip_freq_range(1) = pip_sweep_start;
k = 2;
while pip_freq_range(k-1) < pip_sweep_end
    pip_freq_range(k) = pip_freq_range(k-1)*(2^(pip_sweep_step));
    k = k+1;
end
pip_count = length(pip_freq_range);
CF_post_syn = 16000;

fiber_type = [1]; % which type of fibers should be included
fiber_type_count = length(fiber_type);
AN_input_count = 3;
AN_input_sd = 0.05;
DS_input_count = 7;
DS_input_sd = 0.208;
TV_input_count = 6;
TV_input_sd = 0.069;

%entering AN model parameters
cohc  = 1.0;    % normal ohc function
cihc  = 1.0;    % normal ihc function
species = 1;    % 1 for cat (2 for human with Shera et al. tuning; 3 for human with Glasberg & Moore tuning)
noiseType = 1;  % 1 for variable fGn (0 for fixed fGn)
implnt = 0;     % "0" for approximate or "1" for actual implementation of the power-law functions in the Synapse
% stimulus parameters
Fs = 100e3;  % sampling rate in Hz (must be 100, 200 or 500 kHz)
T  = 50e-3;  % stimulus duration in seconds
rt = 2.5e-3; % rise/fall time in seconds
numsponts_healthy = [AN_input_count AN_input_count AN_input_count
```

```
    ];
69
70 % PSTH parameters
71 nrep = 1;                % number of stimulus repetitions (e.g., ↩
       50);
72 psthbinwidth = 0.5e-3; % binwidth in seconds;
73
74 t = 0:step_size:T-step_size; % time vector
75 mxpts = length(t);
76 irpts = rt*Fs;
77 ondelay = 50e-3;
78 %ondelay = AN_counter*1e-3;
79 onbin = round(ondelay*Fs);
80
81 [sponts,tabss,trels] = generateANpopulation(pip_count,↩
       numsponts_healthy);
82 sponts_lower_limit = [ones(1,AN_input_count)*0.1, ones(1,↩
       AN_input_count)*1,...
83     ones(1,AN_input_count)*10];
84 %disp('Generating population of AN fibers, saved in ANpopulation.↩
       mat')
85 numsponts = round([1 1 1].*numsponts_healthy); % Healthy AN
86
87 db_val_start = 20;
88 db_val_step = 5;
89 db_val_end = 100;
90
91 % creating the range of weight vectors
92 weight_range = 0:pip_count-1;
93
94 % arranging the ODE initial values
95 type = 'bs2'; % cell type
96 load(['rest_val_' type]);
97 init_cond = rest_val;
98 my_ODE = @main_ODE_v2;
99
100 [~, CF_close_index] = min(abs(pip_freq_range - CF_post_syn));
101 seed_number = seed_number + CF_close_index;
102
103 weights_AN = lognpdf(weight_range,log(CF_close_index),AN_input_sd)↩
       ; % dummy mean and standart dev values
104 [s_AN] = RandStream.create('mlfg6331_64','Seed',seed_number); %for↩
        reproductibility
105 AN_freq_chosen = datasample(s_AN,1:pip_count,AN_input_count,'↩
       Replace',false,...
106     'Weights',weights_AN); % draw unique samples according to ↩
          vaules
```

```
% defined in the probability matrix of weights
AN_freq_chosen = sort(AN_freq_chosen);

[~, DS_close_index] = min(abs(pip_freq_range - CF_post_syn));
weights_DS = lognpdf(weight_range,log(DS_close_index),DS_input_sd); % dummy mean and standart dev values
[s_DS] = RandStream.create('mlfg6331_64','Seed',seed_number); %for reproductibility
DS_freq_chosen_indx = datasample(s_DS,1:pip_count,DS_input_count,'Replace',false,...
    'Weights',weights_DS); % draw unique samples according to vaules
% defined in the probability matrix of weights
DS_freq_chosen_indx = sort(DS_freq_chosen_indx);
% for jk = 1:DS_input_count
%     DS_comp = pip_freq_range(DS_freq_chosen_indx(jk));
%     [~,DS_comp_out] = min(abs(pip_freq_range - DS_comp));
%     DS_freq_chosen(jk) = DS_comp_out;
% end

[~, TV_close_index] = min(abs(pip_freq_range - CF_post_syn));
weights_TV = lognpdf(weight_range,log(TV_close_index),TV_input_sd); % dummy mean and standart dev values
[s_TV] = RandStream.create('mlfg6331_64','Seed',seed_number); %for reproductibility
TV_freq_chosen_indx = datasample(s_TV,1:pip_count,TV_input_count,'Replace',false,...
    'Weights',weights_TV); % draw unique samples according to vaules
% defined in the probability matrix of weights
TV_freq_chosen_indx = sort(TV_freq_chosen_indx);
% for jk = 1:TV_input_count
%     TV_comp = pip_freq_range(TV_freq_chosen_indx(jk));
%     [~,TV_comp_out] = min(abs(pip_freq_range - TV_comp));
%     TV_freq_chosen(jk) = TV_comp_out;
% end

a = 1;
for pip_indx = 1:length(pip_freq_range)
    %[~, pip_close_index] = min(abs(freq_range - pip_freq_range(pip_indx)));
    %pip_freq = freq_range(pip_close_index);
    pip_freq = pip_freq_range(pip_indx);
    for db_val = db_val_start:db_val_step:db_val_end
        for m = 1:psth_try
            stimdb = db_val; % stimulus intensity in dB SPL
            spike_train_sum_AN = zeros(1,sim_time*Fs);
```

```
145             % collecting the input data and add the spike trains
146             % together
147             for fiber_type_count = 1:length(fiber_type);
148                 for AN_counter = 1:AN_input_count
149                     F0 = pip_freq;     % stimulus frequency in Hz
150                     CF = pip_freq_range(AN_freq_chosen(AN_counter)↩
                            );
151                     pin = zeros(1,onbin+mxpts);
152                     pin(onbin+1:onbin+mxpts) = sqrt(2)*20e-6*10^(↩
                            stimdb/20)*sin(2*pi*F0*t); % unramped ↩
                            stimulus
153                     pin(onbin+1:onbin+irpts)= pin(onbin+1:onbin+↩
                            irpts).*(0:(irpts-1))/irpts;
154                     pin(onbin+(mxpts-irpts):onbin+mxpts)=pin(onbin↩
                            +(mxpts-irpts):onbin+mxpts).*(irpts:-1:0)/↩
                            irpts;
155
156                     sponts_concat = [sponts.LS(pip_indx,1:↩
                            numsponts(1)) sponts.MS(pip_indx,1:↩
                            numsponts(2)) sponts.HS(pip_indx,1:↩
                            numsponts(3))];
157                     tabss_concat = [tabss.LS(pip_indx,1:numsponts↩
                            (1)) tabss.MS(pip_indx,1:numsponts(2)) ↩
                            tabss.HS(pip_indx,1:numsponts(3))];
158                     trels_concat = [trels.LS(pip_indx,1:numsponts↩
                            (1)) trels.MS(pip_indx,1:numsponts(2)) ↩
                            trels.HS(pip_indx,1:numsponts(3))];
159
160                     %spont = sponts_concat((fiber_type_count-1)*↩
                            AN_input_count + AN_counter);
161                     spont = sponts_lower_limit((fiber_type(↩
                            fiber_type_count)-1)*AN_input_count + ↩
                            AN_counter);
162                     tabs = tabss_concat((fiber_type_count-1)*↩
                            AN_input_count + AN_counter);
163                     trel = trels_concat((fiber_type_count-1)*↩
                            AN_input_count + AN_counter);
164
165                     vihc = model_IHC_BEZ2018(pin,CF,nrep,1/Fs,↩
                            sim_time,cohc,cihc,species);
166                     psth = model_Synapse_BEZ2018(vihc,CF,nrep,1/Fs↩
                            ,noiseType,implnt,spont,tabs,trel);
167
168                     spike_train(AN_counter,:) = psth;
169                     spike_train_raster(AN_input_count*(↩
                            fiber_type_count-1) + AN_counter,:) = psth;
170
```

```
171                 end
172
173                 spike_train_sum_AN = sum(spike_train,1);
174
175                 cell_out_fiber(fiber_type_count,:) = ↩
                       spike_train_sum_AN;
176             end
177
178             cell_out_AN(:,m) = sum(cell_out_fiber,1);
179
180             g_syn_exct = exp2syn(cell_out_AN(:,m),'exct');
181
182             for DS_counter = 1:DS_input_count
183                 DS_spike_times = ds_out{DS_freq_chosen_indx(↩
                       DS_counter),...
184                     ((db_val - db_val_start)/db_val_step)+1,m};
185                 DS_spike_train = zeros(length(t_sim),1);
186                 DS_spike_train(DS_spike_times) = 1;
187                 DS_spike_out(DS_counter,:) = DS_spike_train;
188             end
189
190             cell_out_DS(:,m) = sum(DS_spike_out,1);
191
192             for TV_counter = 1:TV_input_count
193                 TV_spike_times = ds_out{TV_freq_chosen_indx(↩
                       TV_counter),...
194                     ((db_val - db_val_start)/db_val_step)+1,m};
195                 TV_spike_train = zeros(length(t_sim),1);
196                 TV_spike_train(TV_spike_times) = 1;
197                 TV_spike_out(TV_counter,:) = TV_spike_train;
198             end
199
200             cell_out_TV(:,m) = sum(TV_spike_out,1);
201
202             g_syn_inh = exp2syn((cell_out_TV(:,m) + cell_out_DS(:,↩
                   m))*0.25,'inh');
203             [t_out,d_out] = ode45(my_ODE,t_sim,init_cond);
204
205             [~,l] = findpeaks(d_out(:,1),'MinPeakHeight',threshold↩
                   );
206             %             new_cell_out = zeros(1,length(d_out(:,1)↩
                   ));
207             %             new_cell_out(l) = 1;
208             %             new_cell_out = find(new_cell_out==1);
209
210             new_cell_out_psth_cell{a,((db_val-db_val_start)/↩
                   db_val_step +1),m} = l; %new_cell_out;
```

```
211
212 %             figure,
213 %
214 %             subplot(3,1,1), plot(d_out(:,1)),title('bushy cell membrane voltage'),ylabel('mV');
215 %              subplot(3,1,2), plot(g_syn_exct),title('excitatory synaptic conductance change'),ylabel('nS');
216 %             subplot(3,1,3), plot(g_syn_inh),title('inhibitory synaptic conductance change'),ylabel('nS');
217 %
218 %
219 %             figure,
220 %
221 %             subplot(3,1,1), plot(d_out(:,1)),title('bushy cell membrane voltage'),ylabel('mV');
222 %             subplot(3,1,2), plot(cell_out_AN(:,m)),title('excitatory synaptic conductance change'),ylabel('nS');
223 %             subplot(3,1,3), plot(g_syn_inh),title('inhibitory synaptic conductance change'),ylabel('nS');
224 %
225 %
226             disp(['trying ' num2str(m) ' psth for ' num2str(db_val) ' db for the pip freq of ' num2str(pip_freq)])
227         end
228
229     end
230     %end
231     a = a+1;
232 end
233
234 % response_map = zeros((pip_sweep_end-pip_sweep_start-pip_sweep_step)/pip_sweep_step + 1,...
235 %     (db_val_end-db_val_start)/db_val_step + 1);
236 response_map = zeros(length(pip_freq_range),(db_val_end-db_val_start)/db_val_step + 1);
237 for db_resp = 1:((db_val_end-db_val_start)/db_val_step + 1)
238     %for pip_resp = 1:((pip_sweep_end-pip_sweep_start-pip_sweep_step)/pip_sweep_step + 1)
239     for pip_resp = 1:length(pip_freq_range)
240         for s_AN = 1:psth_try
241             response_map(pip_resp,db_resp) = length(new_cell_out_psth_cell{pip_resp,db_resp,s_AN})+ response_map(pip_resp,db_resp);
242         end
243         % response_map(pip_resp,db_resp) = response_map(pip_resp,db_resp);%/psth_try;
244     end
```

```
end

response_map = response_map./max(max(response_map));
response_map = flipud(response_map');

figure,
ax = gca;
imagesc(response_map),colormap(flipud(gray))
set(gca, 'XScale')
ax.XTick = [1 9 17 25]
ax.XTickLabel = {4000 8000 16000 32000}
ax.YTick = [1 5 9 13 17]
ax.YTickLabel = {100 80 60 40 20}
xlabel('Tone frequency (Hz)')
ylabel('Tone SPL (dB)')
```

```
% an_boxplot_ALSR.m

global type
global response_type
global step_size
global sim_time
global g_syn_exct
global g_syn_inh
global step_size_syn

threshold = -20;
syn_response = 'exct';
response_type = 'synaptic_exct'; % response type; epsp-->synaptic,ext-->external,
%                neural --> from other types,
%                spike--> spike train
input_level = 'supra'; % sub --> subthreshold, supra --> suprathreshold
type = 'bs2'; % cell type
load(['rest_val_' type]);
init_cond = rest_val;
my_ODE = @main_ODE_v2;

alsr_octs = 1; % number of octaves around CF over which the ALSR is computed

h1 = figure;
h3 = fill([0.1 10 10 0.1],[0.1*2^(1/2) 10*2^(1/2) 10/2^(1/2) 0.1/2^(1/2)],0.9*ones(1,3));
set(h3,'edgecolor','none')
```

```
27 set(gca,'xscale','log','yscale','log','fontsize',14)
28 xlabel('CF (kHz)','fontsize',14)
29 ylabel('Frequency (kHz)','fontsize',14)
30 axis([0.1 10 0.095 4.5])
31 set(gca,'xtick',[0.1 1.0 10])
32 % set(gca,'xticklabel','0.1|1.0|10')
33 set(gca,'xticklabel',{'0.1','1.0','10'})
34 set(gca,'ytick',[0.1 0.4 1.0 4.0])
35 % set(gca,'yticklabel','0.1|0.4|1.0|4.0')
36 set(gca,'yticklabel',{'0.1','0.4','1.0','4.0'})
37 hold on
38 plot([0.5 0.5],[0.095 4.5],'k--')
39 plot([1.7 1.7],[0.095 4.5],'k--')
40 plot([2.5 2.5],[0.095 4.5],'k--')
41 plot([0.1 10],[0.5 0.5],'k--')
42 plot([0.1 10],[1.7 1.7],'k--')
43 plot([0.1 10],[2.5 2.5],'k--')
44 units=get(h1,'units');
45 set(h1,'units',get(h1,'PaperUnits'));
46 set(h1,'Position',get(h1,'PaperPosition'));
47 set(h1,'Units',units)
48 set(h1,'Position',get(h1,'Position')-[-250 0 0 0])
49
50 % model parameters
51 numcfs = 41;
52 cfs = logspace(log10(125),log10(5e3),numcfs);
53 numcfs_bushy = 39;
54 AN_input_count = 3;
55 cohcs  = ones(1,numcfs);  % normal ohc function
56 cihcs  = ones(1,numcfs);  % normal ihc function
57
58 numsponts_healthy = [0 0 1]; % Number of low-spont, medium-spont, ↩
      and high-spont fibers at each CF in a healthy AN
59
60 % if exist('ANpopulation.mat','file')
61 %     load('ANpopulation.mat');
62 %     disp('Loading existing population of AN fibers saved in ↩
      ANpopulation.mat')
63 %     if (size(sponts.LS,2)<numsponts_healthy(1))||(size(sponts.MS↩
      ,2)<numsponts_healthy(2))||(size(sponts.HS,2)<numsponts_healthy↩
      (3))||(size(sponts.HS,1)<numcfs||~exist('tabss','var'))
64 %         disp('Saved population of AN fibers in ANpopulation.mat ↩
      is too small - generating a new population');
65 %         [sponts,tabss,trels] = generateANpopulation(numcfs,↩
      numsponts_healthy);
66 %     end
67 % else
```

```
68 [sponts,tabss,trels] = generateANpopulation(numcfs,↩
      numsponts_healthy);
69 %     disp('Generating population of AN fibers, saved in ↩
      ANpopulation.mat')
70 % end
71 sponts_lower_limit = ones(1,numcfs);
72 species = 1;     % 1 for cat (2 for human)
73 noiseType = 1;  % 0 for fixed fGn (1 for variable fGn)
74 implnt = 0;     % "0" for approximate or "1" for actual ↩
      implementation of the power-law functions in the Synapse
75
76 % stimulus parameters
77 Fs = 100e3;  % sampling rate = 100 kHz - THIS SAMPLING RATE IS ↩
      ESSENTIAL FOR THE MODEL
78 rt = 0.01;   % rise time = 10 ms
79 stimdb = 55; % stimulus intensity in dB SPL; note - vowel portion ↩
      of besh is ~3 dB lower
80 % stimdb = 60; % stimulus intensity in dB SPL; note - vowel ↩
      portion of besh is ~3 dB lower
81
82 % PSTH parameters
83 nrep = 1;             % number of stimulus repetitions = 50;
84 psthbinwidth = 0.1e-3; % binwidth = 0.1 ms;
85 psthbins = round(psthbinwidth*Fs);  % number of psth100k bins per ↩
      psth bin
86 psth_try = 50;
87 % load eh_hrtf_calib_100k_0dB;
88 % stim = resample(eh_hrtf_calib_100k_0dB,Fs,Fs_stim);
89 % stim = stim(1:round(0.1*Fs));
90
91 load besh100k_hrtf_calib
92 stim = besh100k_hrtf_calib;
93
94 T = round(length(stim))/Fs;
95
96 simdur = ceil(T*2/psthbinwidth)*psthbinwidth;
97 step_size = 1/Fs;
98 step_size_syn = step_size/1e-3;
99 t = 0:1/Fs:T-1/Fs; % time vector
100 t_sim = 0:step_size_syn:(simdur*1e3)-step_size_syn;
101
102 pin = 10^(stimdb/20)*stim; % unramped stimulus
103
104 pin = pin(:).';
105
106 % Ramp stimulus on and off
107 % mxpts = length(pin);
```

```
% irpts = round(rt*Fs);
%
% pin(1:irpts) = pin(1:irpts).*(0:(irpts-1))/irpts;
% pin((mxpts-irpts):mxpts) = pin((mxpts-irpts):mxpts).*(irpts:-1:0)/irpts;

h = waitbar(0,'Computing...');
set(h,'name','anboxplot - 0%')

maxcf = find(cfs<1/psthbinwidth/2,1,'last');
%g_syn_inh = zeros(1,length(t_sim));
numsponts = round([1 1 1].*numsponts_healthy); % Healthy AN

% comment out this part if just excitatory input are going to be presented
syn_in_inh = zeros(1,length(t_sim));
syn_in_inh([(Fs/1e5)*randi(length(syn_in_inh)/(Fs/1e5),1,20)]) = 1;
g_syn_inh = exp2syn(syn_in_inh,'inh');


for cflp=1:numcfs_bushy
    for spontlp = 1:sum(numsponts)
        disp(['cflp = ' int2str(cflp) '/' int2str(maxcf) '; spontlp = ' int2str(spontlp) '/' int2str(sum(numsponts))])

        for m = 1:psth_try

            for n = 0:AN_input_count-1
                cf=cfs(cflp +n);
                cohc=cohcs(cflp +n);
                cihc=cihcs(cflp +n);

                %     disp(['CF = ' num2str(cf) ' (' int2str(cflp) '/' int2str(maxcf) ')'])

                %     numsponts = round([0.5 0.5 0.5].*numsponts_healthy); % 50% fiber loss of all types
                %     numsponts = round([0 1 1].*numsponts_healthy); % Loss of all LS fibers
                %     numsponts = round([cihc 1 cihc].*numsponts_healthy); % loss of LS and HS fibers proportional to IHC impairment

                sponts_concat = [sponts.LS(cflp +n,1:numsponts(1))
```

```
                sponts.MS(cflp +n,1:numsponts(2)) sponts.HS(↩
                cflp +n,1:numsponts(3))];
144             tabss_concat = [tabss.LS(cflp +n,1:numsponts(1)) ↩
                tabss.MS(cflp +n,1:numsponts(2)) tabss.HS(cflp ↩
                +n,1:numsponts(3))];
145             trels_concat = [trels.LS(cflp +n,1:numsponts(1)) ↩
                trels.MS(cflp +n,1:numsponts(2)) trels.HS(cflp ↩
                +n,1:numsponts(3))];
146
147
148             spont = sponts_concat(spontlp);
149             tabs = tabss_concat(spontlp);
150             trel = trels_concat(spontlp);
151             vihc = model_IHC_BEZ2018(pin,cf,nrep,1/Fs,simdur,↩
                cohc,cihc,species);
152
153
154             psth100k(n+1,:) = model_Synapse_BEZ2018(vihc,cf,↩
                nrep,1/Fs,noiseType,implnt,spont,tabs,trel);
155         end
156         psth_100k_sum = sum(psth100k,1);
157
158         psth = zeros(1,length(vihc)/nrep/psthbins);
159
160         % flush the output for the display of the coutput in ↩
            Octave
161         if exist ('OCTAVE_VERSION', 'builtin') ~= 0
162             fflush(stdout);
163         end
164
165
166         g_syn_exct = exp2syn(psth_100k_sum,syn_response);
167
168         [t_out,d_out] = ode45(my_ODE,t_sim,init_cond);
169
170         [~,l] = findpeaks(d_out(:,1),'MinPeakHeight',threshold↩
            );
171         new_cell_out = zeros(1,length(d_out(:,1)));
172         new_cell_out(l) = 1;
173         psth_cell(m,:) = new_cell_out;
174
175         %             figure,
176         %             subplot(4,1,1), plot(psth100k),title('AN ↩
            fiber output');
177         %             subplot(4,1,2), plot(g_syn_exct),title('↩
            Synaptic output');
178         %             subplot(4,1,3), plot(d_out(:,1)),title([↩
```

```
                type ' cell output']);
179             %             subplot(4,1,4), plot(psth_cell(m,:)), ↩
                title ([type ' cell output spike train'])
180             %
181
182         end
183
184         psth_cell_sum = sum(psth_cell,1);
185         timeout = 0:1/Fs:(length(psth100k)-1)/Fs;
186
187         psthtime = timeout(1:psthbins:end); % time vector for psth
188         pr = sum(reshape(psth_cell_sum,psthbins,length(↩
                psth_cell_sum)/psthbins))/psth_try; % pr of spike in ↩
                each bin
189         psth = psth+pr/psthbinwidth; % psth in units of spikes/s
190
191     end
192
193     psth = psth/sum(numsponts);
194
195     [dummyy, tonset] =min(abs(psthtime-90e-3));
196     [dummyy, toffset]=min(abs(psthtime-170e-3));
197
198     toffset = toffset-1;
199
200     % 80ms Hamming window starting 20ms after stimulus onset
201     p = psth(tonset:toffset);
202     w = hamming(length(p),'periodic')';
203     [MX, f] = fouriercoeffs(w.*p,1/psthbinwidth);
204     ft(cflp,:)=MX/sqrt(sum(w.^2)/length(w));
205
206     f_ind = find(f==100):find(f==100)-1:find(f==4e3);
207
208     % creating the boxplot
209     figure(h1)
210     h2 = loglog(cf/1e3,f(f_ind)/1e3,'ks','markerfacecolor','k');
211     for lp=1:length(h2)
212         if ft(cflp,f_ind(lp))<15
213             set(h2(lp),'marker','none')
214         elseif ft(cflp,f_ind(lp))<30
215             set(h2(lp),'markersize',2)
216         elseif ft(cflp,f_ind(lp))<45
217             set(h2(lp),'markersize',4)
218         elseif ft(cflp,f_ind(lp))<60
219             set(h2(lp),'markersize',6)
220         elseif ft(cflp,f_ind(lp))<75
221             set(h2(lp),'markersize',8)
```

```
222          elseif ft(cflp,f_ind(lp))<90
223              set(h2(lp),'markersize',10)
224          elseif ft(cflp,f_ind(lp))<105
225              set(h2(lp),'markersize',12)
226          elseif ft(cflp,f_ind(lp))<120
227              set(h2(lp),'markersize',14)
228          else
229              set(h2(lp),'markersize',16)
230          end
231      end
232
233      waitbar(cflp/maxcf,h)
234      set(h,'name',['anboxplot - ' num2str(cflp/maxcf*100,'%3.0f') '↩
            %'])
235
236  end
237
238
239  close(h)
240
241  fnums = length(f);
242
243  ALSR = zeros(1,fnums);
244
245
246  for flp = 2:fnums
247
248      cf_low = find(cfs>(f(flp)/2^(alsr_octs/2)),1,'first');
249      cf_high = find(cfs<(f(flp)*2^(alsr_octs/2)),1,'last');
250      ALSR(flp) = mean(ft(cf_low:cf_high,flp));
251
252  end
253
254  % plotting the ALSR
255  figure
256  subplot(2,1,1)
257  loglog(f/1e3,ALSR)
258  xlim([0.1 5])
259  hold on
260  plot([0.5 0.5],ylim,'k--')
261  plot([1.7 1.7],ylim,'k--')
262  plot([2.5 2.5],ylim,'k--')
263  ylabel('ALSR (spikes/s)')
264  title('ALSR at all frequencies')
265  subplot(2,1,2)
266  loglog(f(f_ind)/1e3,ALSR(f_ind))
267  xlim([0.1 5])
```

```
268 hold on
269 plot([0.5 0.5],ylim,'k--')
270 plot([1.7 1.7],ylim,'k--')
271 plot([2.5 2.5],ylim,'k--')
272 ylabel('ALSR (spikes/s)')
273 title('ALSR at vowel harmonics')
274 xlabel('Frequency (kHz)')
275 xlim([0.1 5])
```

Bibliography

Anatomybody-charts (2016). Anatomy body charts. http://anatomybodycharts.us/inner-ear-anatomy/inner-ear-anatomy-2/.

Blackburn, C. C. and Sachs, M. B. (1990). The representations of the steady-state vowel sound/e/in the discharge patterns of cat anteroventral cochlear nucleus neurons. *Journal of neurophysiology*, **63**(5), 1191–1212.

Brawer, J. R., Morest, D. K., and Kane, E. C. (1974). The neuronal architecture of the cochlear nucleus of the cat. *Journal of Comparative Neurology*, **155**(3), 251–299.

Bruce, I. C., Sachs, M. B., and Young, E. D. (2003). An auditory-periphery model of the effects of acoustic trauma on auditory nerve responses. *The Journal of the Acoustical Society of America*, **113**(1), 369–388.

Bruce, I. C., Erfani, Y., and Zilany, M. S. (2018). A phenomenological model of the synapse between the inner hair cell and auditory nerve: Implications of limited neurotransmitter release sites. *Hearing research*, **360**, 40–54.

Campagnola, L. and Manis, P. B. (2014). A map of functional synaptic connectivity in the mouse anteroventral cochlear nucleus. *Journal of Neuroscience*, **34**(6), 2214–2230.

Cant, N. B. and Benson, C. G. (2003). Parallel auditory pathways: projection patterns of the different neuronal populations in the dorsal and ventral cochlear nuclei. *Brain research bulletin*, **60**(5-6), 457–474.

Carnevale, N. T. and Hines, M. L. (2006). *The NEURON book*. Cambridge University Press.

Carney, L. H. (1993). A model for the responses of low-frequency auditory-nerve fibers in cat. *The Journal of the Acoustical Society of America*, **93**(1), 401–417.

Caspary, D., Backoff, P., Finlayson, P., and Palombi, P. (1994). Inhibitory inputs modulate discharge rate within frequency receptive fields of anteroventral cochlear nucleus neurons. *Journal of Neurophysiology*, **72**(5), 2124–2133.

Delgutte, B. (1982). Some correlates of phonetic distinctions at the level of the auditory nerve. *The representation of speech in the peripheral auditory system*, pages 131–149.

Delgutte, B. (1997). Auditory neural processing of speech. *The handbook of phonetic sciences*, pages 507–538.

Delgutte, B., Hammond, B., and Cariani, P. (1998). Neural coding of the temporal envelope of speech: relation to modulation transfer functions. *Psychophysical and physiological advances in hearing*, pages 595–603.

Eager, M. A. (2013). *The Stellate Microcircuit of the Cochlear Nucleus: Design and Optimisation of a Biophysically-realistic Neural Network Model*. Ph.D. thesis, University of Melbourne, Department of Otolaryngology.

Eager, M. A., Grayden, D. B., Burkitt, A. N., and Meffin, H. (2004). A neural circuit model of the ventral cochlear nucleus. In *Proc 10th Aust Int Conf on Speech Science & Technology, SST*, pages 539–544.

Feng, J. J., Kuwada, S., Ostapoff, E.-M., Batra, R., and Morest, D. K. (1994). A physiological and structural study of neuron types in the cochlear nucleus. i. intracellular responses to acoustic stimulation and current injection. *Journal of Comparative Neurology*, **346**(1), 1–18.

Graham, B. P., Wong, A. Y., and Forsythe, I. D. (2001). A computational model of synaptic transmission at the calyx of held. *Neurocomputing*, **38**, 37–42.

Heinz, M. G., Zhang, X., Bruce, I. C., and Carney, L. H. (2001). Auditory nerve model for predicting performance limits of normal and impaired listeners. *Acoustics Research Letters Online*, **2**(3), 91–96.

Koch, C. and Segev, I. (1998). *Methods in neuronal modeling: from ions to networks*. MIT press.

Kuo, S. P., Lu, H.-W., and Trussell, L. O. (2012). Intrinsic and synaptic properties of vertical cells of the mouse dorsal cochlear nucleus. *Journal of neurophysiology*, **108**(4), 1186–1198.

Liberman, M. C. (1978). Auditory-nerve response from cats raised in a low-noise chamber. *The Journal of the Acoustical Society of America*, **63**(2), 442–455.

Manis, P. B. and Campagnola, L. (2018). A biophysical modelling platform of the cochlear nucleus and other auditory circuits: from channels to networks. *Hearing research*, **360**, 76–91.

Nordlie, E., Gewaltig, M.-O., and Plesser, H. E. (2009). Towards reproducible descriptions of neuronal network models. *PLoS computational biology*, **5**(8), e1000456.

Oertel, D. (1983). Synaptic responses and electrical properties of cells in brain slices of the mouse anteroventral cochlear nucleus. *Journal of Neuroscience*, **3**(10), 2043–2053.

Osen, K. K. (1969). Cytoarchitecture of the cochlear nuclei in the cat. *Journal of Comparative Neurology*, **136**(4), 453–483.

Peterson, A. J., Irvine, D. R., and Heil, P. (2014). A model of synaptic vesicle-pool depletion and replenishment can account for the interspike interval distributions and nonrenewal properties of spontaneous spike trains of auditory-nerve fibers. *Journal of Neuroscience*, **34**(45), 15097–15109.

Pickles, J. (2013). *An introduction to the physiology of hearing*. 4th Ed. Brill Academic Publishers, Leiden, NL.

Rhode, W., Oertel, D., and Smith, P. (1983). Physiological response properties of cells labeled intracellularly with horseradish peroxidase in cat ventral cochlear nucleus. *Journal of Comparative Neurology*, **213**(4), 448–463.

Rhode, W. S. and Smith, P. H. (1986). Encoding timing and intensity in the ventral cochlear nucleus of the cat. *Journal of neurophysiology*, **56**(2), 261–286.

Rothman, J. S. and Manis, P. B. (2003a). Differential expression of three distinct potassium currents in the ventral cochlear nucleus. *Journal of Neurophysiology*, **89**(6), 3070–3082.

Rothman, J. S. and Manis, P. B. (2003b). Kinetic analyses of three distinct potassium conductances in ventral cochlear nucleus neurons. *Journal of neurophysiology*, **89**(6), 3083–3096.

Rothman, J. S. and Manis, P. B. (2003c). The roles potassium currents play in regulating the electrical activity of ventral cochlear nucleus neurons. *Journal of neurophysiology*, **89**(6), 3097–3113.

Ryugo, D. K. and Parks, T. N. (2003). Primary innervation of the avian and mammalian cochlear nucleus. *Brain research bulletin*, **60**(5-6), 435–456.

Sachs, M. B., Bruce, I. C., Miller, R. L., and Young, E. D. (2002). Biological basis of hearing-aid design. *Annals of Biomedical Engineering*, **30**(2), 157–168.

Schnupp, J., Nelken, I., and King, A. (2011). *Auditory neuroscience: Making sense of sound*. MIT press.

Shofner, W. P. and Young, E. D. (1985). Excitatory/inhibitory response types in the cochlear nucleus: relationships to discharge patterns and responses to electrical stimulation of the auditory nerve. *Journal of neurophysiology*, **54**(4), 917–939.

Standring, S. (2015). *Gray's anatomy e-book: the anatomical basis of clinical practice*. Elsevier Health Sciences.

Winslow, R. L. and Sachs, M. B. (1987). Effect of electrical stimulation of the crossed olivocochlear bundle on auditory nerve response to tones in noise. *Journal of neurophysiology*, **57**(4), 1002–1021.

Xie, R. and Manis, P. B. (2013). Target-specific ipsc kinetics promote temporal

processing in auditory parallel pathways. *Journal of Neuroscience*, **33**(4), 1598–1614.

Xie, R. and Manis, P. B. (2017). Radiate and planar multipolar neurons of the mouse anteroventral cochlear nucleus: Intrinsic excitability and characterization of their auditory nerve input. *Frontiers in neural circuits*, **11**, 77.

Young, E. D. and Oertel, D. (2004). Cochlear nucleus. *The synaptic organization of the brain*, **5**.

Young, E. D., Robert, J.-M., and Shofner, W. P. (1988). Regularity and latency of units in ventral cochlear nucleus: implications for unit classification and generation of response properties. *Journal of Neurophysiology*, **60**(1), 1–29.

Zhang, X., Heinz, M. G., Bruce, I. C., and Carney, L. H. (2001). A phenomenological model for the responses of auditory-nerve fibers: I. nonlinear tuning with compression and suppression. *The Journal of the Acoustical Society of America*, **109**(2), 648–670.

Zilany, M. S. and Bruce, I. C. (2006). Modeling auditory-nerve responses for high sound pressure levels in the normal and impaired auditory periphery. *The Journal of the Acoustical Society of America*, **120**(3), 1446–1466.

Zilany, M. S., Bruce, I. C., Nelson, P. C., and Carney, L. H. (2009). A phenomenological model of the synapse between the inner hair cell and auditory nerve: long-term adaptation with power-law dynamics. *The Journal of the Acoustical Society of America*, **126**(5), 2390–2412.

Zilany, M. S., Bruce, I. C., and Carney, L. H. (2014). Updated parameters and expanded simulation options for a model of the auditory periphery. *The Journal of the Acoustical Society of America*, **135**(1), 283–286.